

## Supporting Information

### Common xanthene fluorescent dyes are visible-light activatable CO-releasing molecules

Marek Martínek,<sup>1,2</sup> Lucie Ludvíková,<sup>1</sup> Mária Šranková,<sup>3</sup> Rafael Navrátil,<sup>4</sup> Lucie Muchová,<sup>3</sup> Jiří Huzlík,<sup>5</sup> Libor Vítek,<sup>3,6</sup> Petr Klán,<sup>1,2</sup> Peter Šebej<sup>1,\*</sup>

<sup>1</sup> RECETOX, Faculty of Science, Masaryk University, Kamenice 735/5, D29; 625 00 Brno-Bohunice, Czech Republic

<sup>2</sup> Department of Chemistry, Faculty of Science, Masaryk University, Kamenice 735/5, A08; 625 00 Brno-Bohunice, Czech Republic

<sup>3</sup> Institute of Medical Biochemistry and Laboratory Diagnostics, General University Hospital in Prague and 1<sup>st</sup> Faculty of Medicine, Charles University, Kateřinská 32, 121 08 Praha 2, Czech Republic

<sup>4</sup> Department of Organic Chemistry, Faculty of Science, Charles University, Hlavova 2030/8, 128 43, Prague, Czech Republic

<sup>5</sup> Transport Research Centre (CDV), Líšeňská 33a, 636 00 Brno-Líšeň, Czech Republic

<sup>6</sup> 4<sup>th</sup> Department of Internal Medicine, General University Hospital in Prague and 1<sup>st</sup> Faculty of Medicine, Charles University, Kateřinská 32, 121 08 Praha 2, Czech Republic

\* sebej@recetox.muni.cz

## Contents

Materials and Methods	S2
Synthesis	S4
Physical-chemical and Photophysical Properties of Dyes 1–3	S6
Irradiation Experiments	S8
Role of Singlet Oxygen	S13
Measurement of IR(g)	S14
Quantification of Released CO(g)	S16
CO(g) Solubility in Protic Organic Solvents	S18
Analysis of Non-gaseous Photoproducts in the Reaction Mixture	S20
Photochemical Reactivity of Fluorescein Cation	S24
Thermal Chemistry	S26
Kinetics of Photochemical Degradation of Dyes 1–3	S27
NMR, IR, UV/vis, Fluorescence Spectral Data	S33
TGA and DSC Data	S63
MS Data on Degradation Photoproducts from the Dyes 1–3	S75
Emission Spectra of Used Light Sources	S98
Acknowledgement	S103
References	S104

## Experimental Section

### Materials and Methods

Reagents and solvents of the highest purity available were used as purchased, or they were purified/dried when necessary. Phosphate buffer saline (PBS) was prepared by diluting commercially available PBS tablets in a volumetric flask with demineralized water or water- $d_2$  to a 1× buffer (pH = 7.4,  $I = 0.1 \text{ mol dm}^{-3}$ ). Triethylammonium acetate buffer (TEAA) was prepared by a 1:10 dilution of the stock solution (prepared by direct addition of triethylamine (138.6 mL) and glacial acetic acid (57.2 mL)) into 500 mL water in a volumetric cylinder, adjusting pH to 7.0, and addition of demineralized water up to 1 L. All synthetic steps were performed under ambient atmosphere unless stated otherwise.

NMR spectra were recorded on 300 or 500 MHz spectrometers in dimethylsulfoxide- $d_6$ , water- $d_2$ , or methanol- $d_4$ . The signals in  $^1\text{H}$  and  $^{13}\text{C}$  NMR spectra were referenced<sup>1</sup> to the residual peak of a (major) solvent except for  $\text{D}_2\text{O}$ . The deuterated solvents were kept over high-temperature-dried 3 Å molecular sieve (8–12 mesh) under dry  $\text{N}_2$ . Mass spectra were recorded on a triple quadrupole spectrometer in a positive mode with EI (70 or 22 eV). HPLC analyses were performed using a standard automated high-pressure liquid chromatography system equipped with DAD and FLD detectors using a Zorbax SB-Aq column ( $4.6 \times 150 \text{ mm}$ ;  $3.5 \mu\text{m}$  particles) with acetonitrile/water 6:4 (v/v) as an isocratic mobile phase at 22 °C. For quantification of CO, we used either a GC-headspace instrument (5Å molecular sieve packed column) equipped with a RGA detector, calibrated with standard commercial solution of 10 ppm CO(g) in  $\text{N}_2$ (g), or a GC-headspace instrument (5Å molecular sieve packed column) equipped with a TIC/MS detector in a SIM mode, calibrated using the quantitative photoreaction of cyclopropanone photoCORM ( $50\text{--}600 \mu\text{L}$ ,  $c \sim 1 \times 10^{-5} \text{ mol dm}^{-3}$ , in methanol).<sup>1</sup> A gas chromatograph equipped with a mass spectrometer was used for quantification of CO(g) in the atmosphere over the reaction mixture in headspace vials. The GC instrument was equipped with a molecular sieve filled with an MXT-MSieve 5A column (length 30 m, i.d. 0.53 mm, df 50  $\mu\text{m}$ ) from Restek, and coupled to a ESI mass detector.

UV-vis spectra were obtained with matched 1.0 cm quartz cells. Fluorescence was measured on an automated luminescence spectrometer in 1.0 cm quartz fluorescence cuvettes at  $23 \pm 2$  °C using 90-degree mode; the sample concentration was set to keep the absorbance below 0.1 at  $\lambda_{\text{max}}$ ; emission spectra were normalized and corrected using standard correction files.

IR spectra of solid or liquid samples were obtained on a FT spectrometer using an ATR sample holder. IR spectra of gaseous samples were obtained on a FT spectrometer using a matched cuvette for gaseous samples ( $V = 0.5 \text{ L}$ ) with a 5-m optical pathway and KBr optical windows. Exact masses were obtained using a time-of-flight mass spectrometer with electrospray ionization or atmospheric-pressure chemical ionization in a positive mode. Melting points were obtained using a non-calibrated Kofler's hot stage melting point apparatus. Elemental analyses were performed on an automatic analyzer. The solution pH values were determined using a glass electrode calibrated with the certified buffer solutions at pH = 4, 7, or 10.

All differential thermal scanning calorimetry (DSC) and thermogravimetric analysis (TG) were performed on a NETZSCH STA-449C Jupiter analyzer with a SiC oven (allowing to reach temperatures up to 1550 °C) under inert atmosphere. The balance was kept at a constant temperature of  $T = 30$  °C and protected from heat and fouling by the nitrogen atmosphere. The samples ( $\sim 10 \text{ mg}$ ) were measured in carborundum crucibles under the dynamic atmosphere of dry  $\text{N}_2$  (g) (5.0 purity). The gas flowed through an oven with a velocity of  $100 \text{ cm}^{-3} \text{ min}^{-1}$ . Obtained thermograms were processed in a Netzsch Proteus software. The released gases were analyzed by a coupled FT-IR spectrometer Tensor 27 equipped with a TG/IR extension with

MCT detector. The connection capillary and the measurement cell were kept at a constant temperature of  $T = 200$  °C during all measurements.

The absolute quantum yields of degradation of the compounds **1–3** were determined using 4,4'-difluoro-8-methoxymethyl-1,3,5,7-tetramethyl-4-bora-3a,4a-diaza-*s*-indacene (labeled as a “compound **3**” in ref.)<sup>2</sup> as a chemical actinometer. The samples of **1–3** were irradiated under same conditions as the actinometer and the quantum yield were then calculated as a ratio of relative rates of degradation of **1–3** and actinometer multiplied by known quantum yield of decomposition of the actinometer ( $0.02 \pm 0.001$ ) under the given irradiation conditions. Conversions were kept below 15 % to avoid secondary photochemical processes.

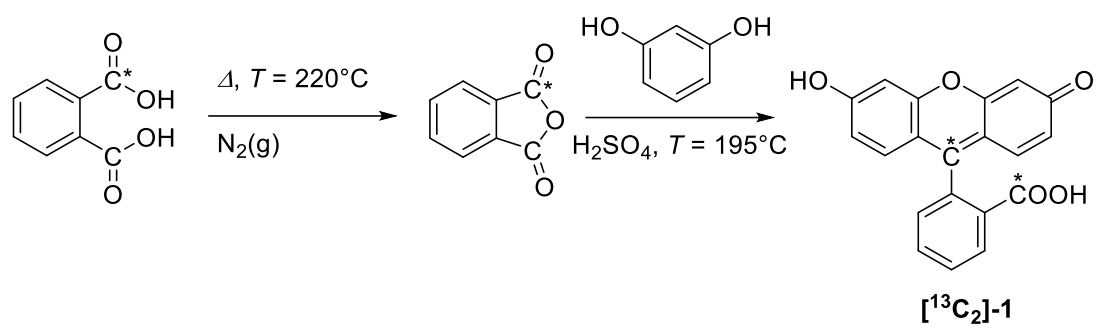
The photodissociation spectra were acquired with an ISORI instrument described in detail elsewhere.<sup>3–6</sup> Fluorescein cations were generated by electrospray ionization of a  $1 \times 10^{-5}$  mol dm<sup>-3</sup> fluorescein solution in methanol (typical ESI conditions: 6 kV capillary voltage, 100 V tube lens voltage, 200 °C capillary temperature, 30 psi nitrogen sheath gas pressure, 0.2 mL h<sup>-1</sup> flow rate, 100- $\mu$ m internal diameter fused-silica capillary). Fluorescein ions were then mass selected by the first quadrupole and guided by the quadrupole bender and the octopole towards the wire quadrupole trap. The trap is cooled to temperatures below 3 K. The ions were trapped and cooled by collisions with helium-buffer gas, a part of the ions was transformed into helium-tagged complexes. The trapped ions were subjected to photodissociation experiments with visible light, the contents of the ion trap were subsequently extracted, mass-analyzed by the second quadrupole, and detected by a Daly-type detector operated in an ion-counting mode. In alternating scans, the light beam was either guided into the ion trap or blocked by a mechanical shutter, giving the number of ions after the irradiation ( $N_i$ ) and the number of nonirradiated ions ( $N_{i0}$ ). The high-resolution helium-tagging photodissociation spectrum was constructed as the wavenumber dependence of  $(1 - N_i/N_{i0})$ . Moreover, the presented helium-tagging photodissociation spectrum (Figure S8, red trace) was normalized by dividing tagged ion attenuation by laser power ( $E_{laser}$ ) and by irradiation time ( $T_{irr}$ , typically 800 ms), *i.e.*,  $(1 - N_i/N_{i0})/(E_{laser} \times T_{irr})$  to account mainly for laser power fluctuations. The parent fluorescein ion attenuation was monitored and normalized in a high-resolution photodissociation spectrum (blue trace in Figure S8) and, thus, expressed as  $(1 - N_{i,parent}/N_{i,parent})/(E_{laser} \times T_{irr})$ .

The high-resolution laser irradiation was generated by a Sunlite EX OPO tunable laser system (Continuum), which was pumped with a seeded PL 9010 laser (linewidth  $<0.1$  cm<sup>-1</sup>, 10 ns pulse length). The wavelength of the Sunlite EX OPO was calibrated using a WS6-600 wavelength meter (HighFinesse GmbH).

## Synthesis

**[9-<sup>13</sup>C][carboxy-<sup>13</sup>C]-fluorescein ([<sup>13</sup>C<sub>2</sub>]-1).** [HOO<sup>13</sup>C]-Phthalic acid (0.25 g, 1.50 mmol) was dried (3 × vacuum/dry N<sub>2</sub>(g)) in a sublimation apparatus equipped with a water-cooled finger (5 °C) and then heated to 220 °C (temperature of the oil bath) for 3.5 h under dry N<sub>2</sub>(g) atmosphere. The sublimate appeared on a cooled finger and was collected after cooling back to 20 °C. White crystalline solid (with needle-like long and thin crystals). Yield: 197 mg (88 %). <sup>1</sup>H NMR (300 MHz, DMSO-*d*<sub>6</sub>): δ 7.55–7.61 (m, 2H), 7.63–7.70 (m, 2H) ppm (Figure S17). <sup>13</sup>C{<sup>1</sup>H} NMR (75.5 MHz, DMSO-*d*<sub>6</sub>): δ 168.6 ppm (only the carbon atom with [<sup>13</sup>C]-label was visible under the conditions used; Figure S18). Note: Measurement of HRMS (ESI-) showed only a signal at *m/z*: [M–H]<sup>–</sup> 166.0224, which corresponds to the [HOO<sup>13</sup>C]-phthalic acid with calcd *m/z* for (<sup>12</sup>C)<sub>7</sub><sup>13</sup>CH<sub>5</sub>O<sub>4</sub> 166.0227, probably because it ionizes better than phthalanhydride. This reaction intermediate, [<sup>13</sup>C]-phthalic anhydride, was used immediately in the next step without further purification. Note: We estimated the half-life of the [<sup>13</sup>C]-phthalic anhydride in DMSO-*d*<sub>6</sub> solution to be *t*<sub>1/2</sub> ~ 3 days, as we observed about ~20% hydrolysis after 1 day (<sup>1</sup>H NMR).

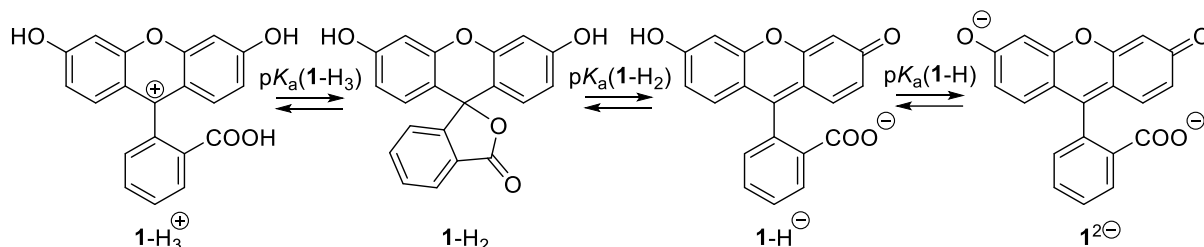
This procedure was adopted from Nencki and Sieber,<sup>7</sup> Stephenson and Shimizu<sup>8</sup> and Vogel et al.<sup>9</sup> Sulfuric acid (aq, *c* = 2 mol dm<sup>–3</sup>, 6 drops) was added to a mixture of [<sup>13</sup>C]-phthalic anhydride (196 mg, 1.32 mmol) and resorcinol (295 mg, 2.68 mmol) in a pre-dried 50 mL round bottom flask. The reaction mixture was then heated to 195 °C (in a pre-heated oil bath) for 30 min and then allowed to cool down for about 5 min. Acetone (10 mL) was added cautiously (acetone could be boiling), and the resulting mixture was vigorously stirred for 10 min at 20 °C, while all the solid dissolved. Volatiles were removed under reduced pressure, and the obtained solid residuum was dissolved in a mixture of diethyl ether (30 mL) and water (1.5 mL) and stirred vigorously for 10 min. The organic layer was separated, washed with water (15 mL) and brine (15 mL), dried over anhydrous magnesium sulfate, decanted, and volatiles were removed under reduced pressure. The resulting red-orange crystalline solid residuum was further dried under a high vacuum to yield an orange crystalline solid (239 mg; <sup>1</sup>H NMR (DMSO-*d*<sub>6</sub>) revealed that this product was a ~1:1 mixture with unreacted resorcinol). This material was further purified according to a procedure reported by Sujeeth.<sup>10</sup> All obtained material was suspended in water (0.5 mL) in a beaker (10 mL) and heated until all the solid material dissolved (water was slightly below the boiling point) and then filtered through a pre-heated (150 °C, oven) glass frit (S4); the filter cake was then washed with boiling water (2 × 0.55 mL), collected and dried under high vacuum to yield pure product. Yield: 116 mg (26 %). Dark red crystalline solid. Mp: >215 °C (lit.<sup>11</sup> 315–317 °C; lit.<sup>12</sup> 344 °C). <sup>1</sup>H NMR (500 MHz, DMSO-*d*<sub>6</sub>): δ 6.54 (s, 4H), 6.68 (s, 2H), 7.26 (d, 1H, *J* = 7.7 Hz), 7.71 (t, 1H, *J* = 7.5 Hz), 7.79 (t, 1H, *J* = 7.4 Hz), 7.98 (d, 1H, *J* = 7.6 Hz), 10.08 (s, 2H, –OH) ppm (Figure S21). <sup>13</sup>C{<sup>1</sup>H} NMR (125 MHz, DMSO-*d*<sub>6</sub>): δ 83.0 (<sup>13</sup>C labelled), 102.2, 109.6 (t, *J* = 25 Hz), 112.6, 124.0 (d, *J* = 3.5 Hz), 124.5 (d, *J* = 3.3 Hz), 126.3 (d, *J* = 34 Hz), 129.0, 130.0, 135.5, 151.8, 152.4 (dd, *J*<sub>1</sub> = 27 Hz, *J*<sub>2</sub> = 21 Hz), 159.4, 168.6 ppm (Figure S22). IR (ATR): 3056, 1700, 1635, 1590, 1456, 1383, 1310, 1262, 1242, 1210, 1110, 1081, 863, 847, 698, 601, 591, 574, 497, 458 cm<sup>–1</sup> (Figure S19). HRMS (ESI-) *m/z*: [M–H]<sup>–</sup> calcd for (<sup>12</sup>C)<sub>19</sub><sup>13</sup>CH<sub>11</sub>O<sub>5</sub> 332.0646; found 332.0640. Note: our melting point apparatus can heat samples only up to 215 °C, so we could not measure the melting point.



**Scheme S1.** Synthesis of [9- $^{13}\text{C}$ ][carboxy- $^{13}\text{C}$ ]-fluorescein [ $^{13}\text{C}_2$ ]-1.

### Physical-chemical and Photophysical Properties of Dyes 1–3

All dyes **1–3** can exist in four acid–base forms in aqueous solutions (Scheme S2), and their populations are pH dependent. At physiologically relevant pH (6–8), only anionic forms **X-H<sup>-</sup>** and **X<sup>2-</sup>** (**X = 1–3**) are detected (e.g.,  $pK_a(\mathbf{1-H}_2) = 4.31$  and  $pK_a(\mathbf{1-H}^-) = 6.43$ ),<sup>13</sup> thus, the dianion is the major or sole form of **1** at pH = 7.4. In contrast, **X-H<sub>2</sub>** as a neutral species is the major form in non-polar media. The **X-H<sub>3</sub><sup>+</sup>** and **XH<sub>2</sub>** forms are weakly absorbing species in an aqueous environment.<sup>13</sup>



**Scheme S2.** Acid and base forms of **1** in aqueous media. Both anion **1-H<sup>-</sup>** and neutral form **1-H<sub>2</sub>** could be present as more than one tautomer<sup>13</sup> (omitted for clarity).

Absorption and emission spectra of **1–3** in an aqueous buffer (phosphate-buffered saline; (1×) PBS, pH = 7.4,  $I = 0.1 \text{ mol dm}^{-3}$ ) solution are shown in Figures S1 and S24–S26, and an overview of the basic spectroscopic data is given in Table S1.

Dyes **1–3** have their major absorption bands centered in the green region with  $\lambda_{\text{max}}(\text{abs})$  in the range of 490–550 nm (Figure S1, Table 1). The shape of the bands and the positions of maxima exhibit only relatively small solvatochromic shifts.<sup>14–17</sup> They are fluorescent with fluorescence quantum yields ( $\Phi_f$ ) spanning from 0.02 for **3** to 0.93 for **1** in an aqueous solution at pH ~ 7.4. Fluorescence represents the major deactivation channel for excited fluorescein. The compounds exhibit only small Stokes shifts (15–25  $\text{cm}^{-1}$ ), which is a typical feature of xanthene dyes.<sup>18,19</sup> The excitation spectra closely match the absorption spectra (Figures S24–S26).

All dyes **1–3** can exist in four acid–base forms in aqueous solutions (Scheme S2), and their populations are pH dependent. At physiologically relevant pH (6–8), only anionic forms **X-H<sup>-</sup>** and **X<sup>2-</sup>** (**X = 1–3**) are detected (e.g.,  $pK_a(\mathbf{1-H}_2) = 4.31$  and  $pK_a(\mathbf{1-H}^-) = 6.43$ ),<sup>13</sup> thus, the dianion is the major or sole form of **1** at pH = 7.4. In contrast, **X-H<sub>2</sub>** as a neutral species is the major form in non-polar media. The **X-H<sub>3</sub><sup>+</sup>** and **XH<sub>2</sub>** forms are weakly absorbing species in an aqueous environment.<sup>13</sup>

**Table S1.** Photophysical Properties of **1–3** in Aqueous Solutions.<sup>a</sup>

Cmpd	$\lambda_{\text{max}}(\text{abs})/\text{nm}$	$\epsilon/\text{dm}^3 \text{ mol}^{-1} \text{ cm}^{-1}$	deactivation pathways			
			major	$\Phi_f^b$	$\Phi_{\text{isc}}^c$	$\Phi_{\Delta}^d$
<b>1</b>	490 (490) <sup>13</sup>	$7.69 \times 10^4$ (0.1 mol $\text{dm}^{-3}$ NaOH) <sup>13</sup>	fl <sup>e</sup>	0.93 <sup>13</sup>	0.03 <sup>20</sup>	0.1, <sup>20</sup> 0.06 <sup>21</sup>
<b>2</b>	517 (517) <sup>22</sup>	$9.9 \times 10^4$ <sup>23</sup>	fl <sup>e</sup> , isc <sup>f</sup>	0.43 <sup>24</sup> 0.20 <sup>16</sup>	$0.7 \pm 0.1$ (pH 9), <sup>25</sup> $0.4 \pm 0.03$ (H <sub>2</sub> O) <sup>26</sup>	0.4 <sup>20</sup>
<b>3</b>	549 (549) <sup>14</sup>	$9.5 \times 10^4$ (H <sub>2</sub> O) <sup>14,16</sup>	isc <sup>f</sup>	<0.02 <sup>14</sup>	0.98 <sup>27</sup>	0.76 <sup>20</sup>

<sup>a</sup> In aqueous solutions at 20 °C: PBS (see Supporting Information), unless stated otherwise. The values from the literature are given in parentheses. <sup>b</sup> Quantum yield of fluorescence. <sup>c</sup> Quantum yield of inter-system crossing. <sup>d</sup> Quantum yield of sensitization of oxygen to singlet oxygen <sup>1</sup>O<sub>2</sub>. <sup>e</sup> Fluorescence. <sup>f</sup> Intersystem crossing to the triplet excited state.

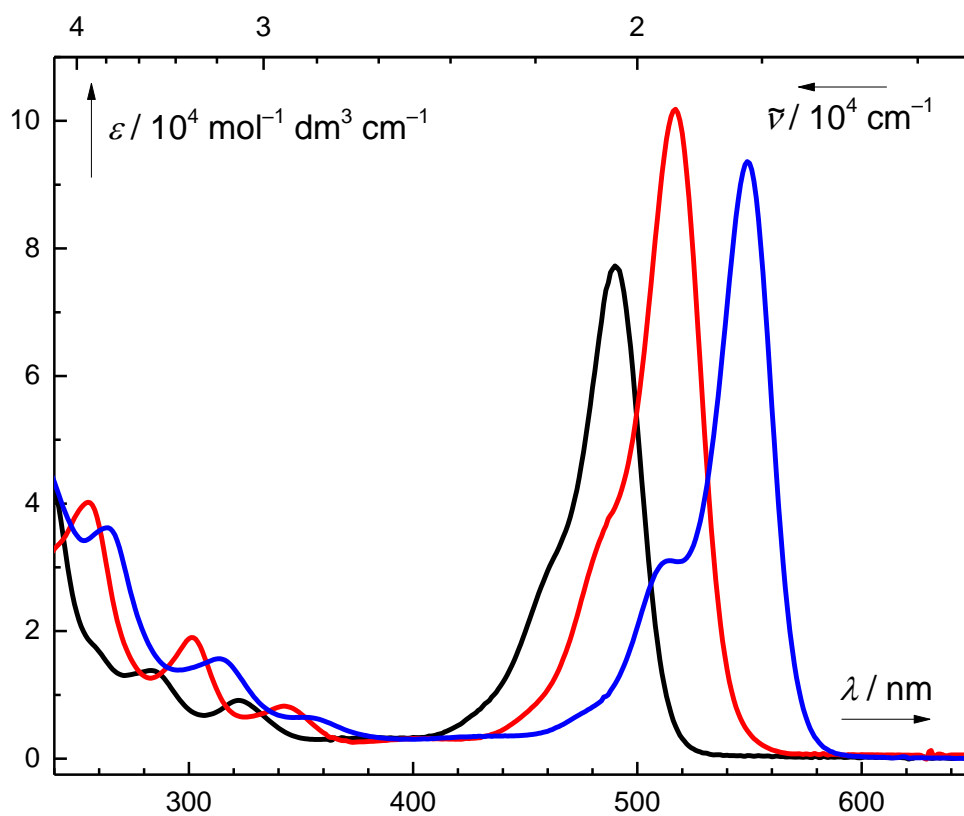


**Figure S1.** Absorption spectra of fluorescein (**1**; black), eosin Y (**2**; red) and rose bengal (**3**; blue) in PBS ( $c(\text{dye}) \sim 1 \times 10^{-5} \text{ mol dm}^{-3}$ ).

## Irradiation Experiments

We performed an array of irradiation experiments with **1**, **2**, and **3** under various experimental conditions to: a) determine kinetic parameters of the photolysis; b) assess the role of singlet oxygen in the photolysis; and c) identify the photoproducts. We employed a battery of analytical techniques, including UV/vis absorption spectrometry, NMR, MS (following the coupled chromatographic separation), IR (g) and gas chromatography with various detectors (except MS).

### Absorption Spectra Change upon Irradiation

Solutions of **1**, **2** and **3** ( $c = 1.3\text{--}1.5 \times 10^{-5} \text{ mol dm}^{-3}$ ; the concentrations were adjusted to have  $A(\lambda_{\text{max}}(\text{abs})) \sim 1 - 1.5$ ) in PBS buffer ( $\text{pH} = 7.4$ ,  $I = 0.1 \text{ mol dm}^{-3}$ ) in matched 1-cm quartz cuvettes ( $V = 3 \text{ mL}$ ) were irradiated with a home-made light source equipped with 28 LED emitting at  $\lambda_{\text{max}}(\text{em}) = 509 \pm 17 \text{ nm}$  (Figure S82; Table S7) at the distance of  $\sim 1 \text{ cm}$  from the cuvette optical window at temperatures of  $T = 21$  or  $40^\circ\text{C}$ . The reaction progress was monitored by a UV-vis diode-array spectrophotometer in the given time intervals. The degradation lifetimes under continuous irradiation were found to be 3323, 5677 and 8581 s for **1**, **2** and **3**, respectively at  $21^\circ\text{C}$  (Table S2). The values obtained from fitting the values of absorption maxima to a single-exponential decay corresponded to the pseudo first-order degradation rate constants of  $3.01 \times 10^{-4}$ ,  $1.76 \times 10^{-4}$ , and  $1.17 \times 10^{-4} \text{ s}^{-1}$  for **1**, **2**, and **3**, respectively.

**Table S2.** Degradation lifetimes obtained upon irradiation of **1**, **2**, and **3**, obtained from fitting the values of absorption maxima recorded during in the course of irradiation to single-exponential decay.

Compd.	$T = 21^\circ\text{C}$		$T = 40^\circ\text{C}$	
	$\tau/\text{s}$	$k_{\text{obs}}/\text{s}^{-1}$	$\tau/\text{s}$	$k_{\text{obs}}/\text{s}^{-1}$
<b>1</b>	3323	$3.01 \times 10^{-4}$	2652	$3.77 \times 10^{-4}$
<b>2</b>	5677	$1.76 \times 10^{-4}$	1763	$5.76 \times 10^{-4}$
<b>3</b>	8581	$1.17 \times 10^{-4}$	6020	$1.66 \times 10^{-4}$

The obtained degradation rates cannot be compared directly, but we further corrected them with the absorption spectra of the dyes, the emission spectra of the used light source ( $\lambda_{\text{max}}(\text{em}) = 509 \pm 17 \text{ nm}$  (Figure S82; Table S7)), and their effective overlap integrals to calculate relative quantum yields of degradation of **1–3** (Table S3).

**Table S3.** Relative quantum yields of degradation of **1**, **2**, and **3** upon irradiation with LED source ( $\lambda_{\text{em}} = 509 \pm 17 \text{ nm}$ ; Figure S82; Table S7) at  $T = 21^\circ\text{C}$ .

Compd.	$\Phi_{\text{decomp}}(\text{rel.})$
<b>1</b>	1
<b>2</b>	0.19
<b>3</b>	0.16

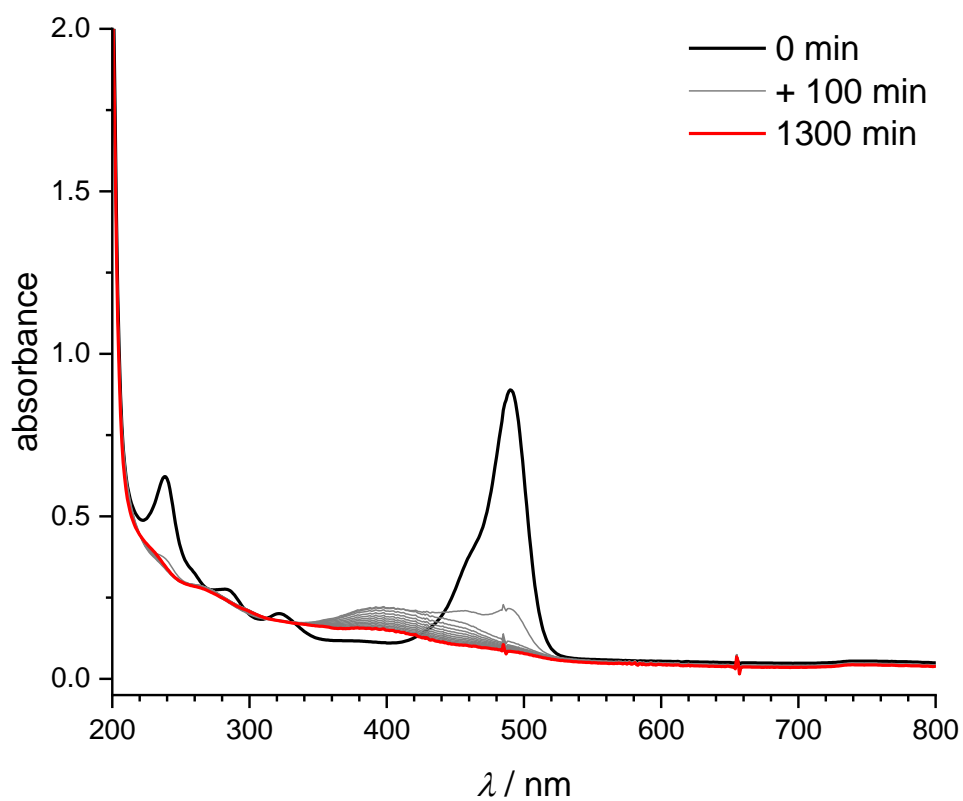


**Figure S2.** UV-vis absorption spectra of fluorescein (**1**,  $c \sim 1.3 \times 10^{-5} \text{ mol dm}^{-3}$ ) in PBS (pH = 7.4,  $I = 0.1 \text{ mol dm}^{-3}$ ) measured during continuous irradiation with LEDs ( $\lambda_{\text{em}} = 509 \pm 17 \text{ nm}$ ; Figure S82) under ambient atmosphere. Starting spectrum (thick black line) and end spectrum (thick red line) are highlighted.

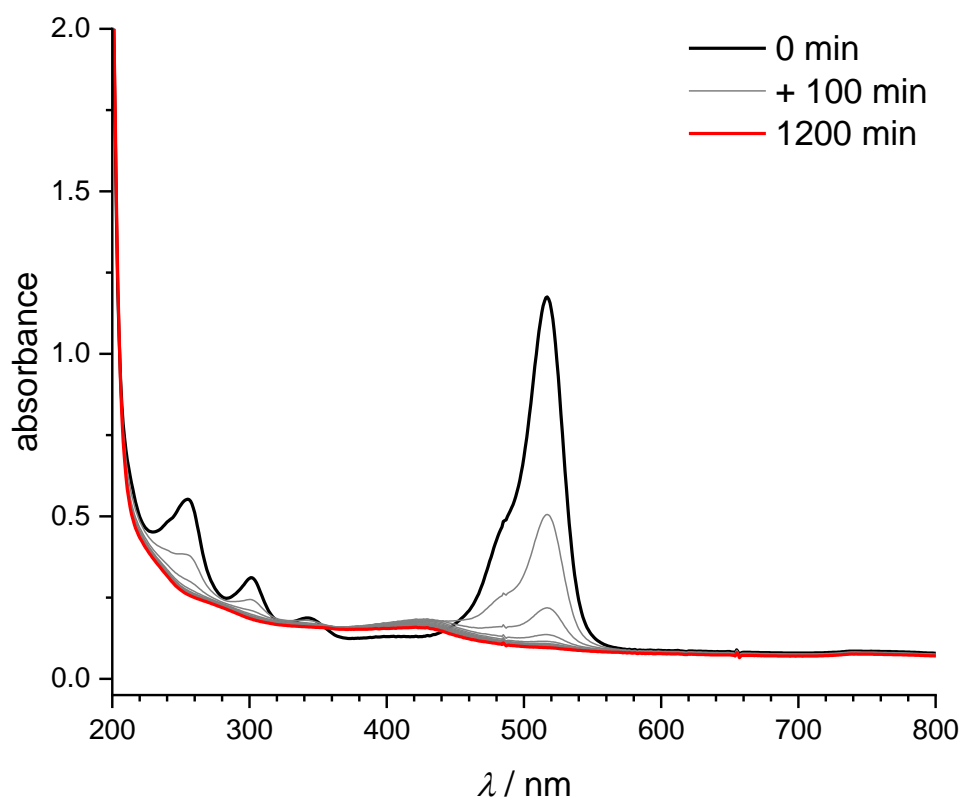


**Figure S3.** UV-vis absorption spectra of eosin Y (**2**,  $c \sim 1.3 \times 10^{-5} \text{ mol dm}^{-3}$ ) in PBS (pH = 7.4,  $I = 0.1 \text{ mol dm}^{-3}$ ) measured during continuous irradiation with LEDs ( $\lambda_{\text{em}} = 509 \pm 17 \text{ nm}$ ; Figure S82) under ambient atmosphere. Starting spectrum (thick black line) and end spectrum (thick red line) are highlighted.

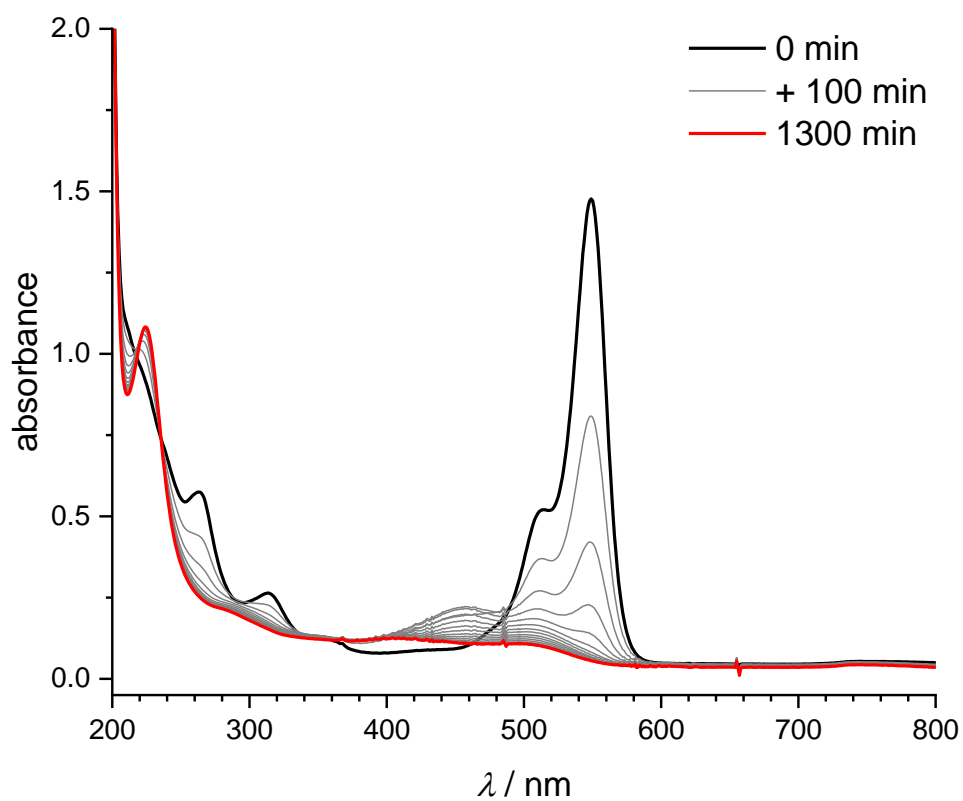


**Figure S4.** UV-vis absorption spectra of rose bengal (**3**,  $c \sim 1.5 \times 10^{-5} \text{ mol dm}^{-3}$ ) in PBS (pH = 7.4,  $I = 0.1 \text{ mol dm}^{-3}$ ) measured during continuous irradiation with LEDs ( $\lambda_{\text{em}} = 509 \pm 17 \text{ nm}$ ; Figure S82) under ambient atmosphere. Starting spectrum (thick black line) and end spectrum (thick red line) are highlighted.

Model	ExpDec1					
Equation	$y = A1 \cdot \exp(-x/t1) + y0$					
Plot	kincomparision_L	kincomparision_H	kincomparision_I	kincomparision_J	kincomparision_K	kincomparision_M
y0	$0.0018 \pm 6.72364E-4$	$0.01073 \pm 7.55094E-4$	$0.0236 \pm 0.00171$	$0.00269 \pm 9.68171E-4$	$0.00726 \pm 6.89481E-4$	$0.00402 \pm 4.67582E-4$
A1	$1.03721 \pm 0.00297$	$1.02175 \pm 0.00581$	$0.96356 \pm 0.0144$	$1.05767 \pm 0.00546$	$1.01603 \pm 0.00647$	$1.01614 \pm 0.00264$
t1	$8580.75086 \pm 41.87565$	$3322.61922 \pm 30.50326$	$2652.22742 \pm 64.71678$	$5676.81957 \pm 47.89754$	$1762.77915 \pm 19.089$	$6020.368 \pm 25.51005$
Reduced Chi-Sqr	$3.61005E-5$	$6.54489E-5$	$3.47458E-4$	$8.63496E-5$	$5.61594E-5$	$2.11708E-5$
R-Square (COD)	0.99926	0.99724	0.98086	0.99782	0.99644	0.99942
Adj. R-Square	0.99925	0.9972	0.98057	0.99778	0.99638	0.99941

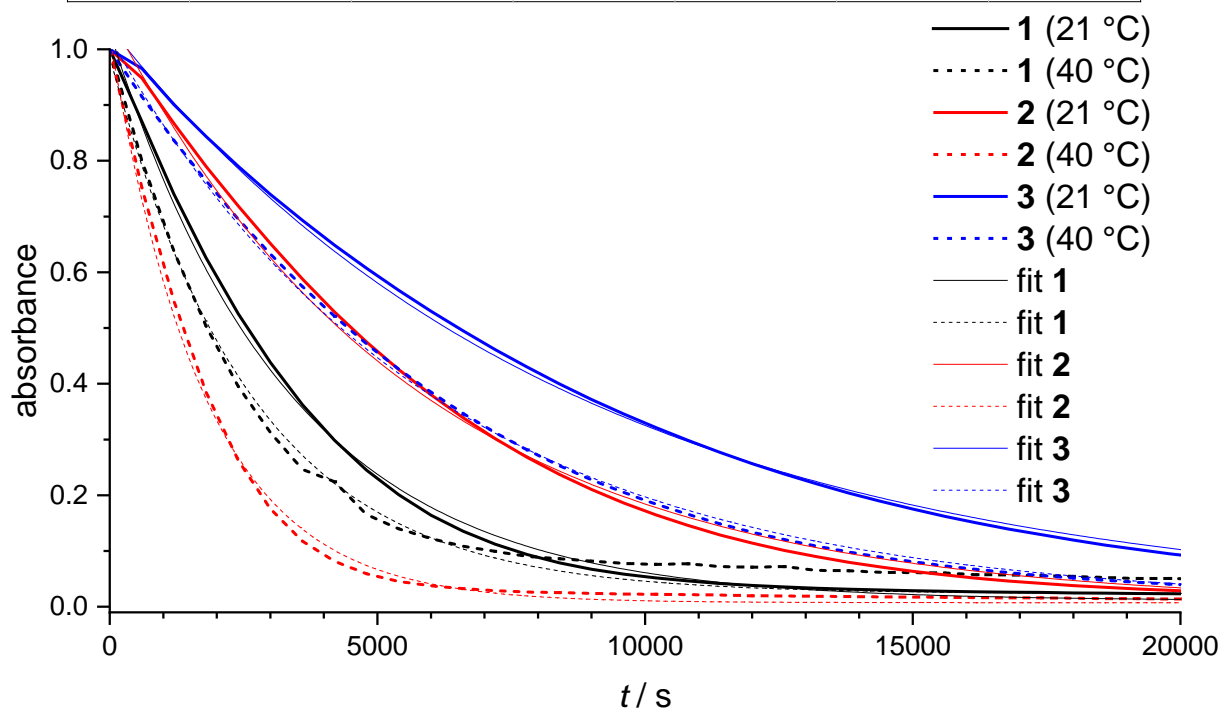


**Figure S5.** Normalized kinetic profiles of **1** (black), **2** (red), and **3** (blue) absorbance change recorded at their respective maxima under continuous irradiation by LEDs under an ambient atmosphere at 21 °C (solid lines) and 40 °C (dotted lines).

### Role of Singlet Oxygen

Solutions of **1**, **2** and **3** ( $c = 1.3\text{--}1.5 \times 10^{-5} \text{ mol dm}^{-3}$ ; the concentrations were adjusted to have  $A(\lambda_{\text{max}}(\text{abs})) \sim 1\text{--}1.5$ ) in a PBS buffer (pH = 7.4,  $I = 0.1 \text{ mol dm}^{-3}$ )/methanol mixture (1:100, v/v) containing 1,4-dimethyl-1,4-dihydro-1,4-epidioxynaphthalene<sup>28</sup> (**4**,  $c = 5.3 \times 10^{-3} \text{ mol dm}^{-3}$ ) – a singlet oxygen-generating molecule<sup>29</sup> in matched 1-cm quartz cuvettes ( $V = 3 \text{ mL}$ ) were thermostated at  $T = 40 \text{ }^\circ\text{C}$ . The reaction progress was monitored by a UV-vis diode-array spectrophotometer. The results (Figure S6) suggests, that  $^1\text{O}_2$  plays a negligible role in the degradation of xanthene dyes **1–3**.

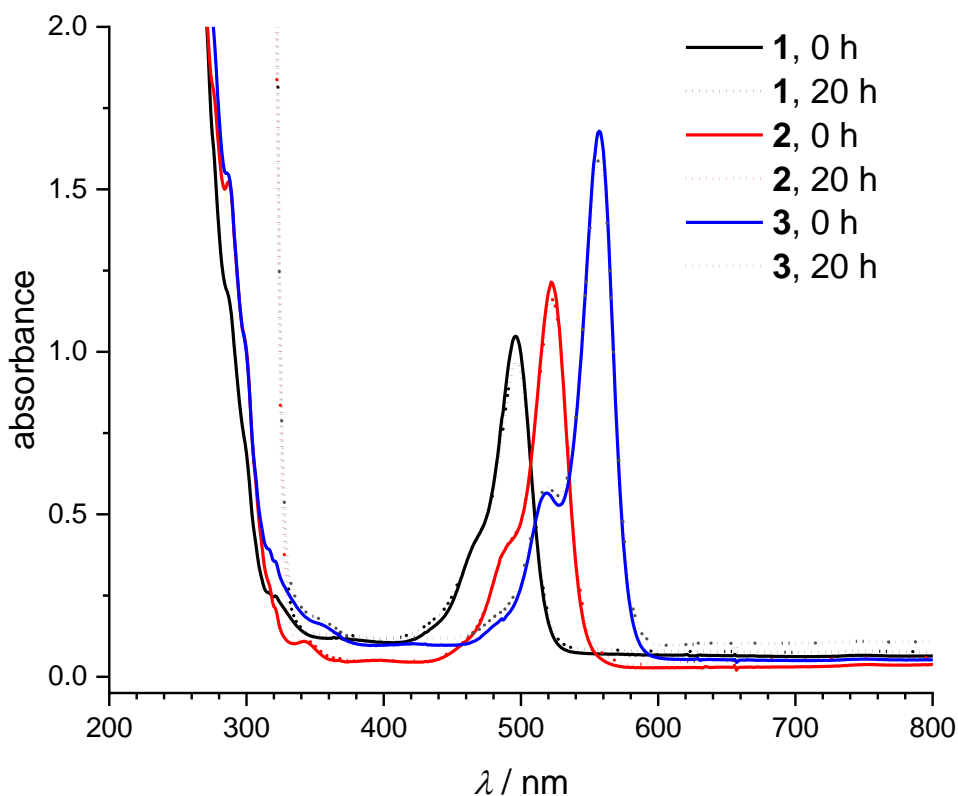


**Figure S6.** UV-vis absorption spectra of **1–3** ( $c = 1.3\text{--}1.5 \times 10^{-5} \text{ mol dm}^{-3}$ ) in the presence of singlet oxygen-generating molecule at  $T = 40 \text{ }^\circ\text{C}$  in the dark at the time  $t = 0$  (solid lines) and after 20 h (dotted lines).

## Measurement of IR of Gaseous Samples

### A) Qualitative Analysis

Solution of **1**, **2** and **3** ( $c = \sim 2\text{--}6 \times 10^{-5} \text{ mol dm}^{-3}$ ;  $m(\text{dye}) = 5 \text{ mg}$ ) in TEAA ( $c(\text{TEAA}) = 0.1 \text{ mol dm}^{-3}$  pH = 7.0,  $I = 0.1 \text{ mol dm}^{-3}$ ) were independently irradiated for  $\sim 48 \text{ h}$  (conversion was followed by a UV-vis spectroscopy) in a home-made glass reactor ( $V_{\text{total}} = 1.05 \text{ L}$ ; Figure S81) with white-light LED reflectors ( $\lambda_{\text{irr}} = 400\text{--}700 \text{ nm}$ ,  $3 \times 100 \text{ W}$  reflector, Figure S83). The spectrometer measurement cell for gaseous samples ( $V = 0.5 \text{ L}$ , optical path  $d = 5 \text{ m}$ ) was evacuated with a membrane pump (to  $p \sim 10 \text{ kPa}$ ) and then equilibrated with the gaseous phase ( $V \sim 0.5 \text{ L}$ ) over the irradiated reaction mixture samples in the reactor (typically gave pressure  $p \sim 48 \text{ kPa}$ ).

### B) Semiquantitative Analysis

The cell for gaseous samples ( $V = 0.5 \text{ L}$ , optical pathway  $d = 5 \text{ m}$ ) was filled with a standard sample of CO (10 ppm in  $\text{N}_2(\text{g})$ ) at a pressure of  $p = 100 \text{ kPa}$ . The measured IR(g) spectra of this sample were further used for the calibration. The IR spectra of all other samples of gaseous phase ( $p = 48 \text{ kPa}$ ), obtained from the irradiation experiments (*vide supra*), were measured under the same conditions as the standard (identical settings, same number of scans), and the spectral range of  $2160\text{--}2205 \text{ cm}^{-1}$  (this range, which comprises only a part of the CO(g) signal, was chosen to avoid interference of the signals of other compounds, such as carbon dioxide). For the calculation of the yields of CO, we used the following considerations.<sup>a</sup> The standard sample of CO (10 ppm in  $\text{N}_2$ ,  $p = 100 \text{ kPa}$ ) contains  $2.017 \times 10^{-7} \text{ mol}$  of CO in the sample cuvette ( $V = 0.5 \text{ L}$ ), which gives the given integral under the signal curve. For the reaction mixture, the integral was compared to that value and used to calculate the molar amount of CO in the sample cuvette, regardless of the total pressure of the gas phase. The obtained value was subtracted by a factor of 2.083 (reflecting that the released CO was distributed within the whole system – IR sample cuvette ( $V = 0.5 \text{ L}$ ) and over the reaction mixture ( $V(\text{liq.}) = 0.5 \text{ L}$ ) in the vessel (Figure S81;  $V(\text{gas phase}) = 0.55 \text{ L}$ )) to give the total molar amount of the CO in the gas phase. This total molar amount of CO was divided with the molar amount of the starting material dye (**1**, **2** and **3**, respectively) to give the chemical yield of released CO (in the gas phase; results and all important input values are shown in Table S4).

**Table S4.** Semi-quantitative calculation of chemical yields of CO obtained upon irradiation of **1**, **2** and **3**, using IR(g) spectroscopy.

sample	$p/\text{kPa}$ <sup>a</sup>	$A/\text{au}$ <sup>b</sup>	$n(\text{CO})_c/\text{mol}$ <sup>c</sup>	$n(\text{CO})_s/\text{mol}$ <sup>d</sup>	$m(\text{dye})/\text{mg}$ <sup>e</sup>	$n(\text{dye})/\text{mol}$ <sup>f</sup>	yield/%
standard <sup>g</sup>	100	0.3491	$2.017 \times 10^{-7}$	– <sup>h</sup>	– <sup>h</sup>	– <sup>h</sup>	– <sup>h</sup>
<b>1</b>	48	1.165	$6.737 \times 10^{-7}$	$1.403 \times 10^{-6}$	5	$1.329 \times 10^{-5}$	11
<b>2</b>	48	0.6282	$3.631 \times 10^{-7}$	$7.564 \times 10^{-7}$	5	$7.717 \times 10^{-6}$	10
<b>3</b>	48	0.8782	$5.083 \times 10^{-7}$	$1.059 \times 10^{-6}$	5	$4.913 \times 10^{-6}$	22

<sup>a</sup> Pressure in the system. <sup>b</sup> Integral under the signal curve in the  $2160\text{--}2205 \text{ cm}^{-1}$  range. <sup>c</sup> Molar amount of CO in the sample cuvette ( $V = 0.5 \text{ L}$ ). <sup>d</sup> Molar amount of CO in the whole system (sample cuvette ( $V = 0.5 \text{ L}$ ) and remaining gas phase over the reaction mixture in the reaction vessel ( $V = 0.55 \text{ L}$ )). <sup>e</sup> Weight of the starting material dye. <sup>f</sup> Molar amount of the starting material dye. <sup>g</sup> Commercial sample of 10 ppm CO in  $\text{N}_2(\text{g})$ . <sup>h</sup> Not relevant.

The obtained chemical yields are smaller than those obtained from GC (Table 1 in the main text) by a factor of about 4–11. One of the possible reasons for such small observed yields is

<sup>a</sup> This semiquantitative estimate covers only the part of CO, that was present in the gas phase over the reaction mixture and not the CO, that remained dissolved in the liquid reaction mixture (See “CO(g) Solubility in Protic Organic Solvents” on page S18 for more details).

that a part of CO remained dissolved in the reaction mixture solution (solubility of CO in an aqueous buffer is about  $8 \times 10^{-7} \text{ mol dm}^{-3}$ ; see "CO(g) Solubility in Protic Organic Solvents" on page S18 for more details).

### Quantification of Released CO(g)

Gas chromatography with two different methods of detection was used for the quantification of CO(g) released upon irradiation and over the reaction mixture solution. In both cases, the reaction mixtures of each **1-3** in aqueous solution (PBS buffer, pH = 7.4,  $I = 0.1 \text{ mol dm}^{-3}$ ) in a headspace vial with a gas-tight septum were irradiated with a visible light source until full conversion (evaluated by the disappearance of typical spectral features of the starting material in the visible light spectral region). Two typical experimental setups were used:

1) An aqueous solution of **1-3** ( $c \sim 2 \times 10^{-5} \text{ mol dm}^{-3}$ ;  $V = 0.5 \text{ mL}$ ) in a 2 mL vial (exact measured volume used for calculations  $V = 1.94 \text{ mL}$ ) was irradiated using three 100 W white LED lamps for 4 days, and an aliquot (100  $\mu\text{L}$ ) of the gaseous phase over the reaction mixture was analyzed by GC with MS detector. The obtained values were at least four orders of magnitude higher than background CO (g) levels (in the ambient air), and thus the obtained values were not corrected to the background.

2) A solution of **1-3** ( $c = 1 \times 10^{-5} \text{ mol dm}^{-3}$ ) in an aqueous solution ( $V = 0.1 \text{ mL}$ ) in headspace vial was irradiated using a 3 W LED light source lamp for minutes to hours (until no starting material was observed in a typical procedure) and the gaseous phase over the reaction mixture was analyzed by GC with either a coupled MS detector (aliquot injected) or a reducing gas analyzer (RGA) detector (whole headspace volume injected using flushing with two-syringe system). The values obtained with RGA analysis were significantly higher than background CO (g) levels (in the ambient air samples, which thus was ruled out as a potential source of the systematic error) and the average background values (determined each day independently before the sample measurements) were subtracted. The values obtained with GC/MS analyses were not corrected to background (vide supra).

In all cases, the amount of CO (g) was quantified using a calibration curve constructed with at least five samples set of the standard CO(g) solutions in N<sub>2</sub>(g). The calibration curve was always constructed each day before other measurements were conducted (an example of such a curve is in Figure S31).

A set of 54 measurements obtained from 54 independently prepared samples of **1** upon subsequent irradiation was analyzed using a multifactor ANOVA analysis of variance (mixed effects; Figure S7). The effect of the used light source (determined as the difference between the chemical yields of CO(g) produced upon irradiation by either a 300 W lamp or a 3 W lamp) was not found to be statistically significant with a  $p = 0.061$ , whereas the effect of the analytical method (GC-MS vs. GC-RGA) used for CO (g) quantification was found to be statistically significant by a small margin with a  $p = 0.049$ .

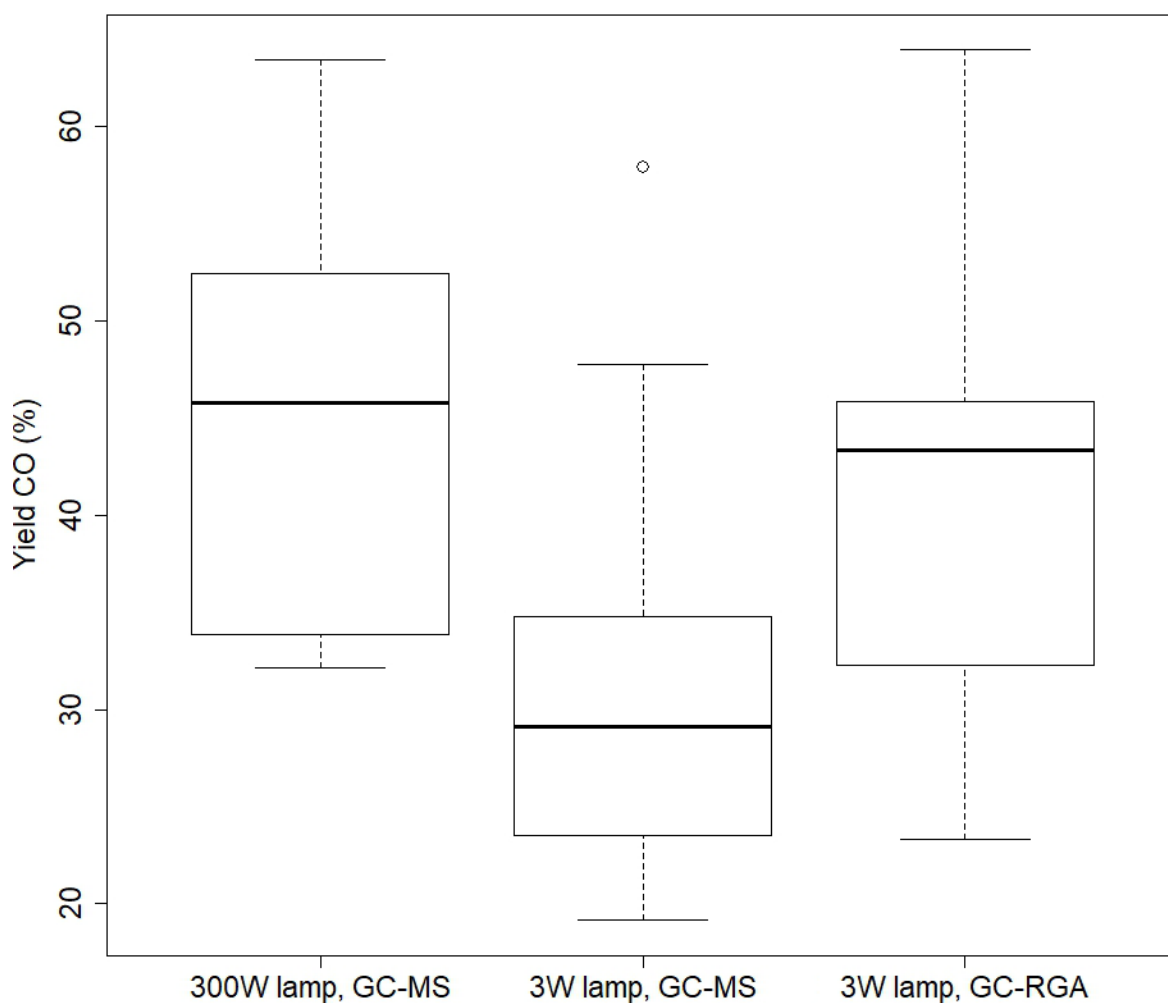


**Figure S7.** Chemical yields of CO(g) released from an aerated aqueous solution of **1** ( $c \sim 1\text{--}30 \times 10^{-5} \text{ mol dm}^{-3}$ ,  $\text{pH} = 7.4$ ,  $I = 0.1 \text{ mol dm}^{-3}$ ) upon irradiation with a)  $3 \times 100 \text{ W}$  white LED reflectors, or b)  $3 \text{ W}$  white LED and determined by a) GC-MS, or b) GC-RGA.

This thorough analysis performed on a wide data set of chemical reactions performed with **1** as a model suggested that all tested solutions concentration (at least in the concentration range from  $c = 1 \times 10^{-5} \text{ mol dm}^{-3}$  to  $c \sim 3 \times 10^{-4} \text{ mol dm}^{-3}$ ), light sources and analytical methods (GC-MS and GC-RGA) does provide similar chemical yields of CO(g) upon full conversion.

## CO(g) Solubility in Protic Organic Solvents

Solubility of CO in solvents and solvent mixtures is an important factor to consider because all analytical methods, both qualitative (such as IR) and quantitative (such as GC with MS or RGA detector) we have employed, are based on the detection of CO in the gaseous phase over the liquid reaction mixture. The information on the CO solubility in pure solvents and especially in more complex liquid matrices are rather scarce in literature. A very good source of these data is IUPAC Solubility data series, Vol. 43.,<sup>30</sup> edited by Cargill and references therein.

Especially to assess the reliability of the quantitative CO(g) analysis, it is helpful to compare the CO(g) yields to the limits of solubility (Table S5).

Out of many possible ways to express gas solubilities and to compare with our own data in a simple way, we decided to use the moles per unit volume solubility,  $c$  (mol dm<sup>-3</sup>). Using this method, solubility is quoted as moles of gas per unit volume of liquid mixture. This is, however, not a common way to express the gas solubility, and the reference data were recalculated to this expression.

For example, the Bunsen coefficient,  $\alpha$ , mainly used in older literature, is defined as the volume of gas reduced to  $T = 273.15$  K and  $p = 1$  atm, which is absorbed by unit volume of solvent (at the temperature of measurement) under a partial pressure of 1 atmosphere. If ideal gas behavior and Henry's law is assumed to be obeyed, the  $\alpha$  could be expressed as:

$$\alpha = \frac{V(g) 273.15}{V(l) T}$$

where  $V(g)$  is the volume of gas absorbed and  $V(l)$  is the original (starting) of an absorbing solvent (or a liquid mixture).

To recalculate the CO(g) solubilities reported in Bunsen coefficients  $\alpha$  to the moles per unit volume  $c$ , we first express the volume of dissolved gas  $V(g)$  as:

$$V(g) = \frac{\alpha V(l) T}{273.15}$$

and calculated the volume of CO dissolved in 1 dm<sup>3</sup> of solution using the known Bunsen coefficient  $\alpha$ . Then we assumed that CO is an ideal gas and calculated its amount as:

$$n = \frac{pV(g)}{RT}$$

using the temperature of the particular experiment and standard pressure ( $p = 101\,325$  Pa), and this is thus the amount of CO(g) that could be dissolved in 1 dm<sup>3</sup> of a solution under the given conditions (Table S4) that equals to the concentration of the gas in a solution  $c$ .

**Table S5.** Solubility of carbon monoxide in various aqueous solutions under standard or near-standard conditions.

Solvent	$T^a$ / K	$\alpha^b$	$V(g)^c$ / dm <sup>3</sup>	$c^d$ / mol dm <sup>-3</sup>
water <sup>31</sup>	298.15	0.02215	0.02418	$9.89 \times 10^{-7}$
sea water (3.16 % salinity) <sup>32</sup>	297.39	0.01867	0.02033	$8.33 \times 10^{-7}$
phosphate buffer <sup>31</sup>	310.15	0.01886	0.02141	$8.41 \times 10^{-7}$
human serum <sup>33</sup>	298.15	0.01830	0.01997	$8.17 \times 10^{-7}$

<sup>a</sup> Temperature of the measurement. <sup>b</sup> Bunsen coefficient. <sup>c</sup> Calculated gas volume of dissolved CO. <sup>d</sup> Solubility of CO in the moles per unit volume.

We did not find similar data for the CO solubility in methanol, but based on a report by Dake and Chaudhari on CO(g) solubilities in organic solvents at high pressures ( $p = 1.5 - 7.2$  MPa) who found out that the solubility of CO in methanol is about 10-fold higher in comparison with water,<sup>34</sup> we decided to use this value as an estimate valid also under our conditions ( $p = 101\,325$  Pa).

Taking into account the typical volumes of solutions in our experiments and an estimated limit of CO solubility in aqueous solutions of  $c = 1 \times 10^{-6} \text{ mol dm}^{-3}$  (see above and Table S5), we calculated the highest limit of the amount of the released CO in a typical reaction setup that remained dissolved in the reaction mixture as a conservative estimate to compare with the released CO(g) determined in the gaseous phase (Table S6).

**Table S6.** Upper estimated limits of CO solubility in the solution in some typical reaction setups tested and used in this work.

Experimental setup	$V(\text{solution})^a$ / mL	$n(\mathbf{1-3})^b$ / mol	$n(\text{CO, dissol.})^c$ / mol	$n(\text{CO, g})^d$ / mol
GC-RGA	0.1	$1 \times 10^{-9}$	$1 \times 10^{-10}$	$1 \times 10^{-9}$
GC-MS	0.5	$1 \times 10^{-7}$	$5 \times 10^{-10}$	$1 \times 10^{-7}$
IR(g)	500	<b>1:</b> $1.3 \times 10^{-5}$ <b>3:</b> $5.1 \times 10^{-6}$	$5 \times 10^{-7}$	<b>1:</b> $1.3 \times 10^{-5}$ <b>3:</b> $5.1 \times 10^{-6}$

<sup>a</sup> Typical volume of a liquid reaction mixture used for quantification of CO(g) released upon photolysis of **1–3**. <sup>b</sup> Typical amount of the starting material (**1–3**) recalculated from the volume and concentration (e.g., for GC-RGA:  $c = 1 \times 10^{-5} \text{ mol dm}^{-3}$ ; for GC-MS:  $c \geq 1 \times 10^{-4} \text{ mol dm}^{-3}$ ; for IR(g):  $c = 1 \times 10^{-5} \text{ mol dm}^{-3}$ ; used in each particular type of experiments. <sup>c</sup> Estimated (based on upper solubility limit of CO solubility in aqueous solutions of  $1 \times 10^{-6} \text{ mol dm}^{-3}$ ) amount of CO able to dissolve in the particular experimental setup (a highest and conservative estimate). <sup>d</sup> Theoretical chemical yield of released CO, if each **1–3** can release 1 eq. of CO upon photolysis.

This suggests that the quantification of CO(g) released upon irradiation in an aqueous solution in the gaseous phase above the reaction mixture using both GC-RGA and GC-MS under the conditions used does not involve significant systematic error (due to CO remaining dissolved in the solution), but the quantification using IR(g) might involve a larger systematic error because the solubility of CO is comparable to the theoretical yield of CO. In methanol, however, the situation is different, and because the solubility of CO in methanol is much higher than that in an aqueous solution, we did not use methanol as a solvent for the CO quantification.

### Analysis of the Non-gaseous Photoproducts in the Reaction Mixture

Upon the loss of carbon monoxide observed concomitantly with irradiation of **1** and its disappearance, we used elemental analysis as a simple semi-quantitative measure to approach the fate of the chromophore with regards to, for example, oxidation by oxygen from air or a nucleophilic attack of water from media.

The solution-phase samples ( $V \sim 0.5$  L) remaining after the measurement of IR(g) with the reaction mixture of non-gaseous photoproducts were transferred to a round bottom flask (1 L), volatiles were removed, and the obtained viscous material was carefully lyophilized. These dry material samples were analyzed by elemental analysis and compared with the elemental composition of the authentic samples of **1-3**. The observed change in the content of carbon does not correspond to a simple loss of one molecule of gaseous CO and suggests that more reaction steps are involved in the photochemical degradation of **1-3**. Plausible explanations involve disproportionation, loss of more gaseous photoproducts, and/or oxidation processes. However, the simple data on the content of carbon and hydrogen in the solid material obtained by lyophilization of reaction mixtures upon irradiation of solutions of **1-3** (results of the elemental analysis of dried product mixtures) and the corresponding photoproduct mixtures does not allow us to rule out any of them.

A set of samples of **1** and [ $^{13}\text{C}_2$ ]-**1** ( $c(\text{dye}) = 3 \times 10^{-5}$  mol dm $^{-3}$ ) in aerated aqueous PBS buffer ( $I = 0.1$  mol dm $^{-3}$ , pH = 7.4) and of **1** ( $c(\text{1}) = 3 \times 10^{-5}$  mol dm $^{-3}$ ) in deoxygenated (argon bubbled for 15 min) aqueous PBS buffer ( $I = 0.1$  mol dm $^{-3}$ , pH = 7.4) in glass vials ( $V(\text{sample}) = 0.5$  mL) were irradiated simultaneously with white-light LED reflectors ( $\lambda_{\text{irr}} = 400\text{--}700$  nm,  $3 \times 100$  W reflector, Figure S83) for 4 days. The course of the reaction was followed using UV-vis absorption spectra, and the irradiation was stopped when the absorption at  $\lambda = 480$  nm (corresponding to the maxima of the major band of fluorescein) reached to baseline.

The reaction mixtures were lyophilized, and the obtained solid residuum was dissolved in a deuterated solvent ( $V = 0.5$  mL), and  $^1\text{H}$  and  $^{13}\text{C}\{^1\text{H}\}$  NMR spectra were measured.

For the MS analysis, the lyophilized samples were prepared using two different methods.

**Method A.** The lyophilized sample was first dissolved in water (1 mL), sonicated (5 min), centrifuged (14000 g, 5 min), and aliquots ( $V = 1$   $\mu\text{L}$ ) were injected into the LC-MS setup and analyzed by Q1-MS in both positive and negative mode (detection in the 92–400  $m/z$  range).

**Method B.** In addition, aliquots were extracted using a solid-phase extraction (SPE) on an X-AW column. Prior to the use, the column was conditioned with methanol ( $2 \times 50$   $\mu\text{L}$ ) and water ( $2 \times 50$   $\mu\text{L}$ ). Then, the sample ( $V = 50$   $\mu\text{L}$ ) was loaded and further washed with water ( $2 \times 50$   $\mu\text{L}$ ). The column was then eluted with ammonium hydroxide ( $2 \times 50$   $\mu\text{L}$ , 5% (w/w) aq). Volatiles were removed from the obtained solution on a SpeedVac and obtained solid residuum dissolved in water (100  $\mu\text{L}$ ) and analyzed by LC-MS. The chromatograms showed several major peaks for all three samples and upon using both sample preparation methods (dissolution; SPE). The chromatograms were compared with the chromatograms of the blank samples (water processed using the same procedure).

**Results.** In all six analyzed samples, we found several major peaks in the chromatograms and more than ten minor peaks (the peaks were identified in comparison with the blank samples of water). Comparison of the chromatograms showed that method A (SPE) yielded samples with fewer individual compounds, thus it is more discriminating than method B (e.g., compare Figures S59 and S74). The chromatograms obtained upon analysis of photoproducts mixtures obtained upon irradiation of aerated samples of **1** and [ $^{13}\text{C}_2$ ]-**1** were found to be nearly identical (e.g., compare Figures S59 and S64). The chromatograms resulting from the analysis of

photoproduct mixtures upon irradiation of degassed samples of **1** show more photoproducts (by both methods A and B, e.g., see Figures S69 and S80).

From the mass spectral data, we were able to identify only two compounds, phthalic acid as a photoproduct (Figures S60, S64, and S75) and fluorescein (**1**; Figure S78), as a remaining unreacted starting material. Unfortunately, we have not been able to identify any other photoproducts among the observed compounds.

The direct comparison of MS spectra of phthalic acid as a photoproduct obtained upon irradiation of aerated solutions of **1** and [ $^{13}\text{C}_2$ ]-**1** shows the difference in  $m/z$  of +1 (Figures S60 and S65), which corroborates with the presence of one labeled carbon atom in the molecule of **1** and supports the release of phthalic acid formally following reverse process to condensation of phthalic acid and resorcinol to form **1**.

Among the non-identified photoproducts we were able to observe, some pairs that show identical  $m/z$  patterns of compounds yielded from **1** and [ $^{13}\text{C}_2$ ]-**1**, such as the product with a major signal at ~13.5 min ( $m/z$  214; Figures S62 and S67), pairs that show the consistent difference by +1 for photoproducts from **1** in comparison to that from [ $^{13}\text{C}_2$ ]-**1** (e.g.  $m/z$  214; Figures S63 and S68) for the product with a major signal at ~16.2 min. Other photoproducts, such as that with a major signal at ~11.6 min, display several major peaks in the MS spectrum. The comparison of the corresponding photoproducts obtained upon irradiation of **1** and [ $^{13}\text{C}_2$ ]-**1** revealed that some of them have identical  $m/z$  signals, others are shifted by +1  $m/z$ , and some are split into two signals (one with original  $m/z$  value and the other with +1  $m/z$ ), which suggested that this compound underwent isotope scrambling or is a product of some desymmetrization degradation.

The comparison of chromatograms of the photoproducts mixtures obtained upon irradiated aerated and degassed solutions of **1** showed that phthalic acid is formed as a stable photoproduct only under aerated conditions (peak at ~10.5 min; Figure S59) but not under degassed conditions (Figure S69). The photoproduct with  $m/z$  187 (peak at ~11.6 min) is present under both conditions (Figures S59 and S64). We observed several other photoproducts obtained under the degassed conditions (e.g., at ~13.6 min and at ~14.5 min), that are not present or only as minor constituents of the mixture obtained upon irradiation of the aerated solution of **1**.

**Analysis of Possible Photoproducts.** In order to simplify the analysis of obtained LC-MS data, we hypothesized possible disconnections of the molecule of **1** and kept the fragment of phthalic acid untouched (Figure S8a). Using these disconnections, we hypothesized an array of plausible photoproducts with different complexity (Figure S8b) and compared their  $m/z$  values with those in the measured spectra (e.g., Figures S60–S80). However, we could not identify any further photoproducts except phthalic acid (see above and the main text).

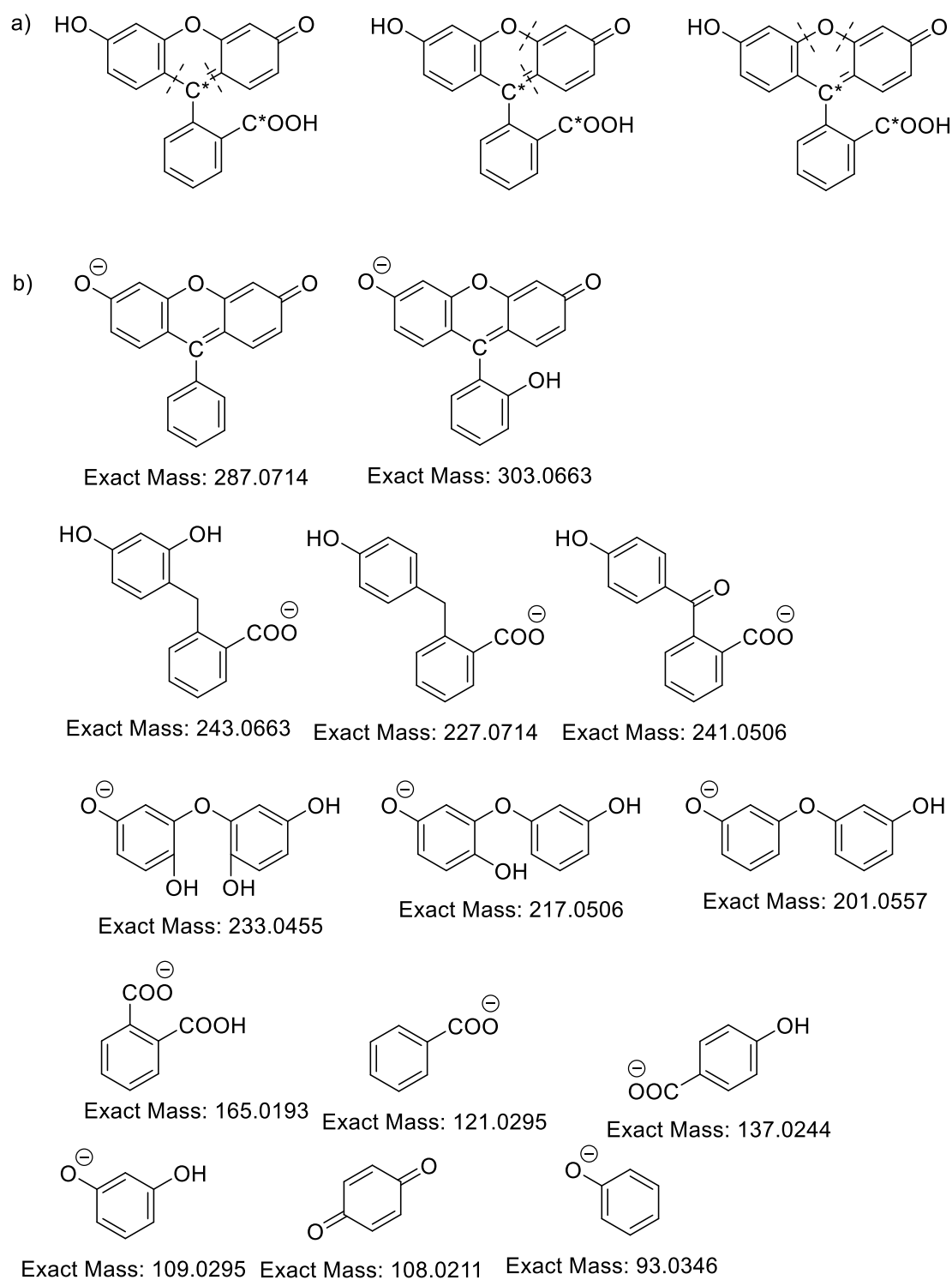


**Figure S8.** Analysis of possible products of degradation of **1**, a) disconnections of the xanthene scaffold with regards to the release of phthalic acid; and b) possible products (structures relevant for a negative MS mode are shown).

To conclude our attempts to identify the non-gaseous photoproducts, we used an array of analytical and spectroscopic techniques and identified CO and phthalic acid as photoproducts of degradation of **1**. Based on the data obtained from  $^1\text{H}$  and  $^{13}\text{C}$  NMR (Figures S32–S38) and ESI-MS (Figures S59–S80) analyses of irradiated aqueous solutions of **1** and  $^{13}\text{C}_2$ -**1**, we identified phthalic acid as a stable photoproduct present in the reaction mixture. Our

investigation of other results from spectroscopies and elemental analysis of the lyophilized reaction mixture was not conclusive, and we could not assign structures to any other observed signals corresponding to the final photoproducts.

### Photochemical Reactivity of Fluorescein Cation

We studied the photodegradation of fluorescein acid-base forms by photodissociation spectroscopy in the gas phase. Unfortunately, our experimental setup hindered our attempts to study negatively charged fluorescein anion and dianion. Thus, we were able to get reasonable experimental data only for isolated fluorescein cation  $1^+$ . Previous experiments using a low-resolution light source featured the absorption maximum of the isolated fluorescein cation at 420–430 nm,<sup>35</sup> which was later refined to 425 nm.<sup>36</sup> Our experimental setup enables us to obtain spectra of isolated fluorescein cations in high-resolution (linewidth  $<0.1 \text{ cm}^{-1}$ ).

The helium-tagging spectrum of isolated fluorescein cation at 3 K features the 0–0 transition at 420.8 nm with a relatively low intensity (Figure , red trace), especially in comparison with previously studied rhodamine ions.<sup>37</sup> This suggests that fluorescein undergoes a more sizable nuclear distortion upon excitation than rhodamine derivatives. Interestingly, the calculated angle between benzene and xantheno planes in  $S_1$  state, which is  $111^\circ$ , markedly differs from the angle in the  $S_0$  state, which is  $90^\circ$ . Unfavorable overlap between  $S_0$  and  $S_1$  geometries may thus account for the reduced intensity of the 0–0 and several other vibronic transitions, which we detected in the helium-tagging experiment.

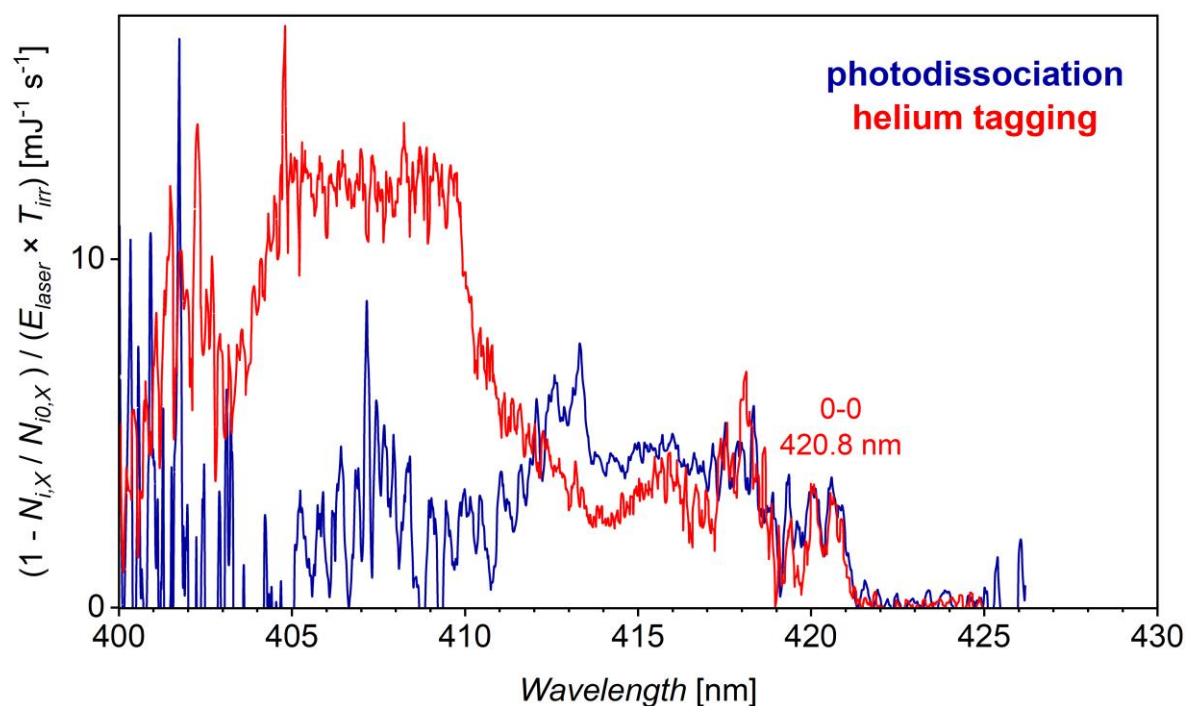


**Figure S9.** Comparison of photodissociation and helium-tagging spectra of fluorescein cation  $1^+$  measured at 3 K. The intensity of the spectra was normalized to the energy of the laser ( $E_{laser}$ ) and to the irradiation time ( $T_{irr}$ ). Please note that the signal of the helium-tagging spectrum is saturated between 405 and 410 nm due to the increase in the power output of the laser. Below  $\sim 405$  nm, the photodissociation signal is biased due to a significant decrease both in photodissociation yield and in laser power.

The second notable feature of the helium-tagging spectrum is the line broadness (in this case not limited by the laser linewidth), which can also result from an unfavorable overlap of  $S_0$  and  $S_1$  geometries resulting in a broad Franck-Condon envelope and/or from a short lifetime of the excited state. The nature of the excited state is most likely rather complicated. A previous study showed that fluorescein emits no detectable fluorescence in the gas phase, even though fluorescein and its derivatives are highly fluorescent in solution. Hence, the dominant deexcitation pathway in the gas phase is most likely a different process with an unclear nature;

proton transfer has been suggested to occur in the excited state.<sup>35</sup> This is particularly puzzling considering the relevance of deexcitation for the helium-tagging process and for its mechanism in particular.

Upon irradiation in the gas phase, fluorescein cation exhibits numerous fragmentation channels, such as the loss of 46 mass units ( $m/z$  287, Figure S10), which corresponds to the dissociation of formic acid from the carboxylate moiety and which is the major fragmentation channel. A large number of fragmentation channels with similar intensities apparently stems from several similarly strong chemical bonds, which dissociate in the excited fluorescein cation. However, the efficiency of individual fragmentation channels, which is rather low, could impede photodissociation experiments. Hence, instead of monitoring several dissociation channels simultaneously, the depletion of the parent fluorescein signal ( $m/z$  333) was monitored during photodissociation experiment. The photodissociation spectrum measured at 3 K (Figure S9, blue trace) is shown together with the helium-tagging spectrum for comparison. The positions of the 0–0 transition (420.8 nm) and several subsequent absorption bands are virtually identical in both spectra. Yet both spectra start to deviate below *ca.* 413 nm; the PD spectrum retains vibrational resolution, whereas the signal of the helium-tagging spectrum is saturated due to an increase in laser power and thus lacks any vibronic structure. The reason for such difference remains unknown and requires further experiments for clarification.

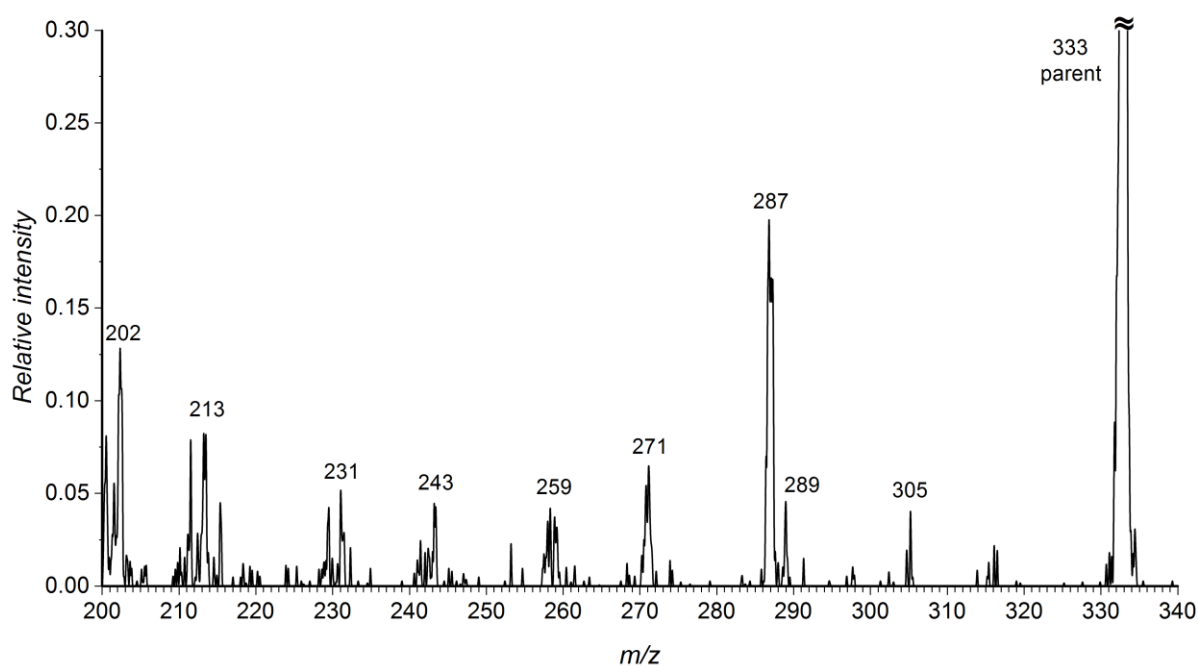


**Figure S10.** Photodissociation mass spectrum of fluorescein cation  $1^+$  ( $m/z$  333) recorded after irradiation with laser light ( $\lambda_{em} = 414$  nm, 250  $\mu$ J) at 295 K. Please note that the laser power used for the actual spectra measurements was decreased by more than 10-fold to avoid photodissociation signal saturation.

## Thermal Chemistry

As the samples sometimes warm up during irradiation, we wanted to be sure that the observed products (especially CO) are solely photoproducts and not products of thermal decomposition of dyes.

Thermal decomposition of **1-3** was studied by thermogravimetric analysis coupled with a differential scanning calorimetry upon heating of the samples up to 500 °C in dry N<sub>2</sub>(g) atmosphere, to prevent secondary oxidation, with IR analysis of the gaseous phase over the sample including the gaseous products released during heating. **1** lost ~9% of the mass upon heating in the range of 50–200 °C, and no change was observed until 420 °C when it started losing mass again leading to residual mass of 85.4 % at 500 °C (Figure S48). The gaseous phase IR spectrum was dominated by a strong signal identified as carbon dioxide and accompanied by water vapors (Figure S50). **2** lost ~8% of the mass upon heating in the range of 50-150 °C and additional 2.5 % in the 220-300 °C range and then loss mass rapidly over 300 °C leading to a residual mass of 66.7 % at 500 °C (Figure S52). The gaseous phase IR spectrum was similar to that observed for **1**, and in addition to the major CO<sub>2</sub> bands and minor H<sub>2</sub>O bands, we also observed minor bands corresponding to carbon monoxide with an intensity comparable to that of water (Figure S54). And last, **3** was found to lost ~7% in the range of 50-150 °C and showed no mass loss upon further heating to 320 °C and then started a massive mass loss of ~46%, which leaves the residual mass of only 44.4% at 500 °C (Figure S56). In the gaseous phase IR spectrum, we identified major bands corresponding to CO<sub>2</sub> and water vapor (with about half intensity in comparison to carbon dioxide). Upon heating of all three **1-3**, we observed decarboxylation as a major degradation pathway, accompanied by a release of only a small amount of carbon monoxide released only from **2** through an unknown process.

The thermal decomposition pathways of **1-3** are different in the profile of observed gaseous products in comparison with the photochemical decomposition. Decarboxylation was observed as a major thermal decomposition reaction channel, similarly to that observed for 3,6-dihydroxy-xanthene-9-carboxylic acid.<sup>38</sup>

**Figure S11.** Change of the chemical yields of photoproducts (phthalic acid, black square; formic acid, red circle; all as eq.) with progressing conversion (represented as degradation of the starting dye) of **1**, measured in a solution of **1** ( $c \sim 6 \times 10^{-3} \text{ mol dm}^{-3}$ ) and phthalic and formic acids quantified by  $^1\text{H NMR}$ . The reaction mixture was followed upon irradiation with  $3 \times 100 \text{ W}$  white LED reflectors (Figure S83) as determined by quantitative  $^1\text{H NMR}$ .

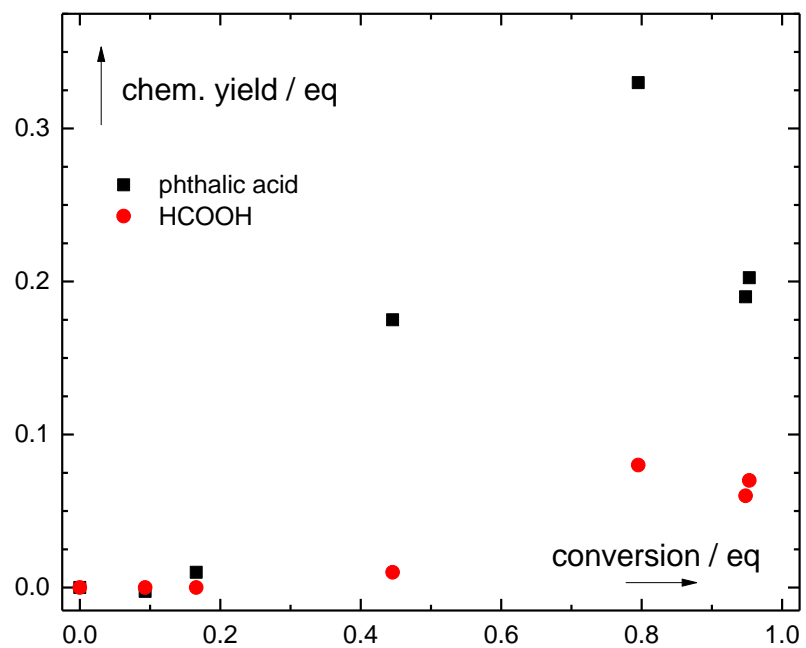


**Figure S12.** Time evolution of the chemical yields of photoproducts (phthalic acid, black square; formic acid, red circle; all as eq.) with progressing conversion (represented as degradation of the starting dye) of **1**, measured in a solution of **1** ( $c \sim 6 \times 10^{-3} \text{ mol dm}^{-3}$ ) and phthalic and formic acids quantified by  $^1\text{H NMR}$ . The reaction mixture was followed upon irradiation with  $3 \times 100 \text{ W}$  white LED reflectors (Figure S83) as determined by quantitative  $^1\text{H NMR}$ .

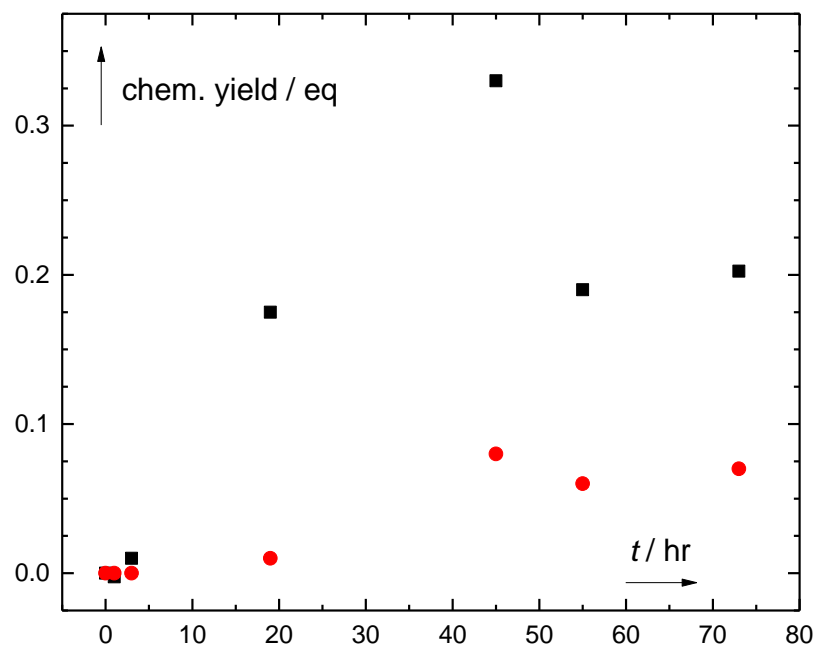


**Figure S13.** Change of the chemical yields of photoproducts (phthalic acid, black square; formic acid, red circle; and carbon monoxide, blue triangle; all as eq.) with progressing conversion (represented as degradation of the starting dye) of **2**, measured in two independent solutions, a) **2** ( $c \sim 6 \times 10^{-3} \text{ mol dm}^{-3}$ ) and phthalic and formic acids quantified by  $^1\text{H NMR}$ , and b) **2** ( $c \sim 1.6 \times 10^{-5} \text{ mol dm}^{-3}$ ) and CO quantified by GC-MS from headspace. Both reaction mixtures were followed upon irradiation with  $3 \times 100 \text{ W}$  white LED reflectors (Figure S83) as determined by a) quantitative  $^1\text{H NMR}$  and b) by UV-vis spectroscopy of simultaneously irradiated solutions of dyes.

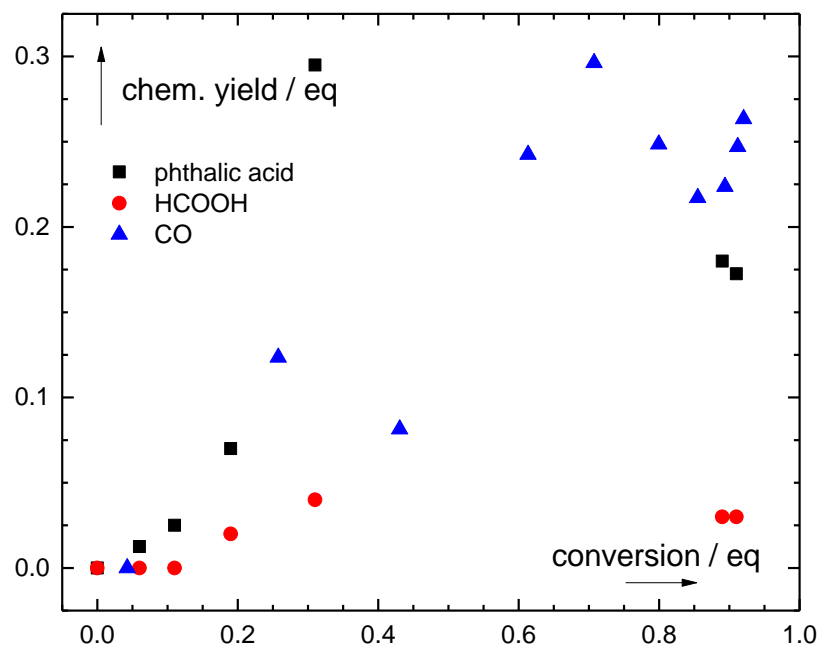


**Figure S14.** Time evolution of the chemical yields of photoproducts (phthalic acid, black square; formic acid, red circle; and carbon monoxide, blue triangle; all as eq.) with progressing conversion (represented as degradation of the starting dye) of **2**, measured in two independent solutions, a) **2** ( $c \sim 6 \times 10^{-3} \text{ mol dm}^{-3}$ ) and phthalic and formic acids quantified by  $^1\text{H}$  NMR (left panel), and b) **2** ( $c = 1 \times 10^{-5} \text{ mol dm}^{-3}$ ) and CO quantified by GC-MS from headspace (right panel). Both reaction mixtures were followed upon irradiation with  $3 \times 100 \text{ W}$  white LED reflectors (Figure S83) as determined by a) quantitative  $^1\text{H}$  NMR and b) by UV-vis spectroscopy of simultaneously irradiated solutions of dyes.

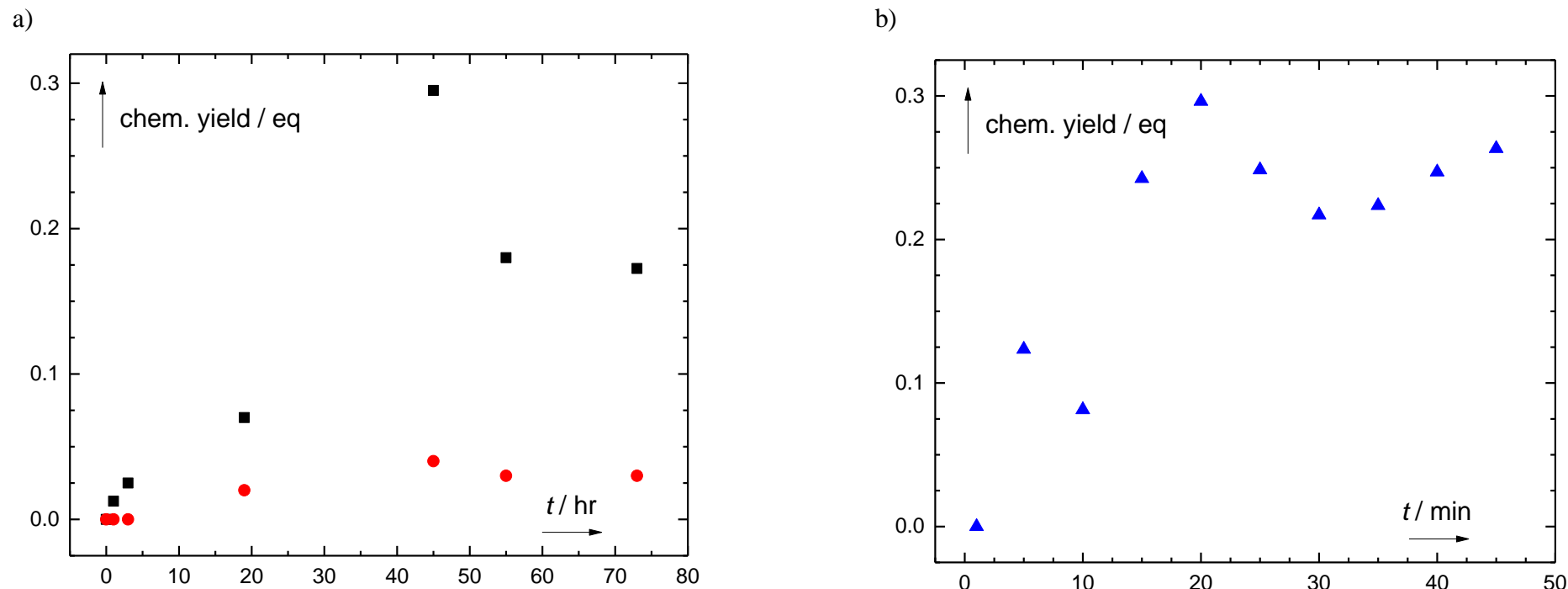


**Figure S15.** Change of the chemical yields of photoproducts (phthalic acid, black square; formic acid, red circle; and carbon monoxide, blue triangle; all as eq.) with progressing conversion (represented as degradation of the starting dye) of **3**, measured in two independent solutions, a) **3** ( $c \sim 6 \times 10^{-3} \text{ mol dm}^{-3}$ ) and phthalic and formic acids quantified by  $^1\text{H NMR}$ , and b) **3** ( $c \sim 1.6 \times 10^{-5} \text{ mol dm}^{-3}$ ) and CO quantified by GC-MS from headspace. Both reaction mixtures were followed upon irradiation with  $3 \times 100 \text{ W}$  white LED reflectors (Figure S83) as determined by a) quantitative  $^1\text{H NMR}$  and b) by UV-vis spectroscopy of simultaneously irradiated solutions of dyes.

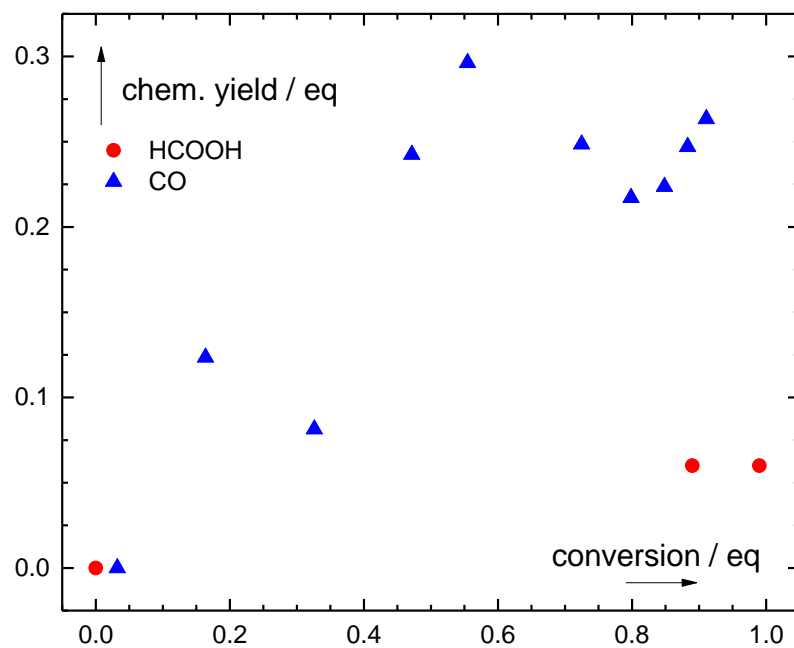
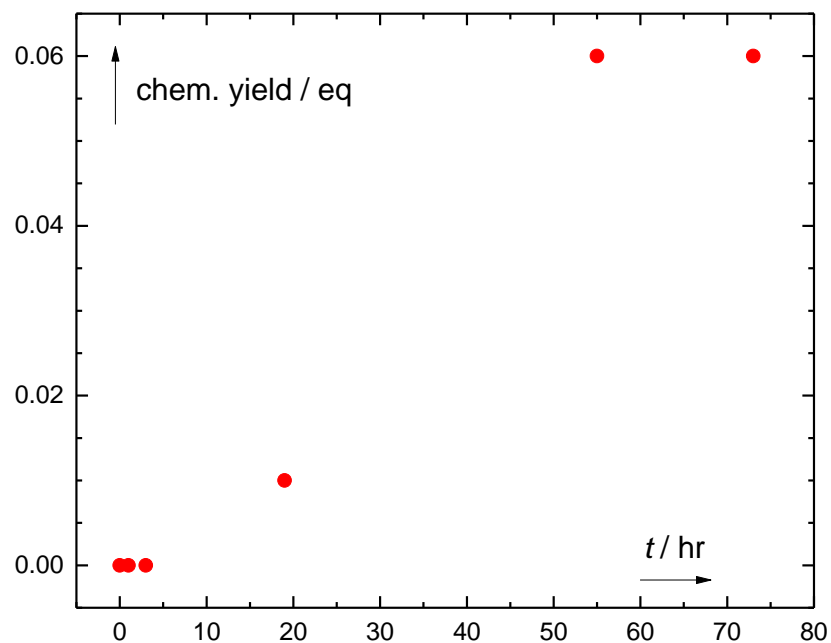


**Figure S16.** Time evolution of the chemical yields of photoproducts (phthalic acid, black square; formic acid, red circle; and carbon monoxide, blue triangle; all as eq.) with progressing conversion (represented as degradation of the starting dye) of **3**, measured in two independent solutions, a) **3** ( $c = 6 \times 10^{-3} \text{ mol dm}^{-3}$ ) and phthalic and formic acids quantified by  $^1\text{H}$  NMR (left panel), and b) **3** ( $c = 1 \times 10^{-5} \text{ mol dm}^{-3}$ ) and CO quantified by GC-MS from headspace (right panel). Both reaction mixtures were followed upon irradiation with  $3 \times 100 \text{ W}$  white LED reflectors (Figure S83) as determined by a) quantitative  $^1\text{H}$  NMR and b) by UV-vis spectroscopy of simultaneously irradiated solutions of dyes.

a)



b)

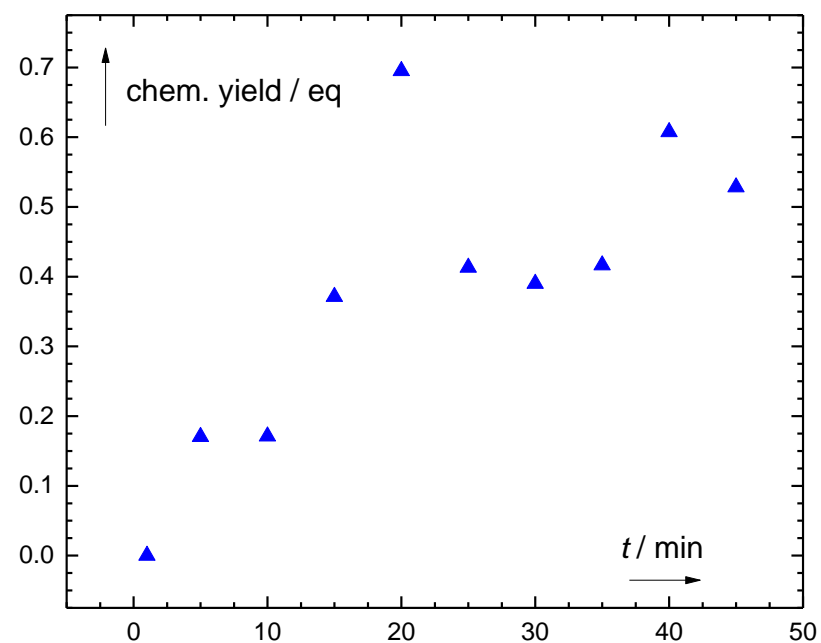
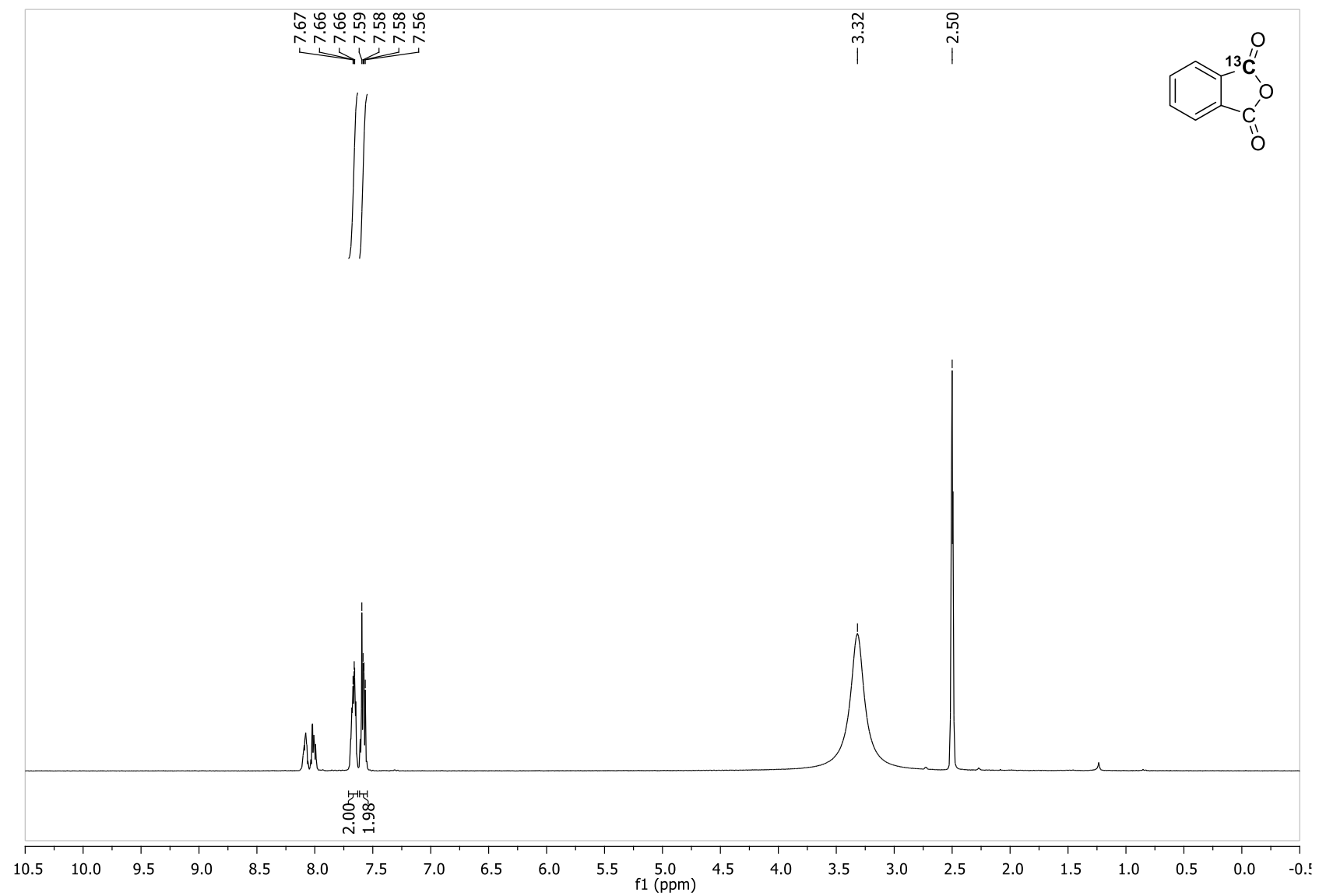
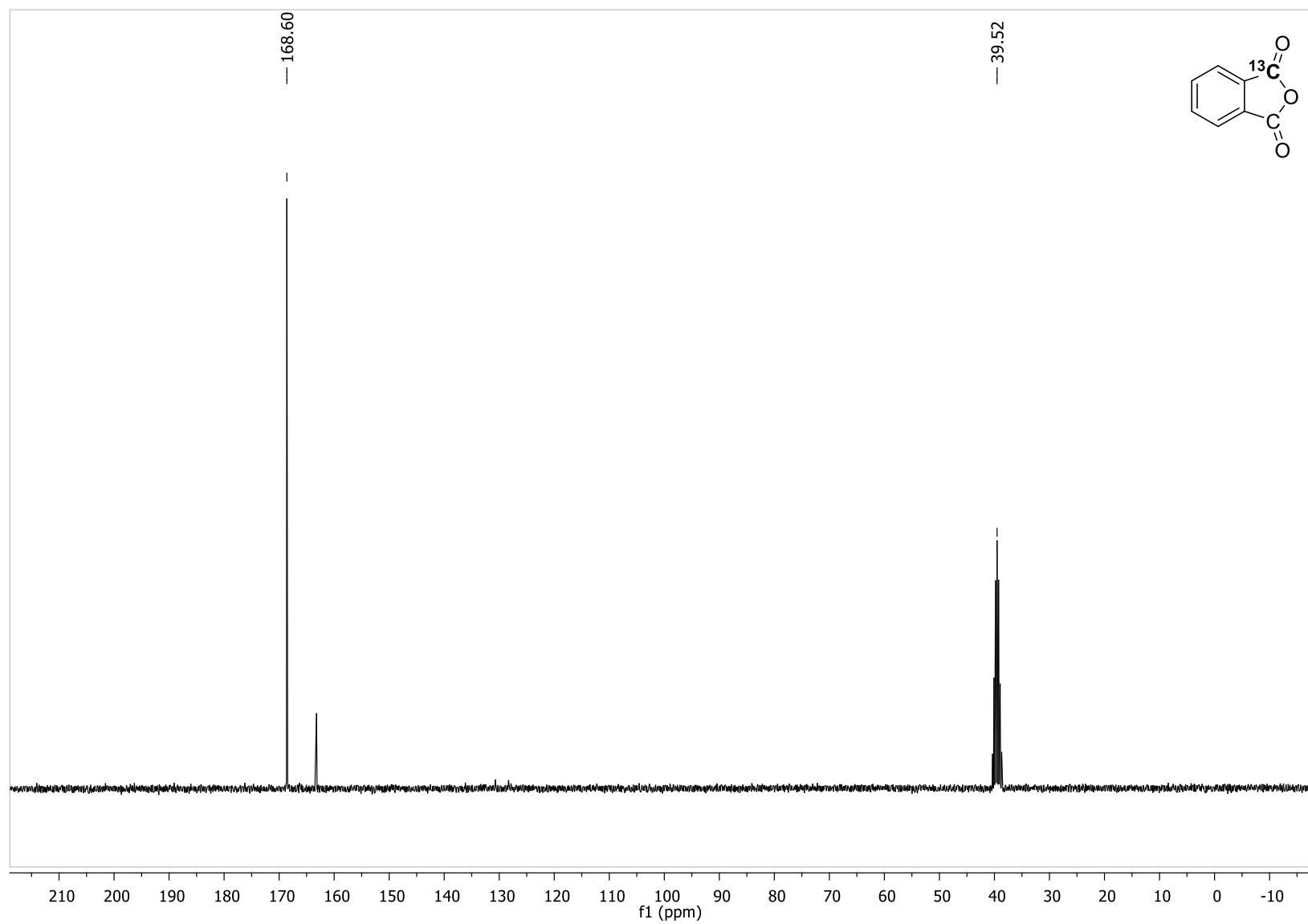


Figure S17.  $^1\text{H}$  NMR (DMSO- $d_6$ , 300 MHz): [ $^{13}\text{C}$ ]-phthalic anhydride



**Figure S18.**  $^{13}\text{C}\{^1\text{H}\}$  NMR (DMSO- $d_6$ , 75 MHz):  $[^{13}\text{C}]$ -phthalic anhydride



**Figure S19.** IR (ATR,  $\text{cm}^{-1}$ ): [9- $^{13}\text{C}$ ][carboxy- $^{13}\text{C}$ ]-fluorescein ([ $^{13}\text{C}_2$ ]-**1**)

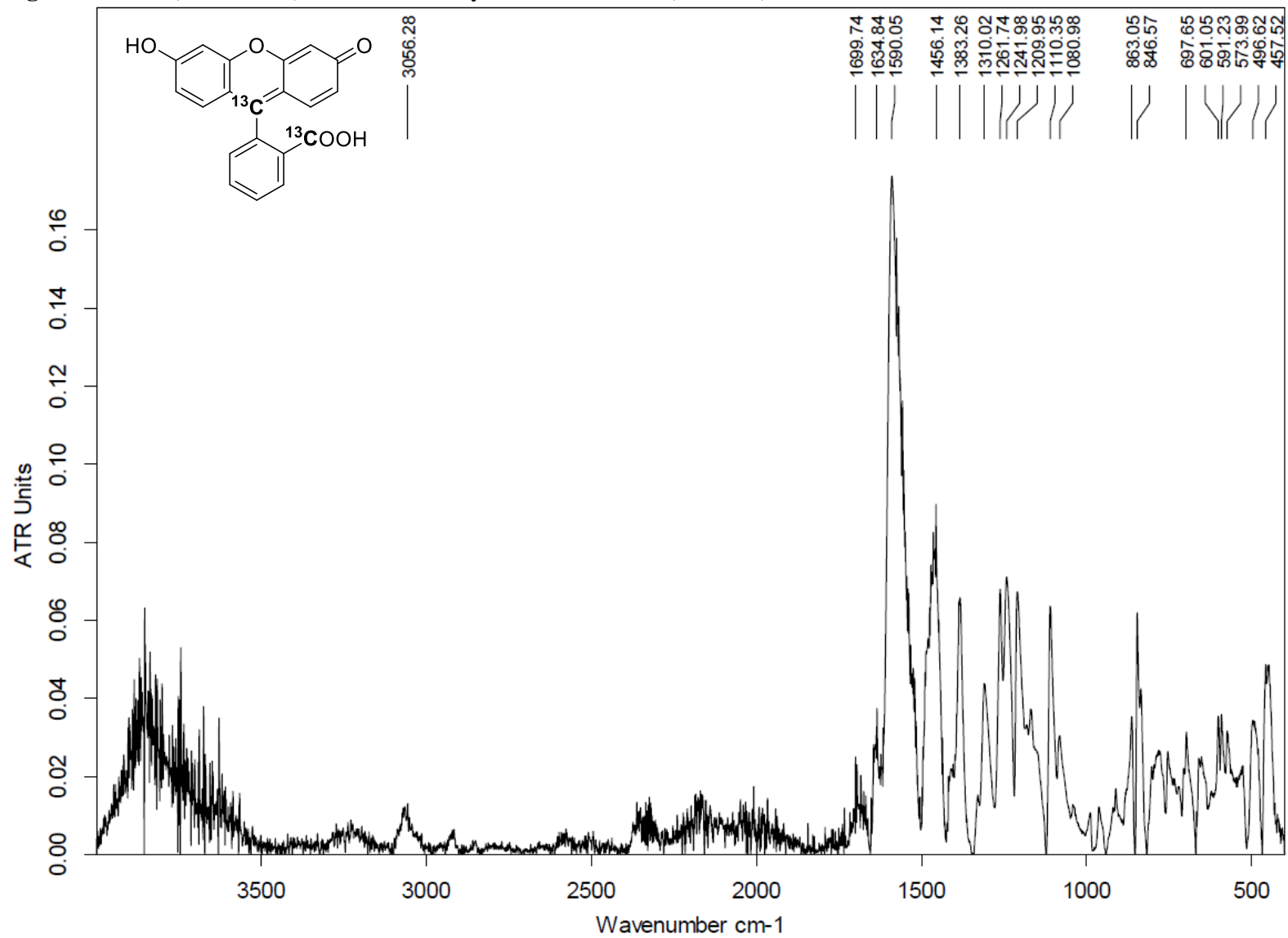


**Figure S20.** Normalized IR (ATR,  $\text{cm}^{-1}$ ):  $[9\text{-}^{13}\text{C}][\text{carboxy-}^{13}\text{C}]\text{-fluorescein}$  ( $[^{13}\text{C}_2]\text{-1}$ ) and fluorescein (**1**)

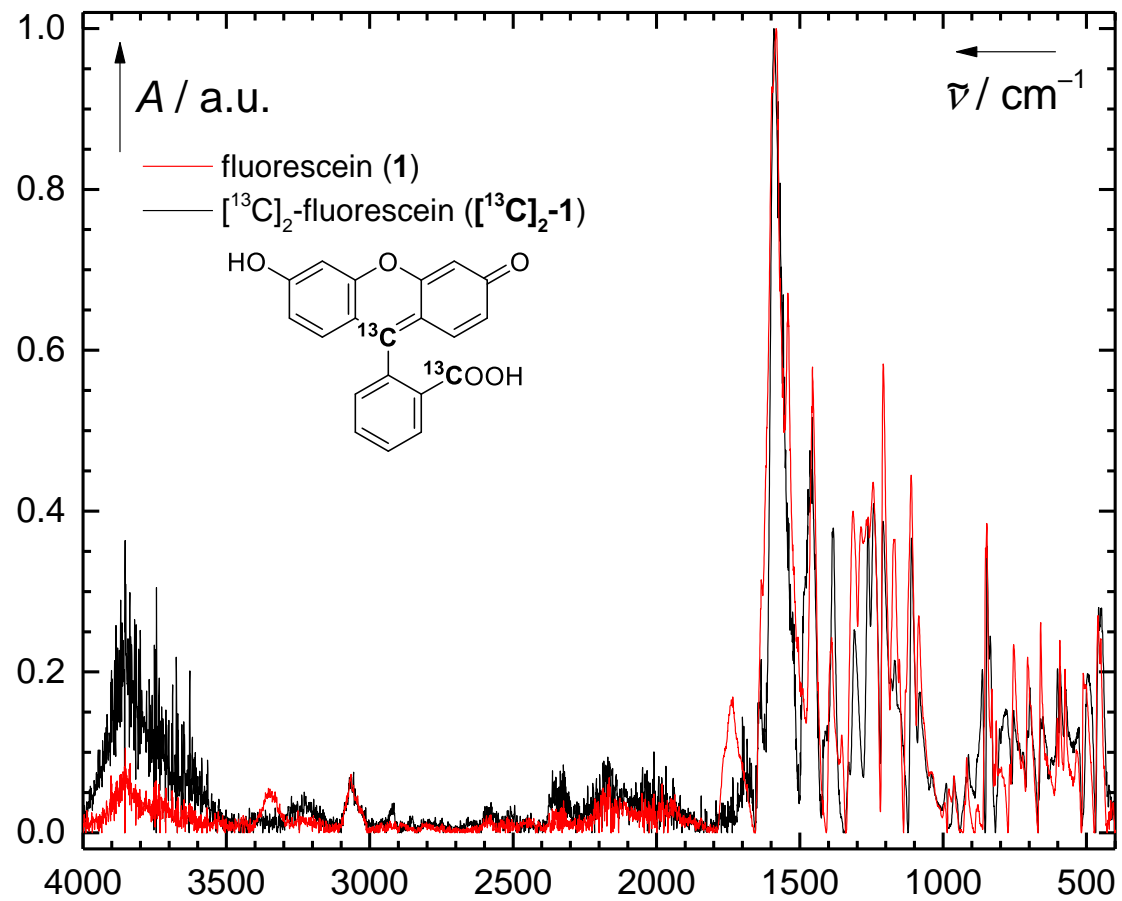


**Figure S21.**  $^1\text{H}$  NMR (500 MHz,  $\text{DMSO-}d_6$ ):  $[9-^{13}\text{C}][\text{carboxy-}^{13}\text{C}]\text{-fluorescein}$  ( $[^{13}\text{C}_2]\text{-1}$ )

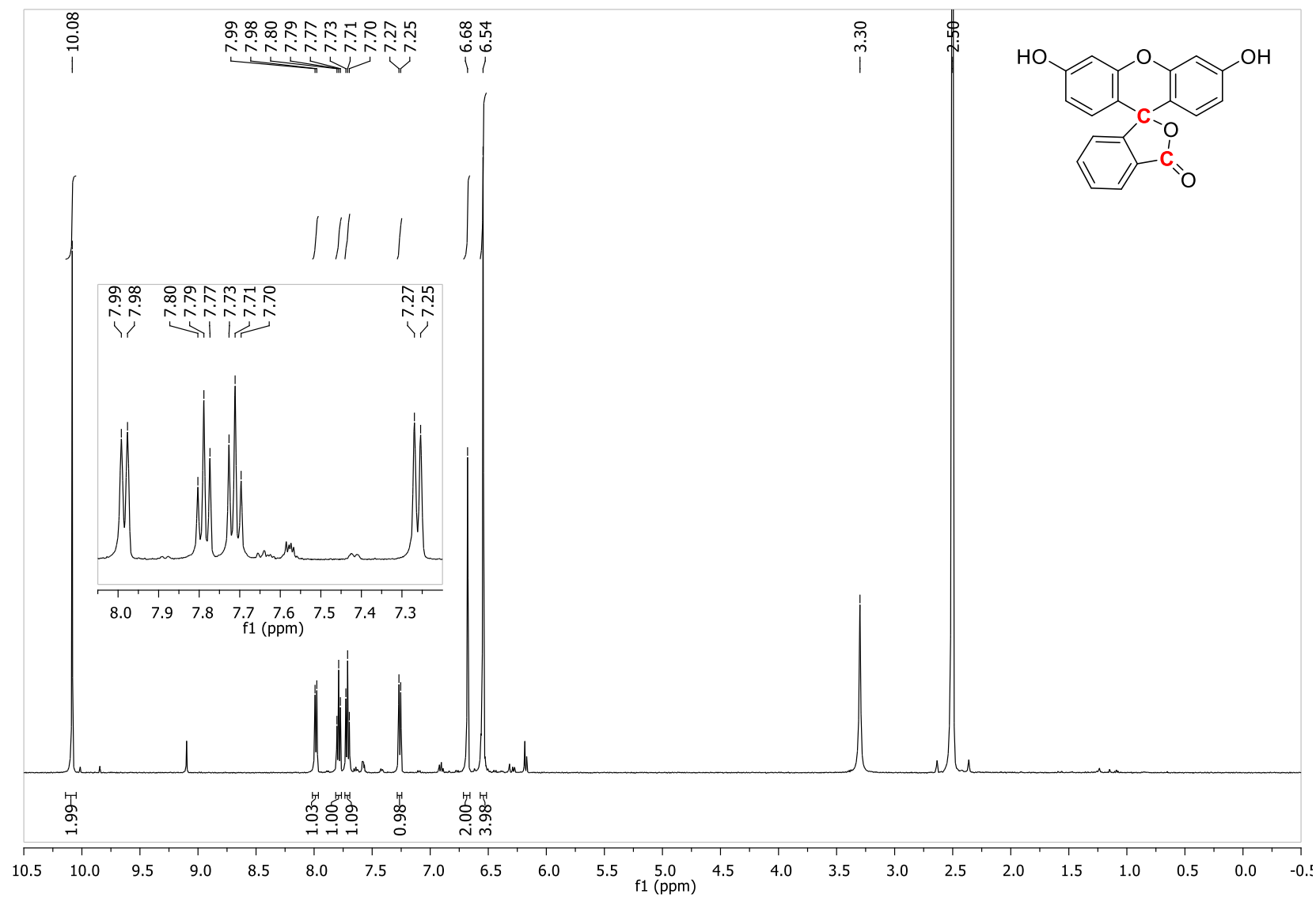
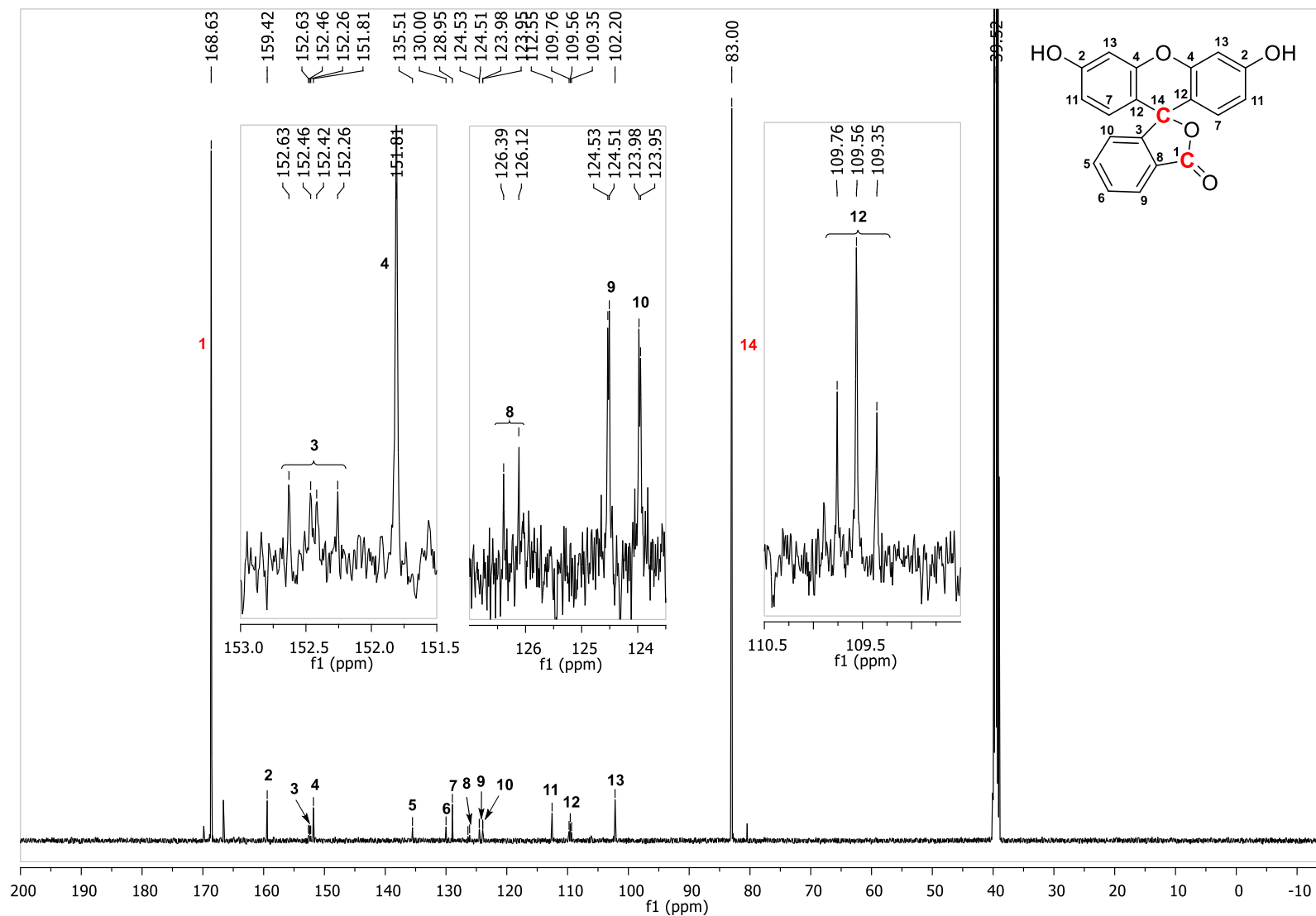


**Figure S22.**  $^{13}\text{C}\{^1\text{H}\}$  NMR (125 MHz,  $\text{DMSO-}d_6$ ):  $[9-^{13}\text{C}][\text{carboxy-}^{13}\text{C}]\text{-fluorescein}$  ( $[^{13}\text{C}_2]\text{-1}$ )



Note: Used numbering does not follow the IUPAC rules, but numbers increase with the increasing upfield signals position.

**Figure S23.**  $^1\text{H}$ - $^{13}\text{C}$  HMBC NMR (500 MHz,  $\text{DMSO-}d_6$ ):  $[\text{}^{13}\text{C}]$ [carboxy- $^{13}\text{C}$ ]-fluorescein ( $[\text{}^{13}\text{C}_2]$ -1)

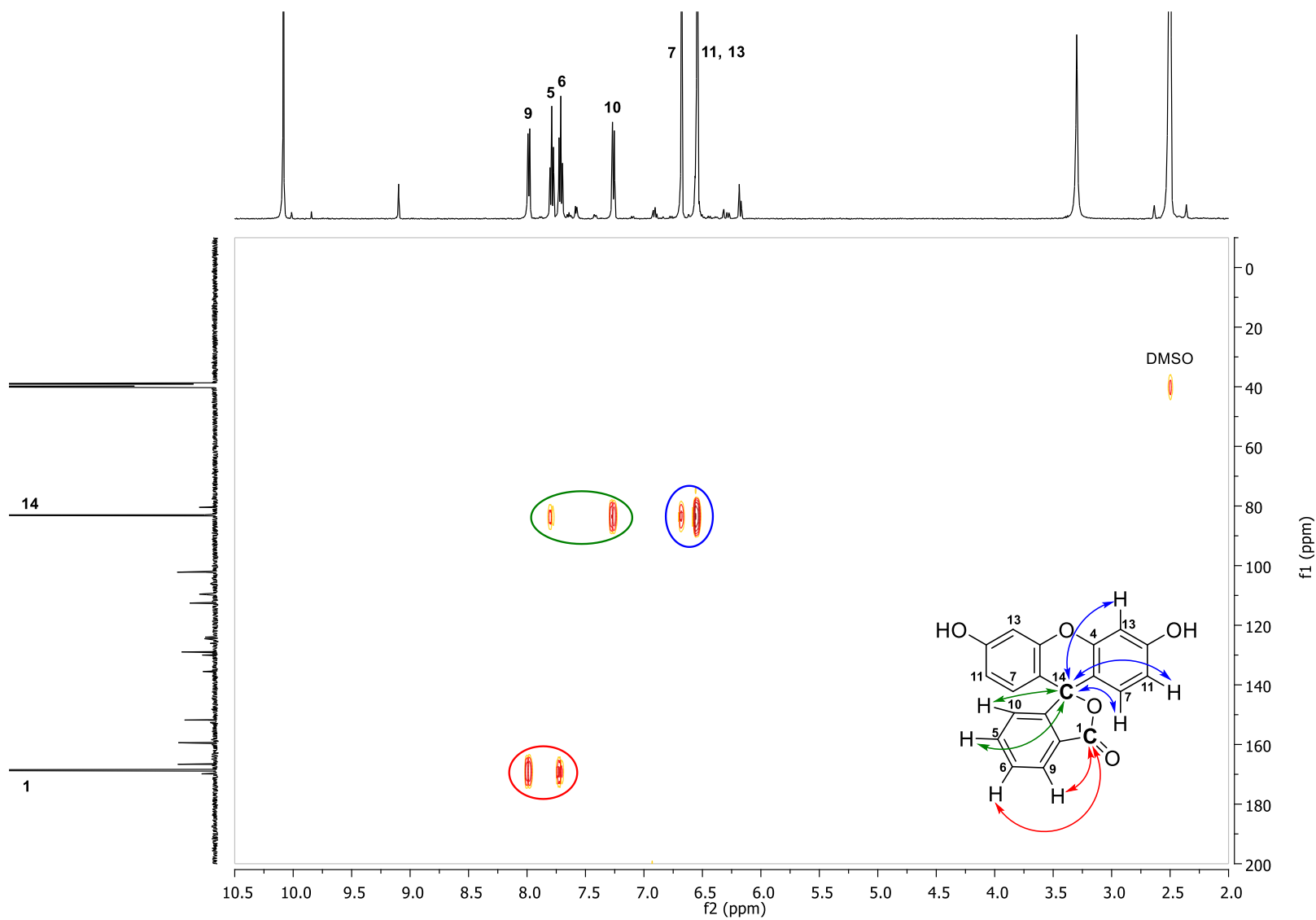


**Figure S24.** Normalized fluorescence excitation (black line;  $\lambda_{em} = 590$  nm) and normalized emission (red line;  $\lambda_{ex} = 440$  nm) spectra of fluorescein (**1**;  $c \sim 1 \times 10^{-5}$  mol dm $^{-3}$ ) in PBS (pH = 7.4,  $I = 0.1$  mol dm $^{-3}$ ) solution at  $(23 \pm 1)$  °C.

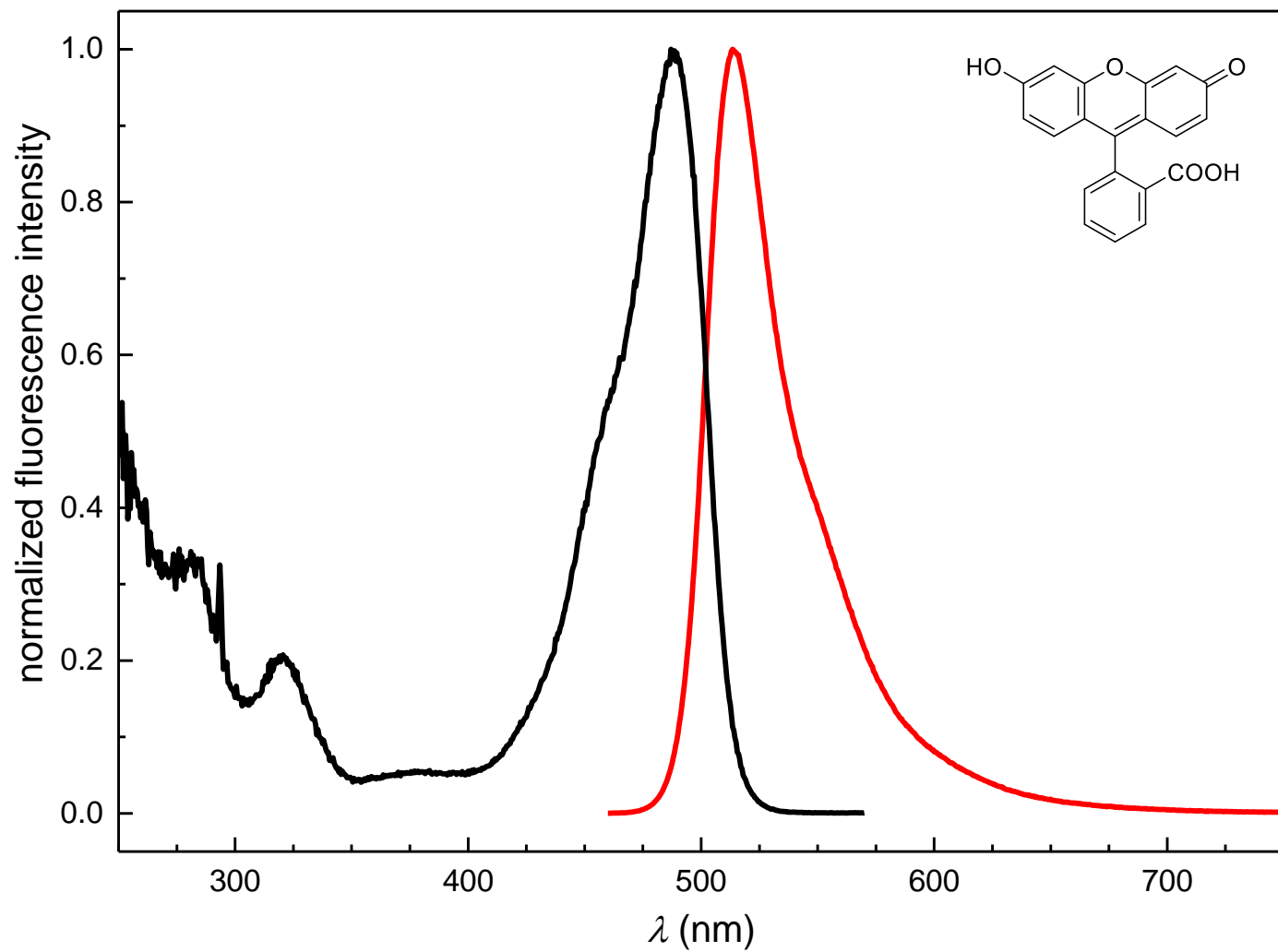


**Figure S25.** Normalized fluorescence excitation (black line;  $\lambda_{em} = 600$  nm) and normalized emission (red line;  $\lambda_{ex} = 460$  nm) spectra of eosin Y (**2**;  $c \sim 1 \times 10^{-5}$  mol dm $^{-3}$ ) in PBS (pH = 7.4,  $I = 0.1$  mol dm $^{-3}$ ) solution at  $(23 \pm 1)$  °C.

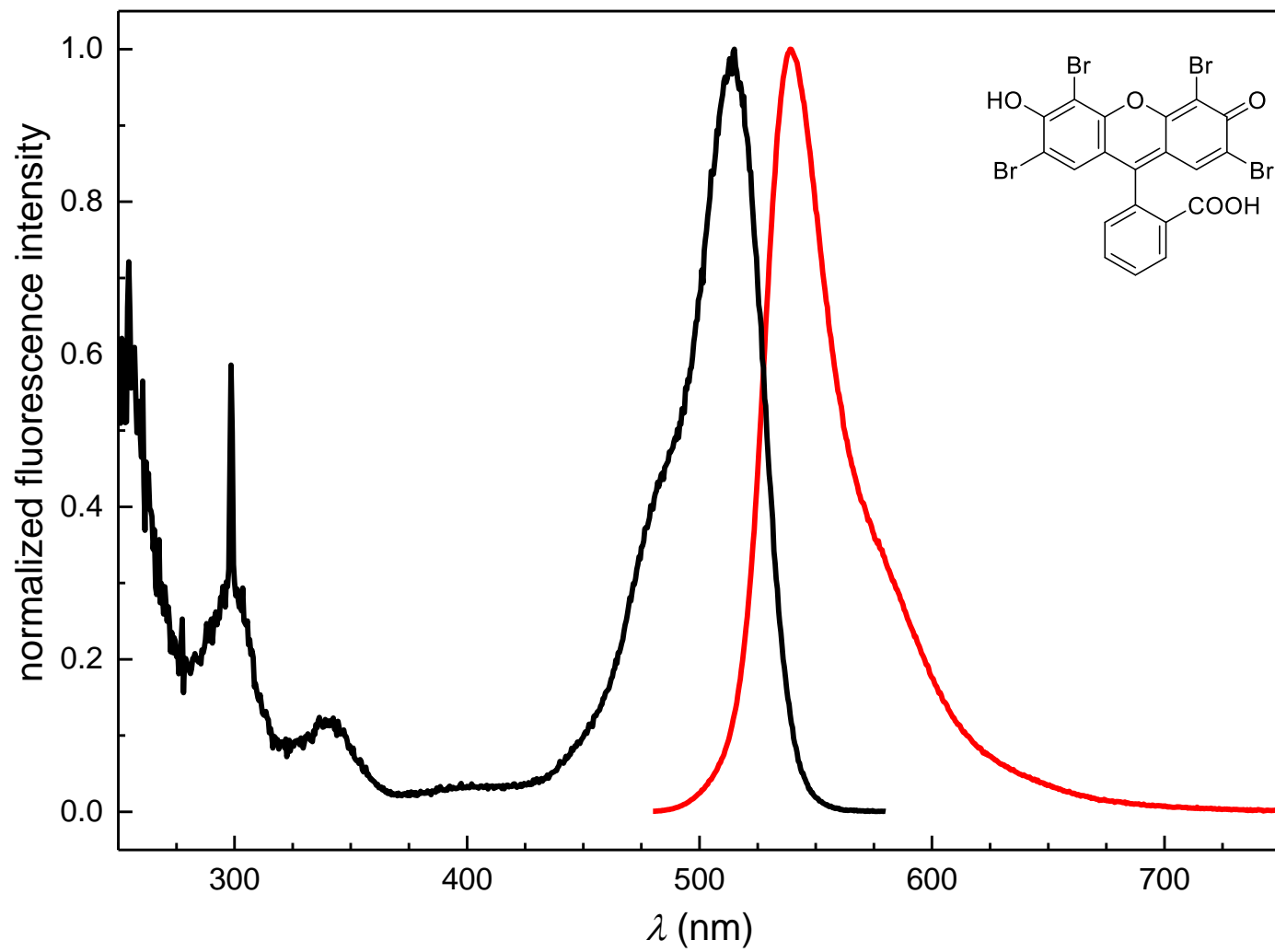


**Figure S26.** Normalized fluorescence excitation (black line;  $\lambda_{em} = 620$  nm) and normalized emission (red line;  $\lambda_{ex} = 490$  nm) spectra of rose bengal (**3**;  $c \sim 1 \times 10^{-5}$  mol dm $^{-3}$ ) in PBS (pH = 7.4,  $I = 0.1$  mol dm $^{-3}$ ) solution at  $(23 \pm 1)$  °C. The sample was measured in degassed ( $3\times$  pump-freeze-thaw) solution, to detect both fluorescence ( $\lambda_{max} = 568$  nm) and phosphorescence ( $\lambda_{max} = 731$ ) nm. Note: The negative peaks at  $\sim 655$  nm and at  $\sim 790$  nm are instrumental artifacts.

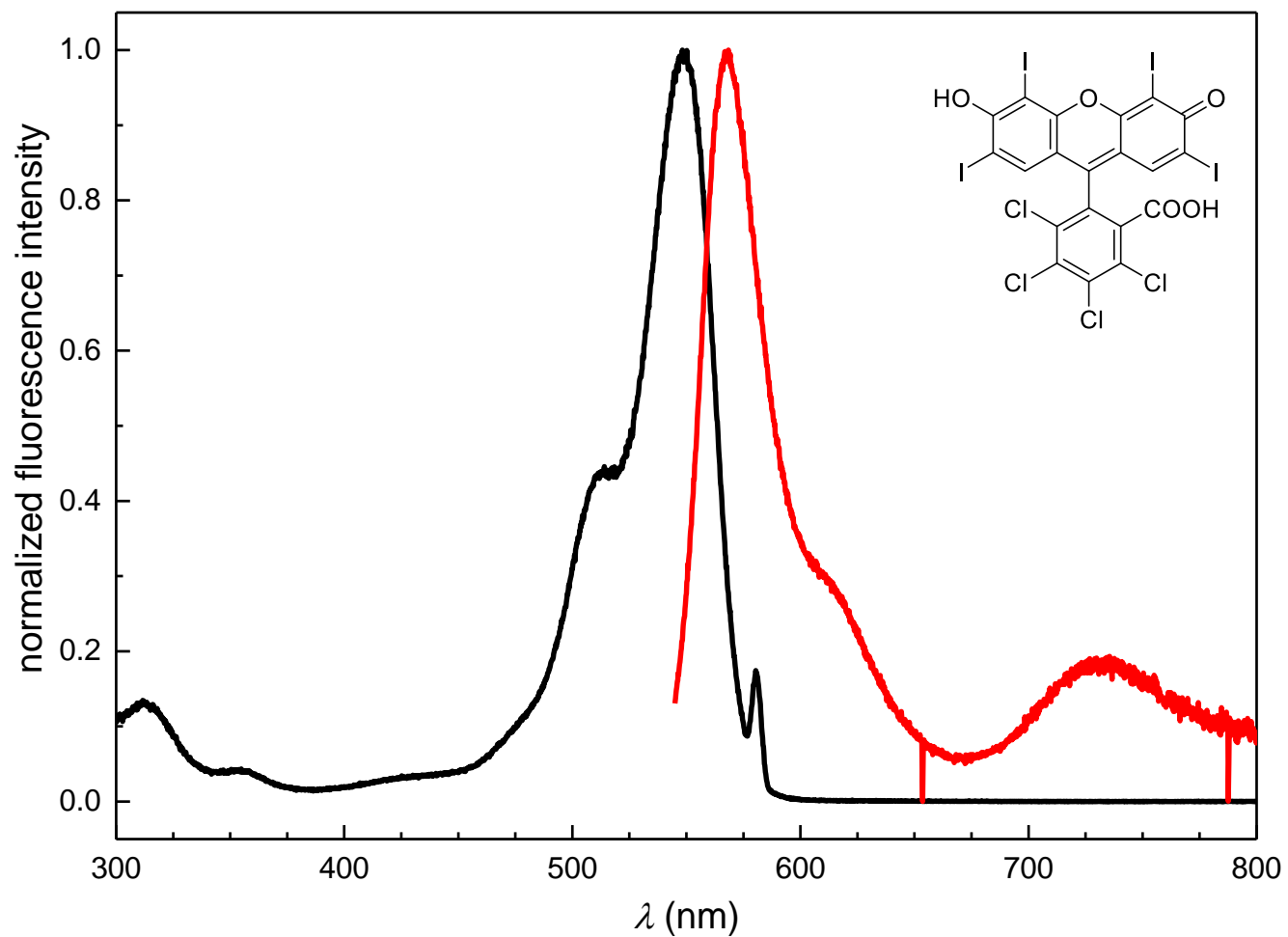


**Figure S27.** A portion of the IR spectrum of standard CO(g); a commercial 10 ppm sample in dry N<sub>2</sub>(g); inset: a full spectrum (arrow, as a visual guide, points at the center of CO signal, at ~2143 cm<sup>-1</sup>).

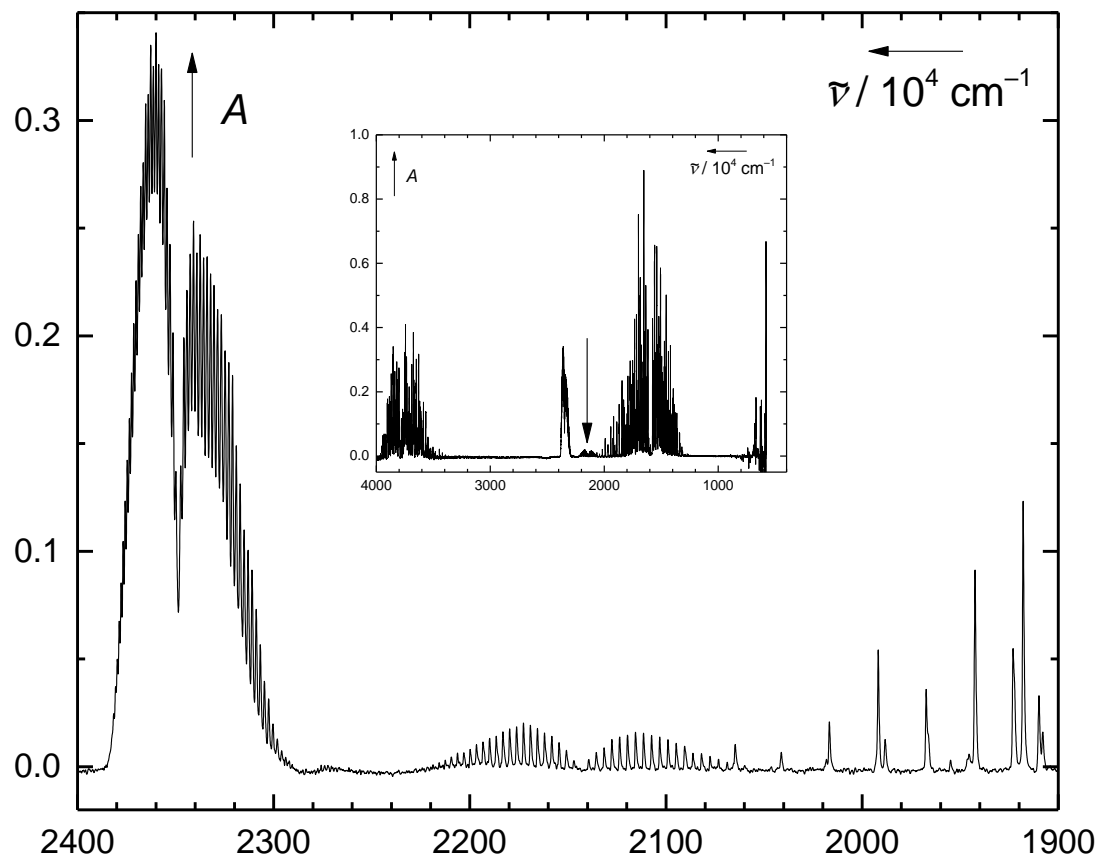


**Figure S28.** A portion of the IR spectrum of gas phase collected after irradiation of fluorescein (**1**,  $c = 2 \times 10^{-5} \text{ mol dm}^{-3}$ ) in aqueous solution (TEAA buffer,  $c(\text{TEAA}) = 0.1 \text{ mol dm}^{-3}$  pH = 7.0,  $I = 0.1 \text{ mol dm}^{-3}$ ) over the reaction mixture obtained after 48 h of irradiation with white-light LED reflectors ( $\lambda_{\text{irr}} = 400\text{--}700 \text{ nm}$ ,  $3 \times 100 \text{ W}$  reflector, Figure S83); inset: a full spectrum (arrow, as a visual guide, points at the center of CO signal, at  $\sim 2143 \text{ cm}^{-1}$ ).

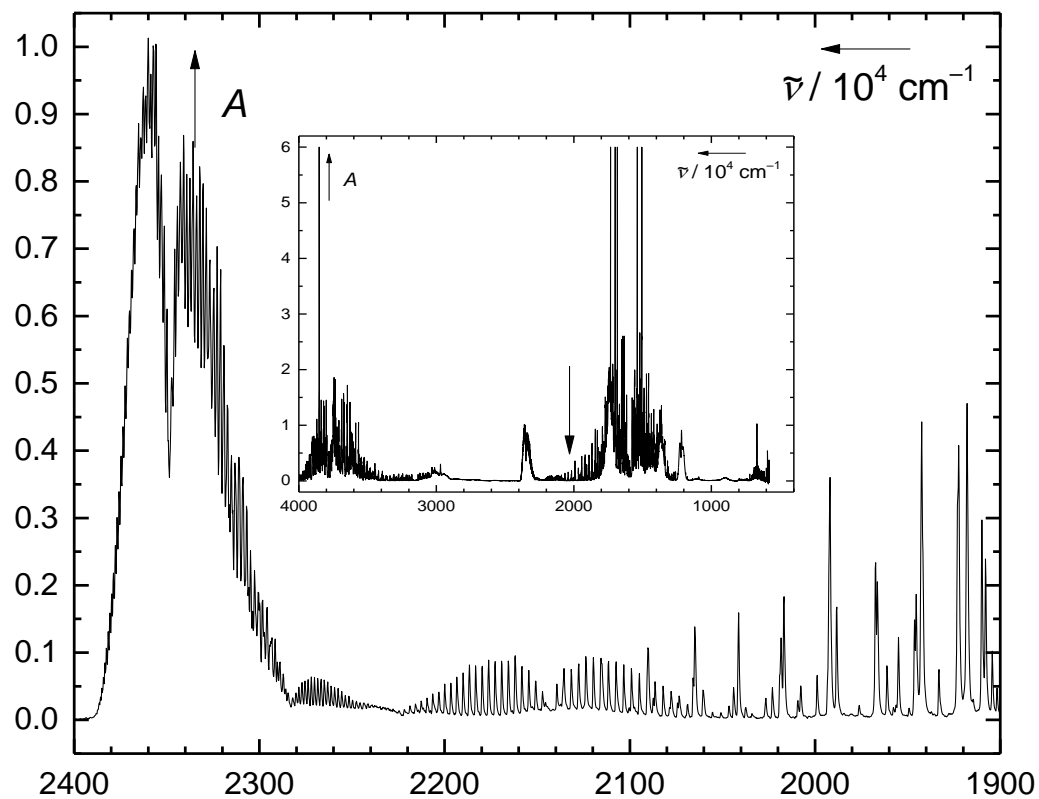


**Figure S29.** A portion of the IR spectrum of gas phase collected after irradiation of eosin Y (**2**,  $c = 2 \times 10^{-5} \text{ mol dm}^{-3}$ ) in aqueous solution (TEAA buffer,  $c(\text{TEAA}) = 0.1 \text{ mol dm}^{-3}$  pH = 7.0,  $I = 0.1 \text{ mol dm}^{-3}$ ) over the reaction mixture obtained after 48 h of irradiation with white-light LED reflectors ( $\lambda_{\text{irr}} = 400\text{--}700 \text{ nm}$ ,  $3 \times 100 \text{ W}$  reflector, Figure S83); inset: a full spectrum (arrow, as a visual guide, points at the center of CO signal, at  $\sim 2143 \text{ cm}^{-1}$ ).

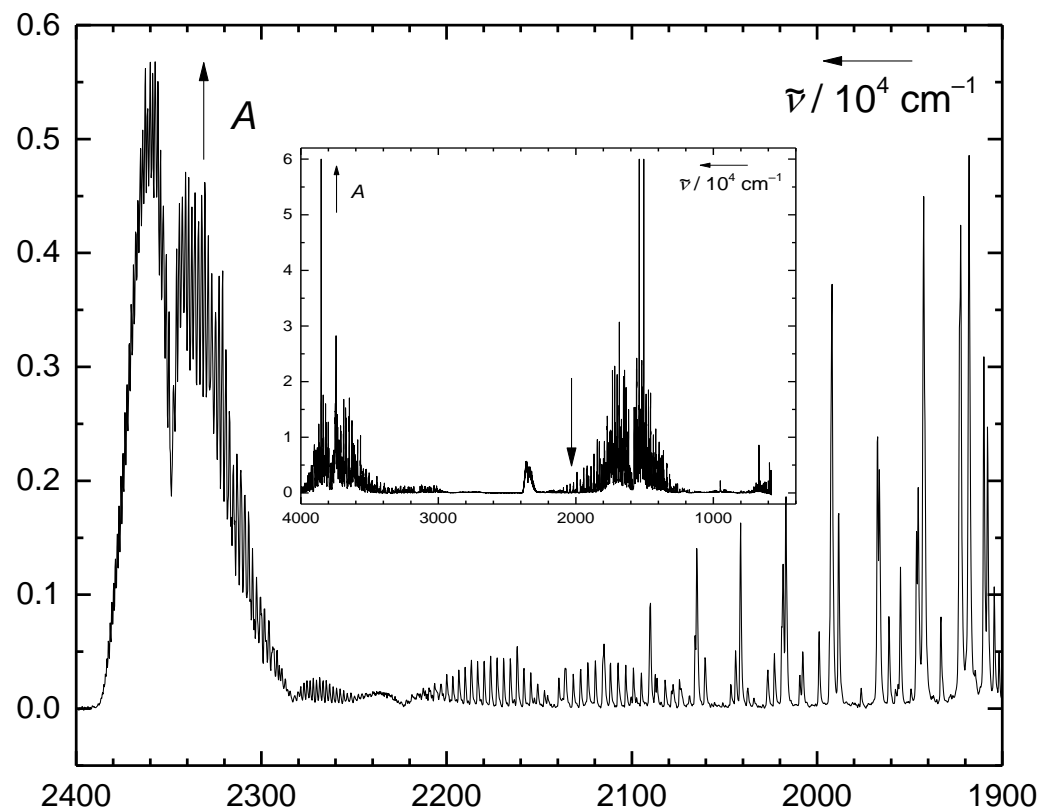


**Figure S30.** IR spectrum of headspace collected above the reaction mixture after 48 h irradiation of **3** ( $c = 2 \times 10^{-5} \text{ mol dm}^{-3}$ ) in an aerated aqueous solution (TEAA buffer,  $c(\text{TEAA}) = 0.1 \text{ mol dm}^{-3}$ ,  $\text{pH} = 7.0$ ,  $I = 0.1 \text{ mol dm}^{-3}$ ;  $\lambda_{\text{irr}} = 400\text{--}700 \text{ nm}$ ; Figure S83). Inset: the full spectrum (arrow, as a visual guide, points at the center of the CO signal at  $\sim 2143 \text{ cm}^{-1}$ ).

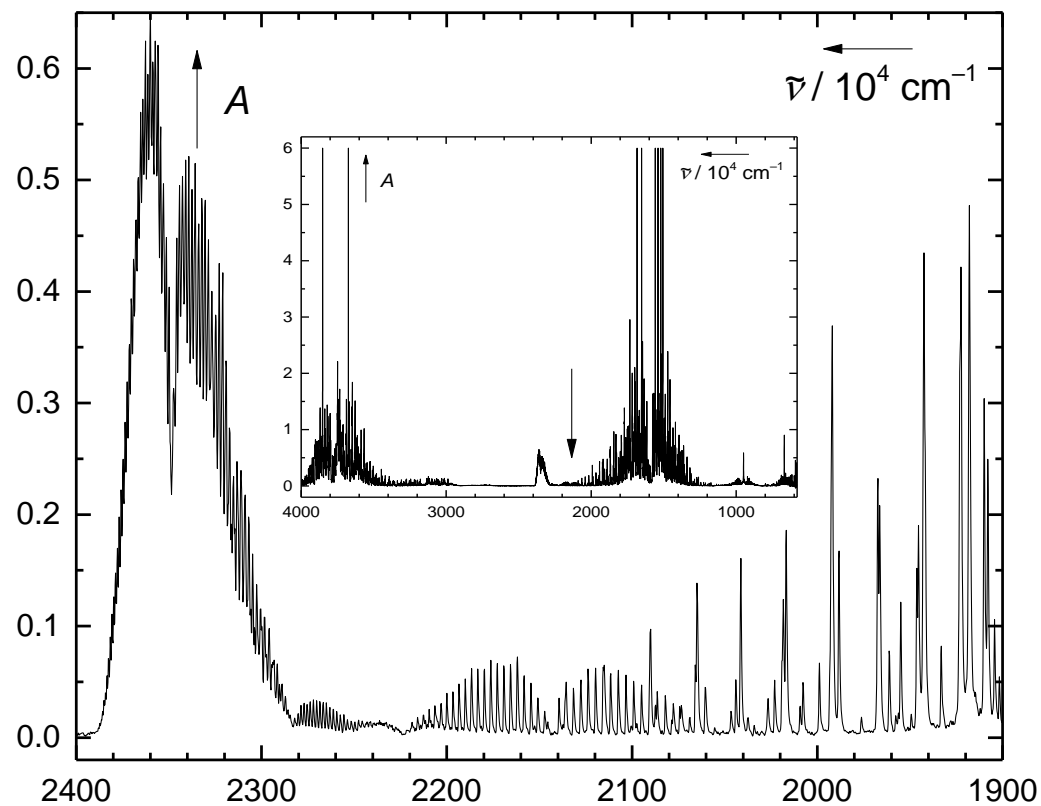


**Figure S31.** Fitted calibration line based on integrated TIC signals (y-axis) from MS analyses of released CO from known photoCORM<sup>1,39</sup> at various concentrations (x-axis).

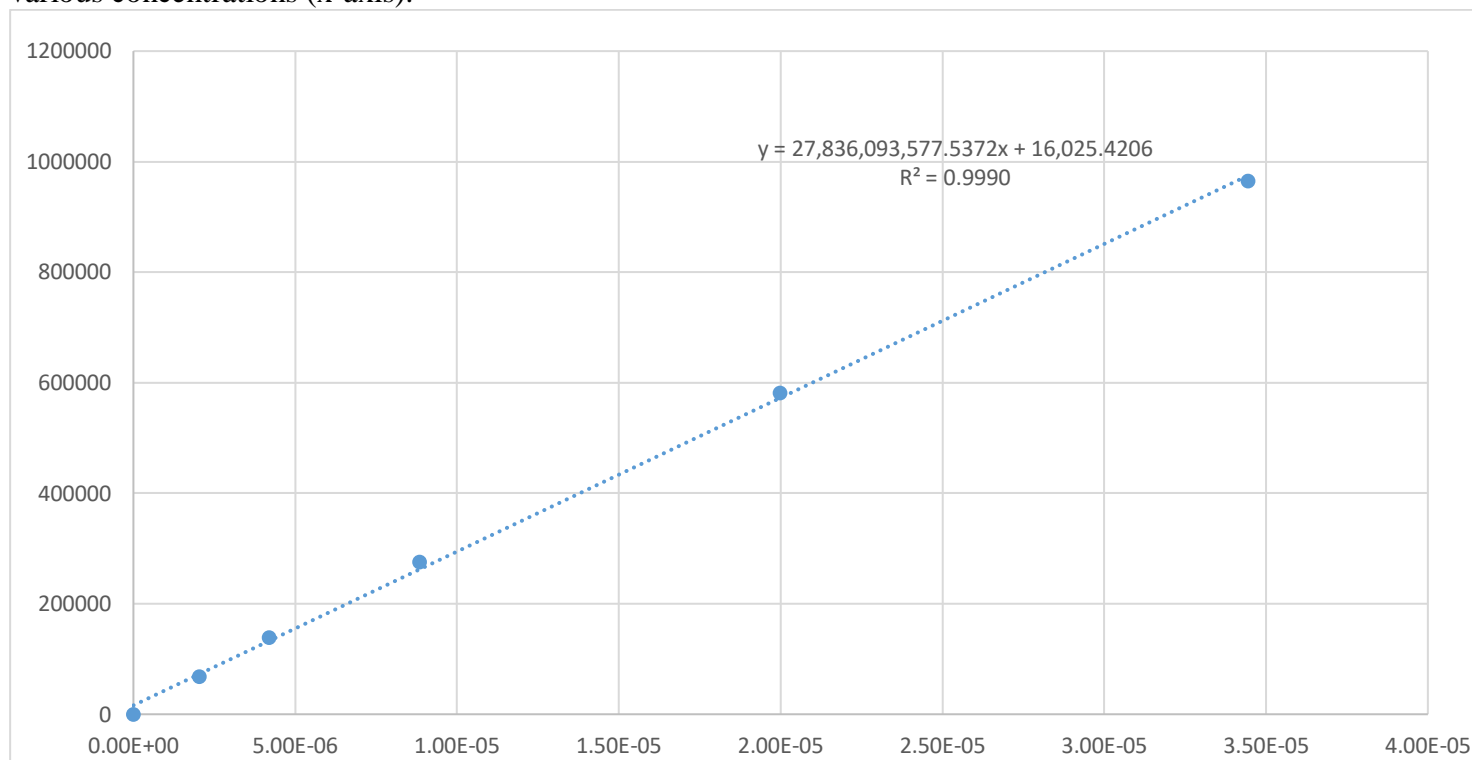


**Figure S32.**  $^1\text{H}$  NMR (500 MHz,  $\text{D}_2\text{O}$ -based PBS buffer ( $0.1 \text{ mol dm}^{-3}$ ,  $\text{pH} = 7.4$ ,  $V = 0.5 \text{ mL}$ )): Product mixture obtained upon irradiation of fluorescein (**1**) with white-light LED reflectors (Figure S83).

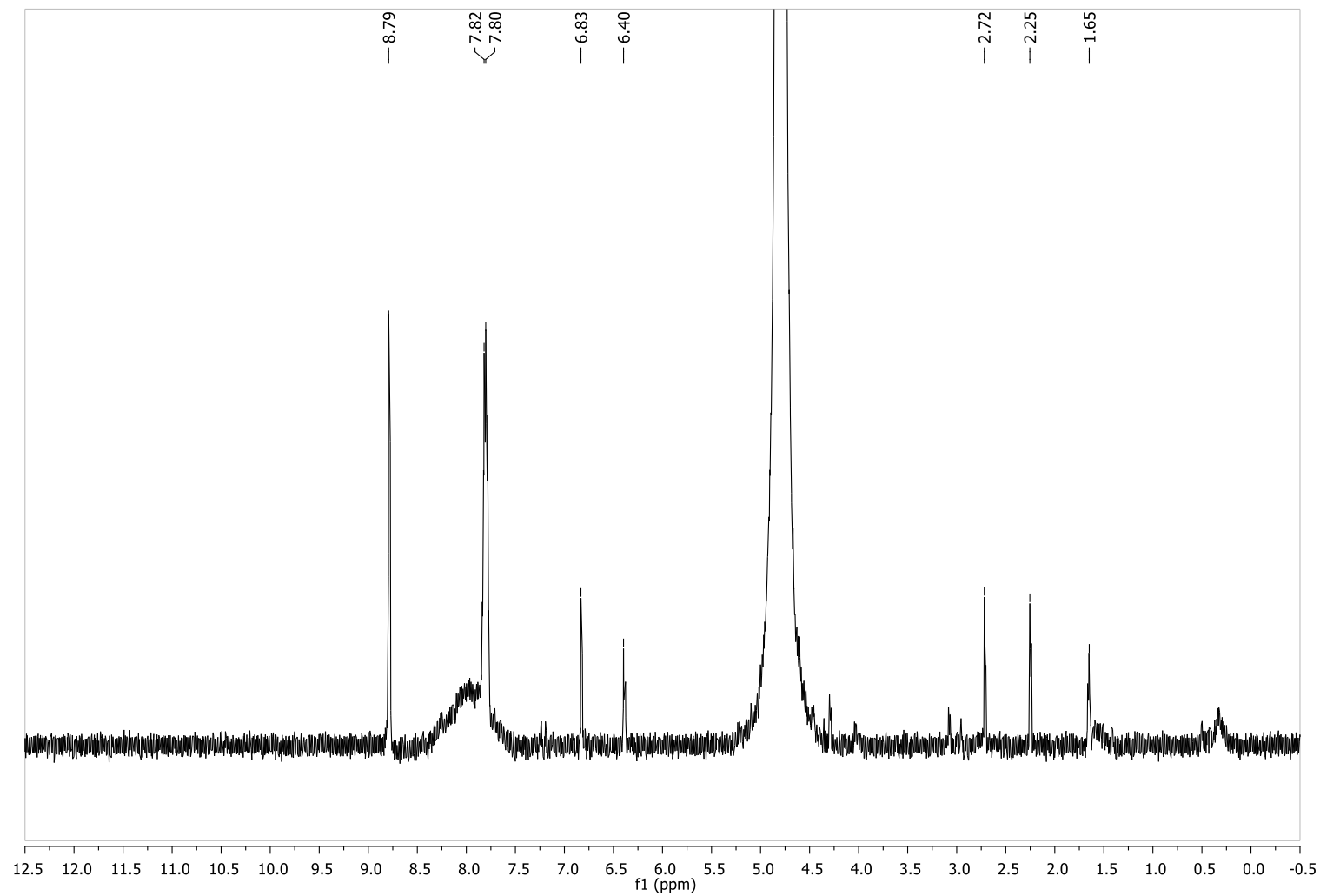


**Figure S33.**  $^1\text{H}$  NMR (500 MHz,  $\text{D}_2\text{O}$ -based PBS buffer ( $0.1 \text{ mol dm}^{-3}$ ,  $\text{pH} = 7.4$ ,  $V = 0.5 \text{ mL}$ )): Product mixture obtained upon irradiation of [9- $^{13}\text{C}$ ][carboxy- $^{13}\text{C}$ ]-fluorescein ( $[^{13}\text{C}_2]\text{-1}$ ) with white-light LED reflectors (Figure S83).

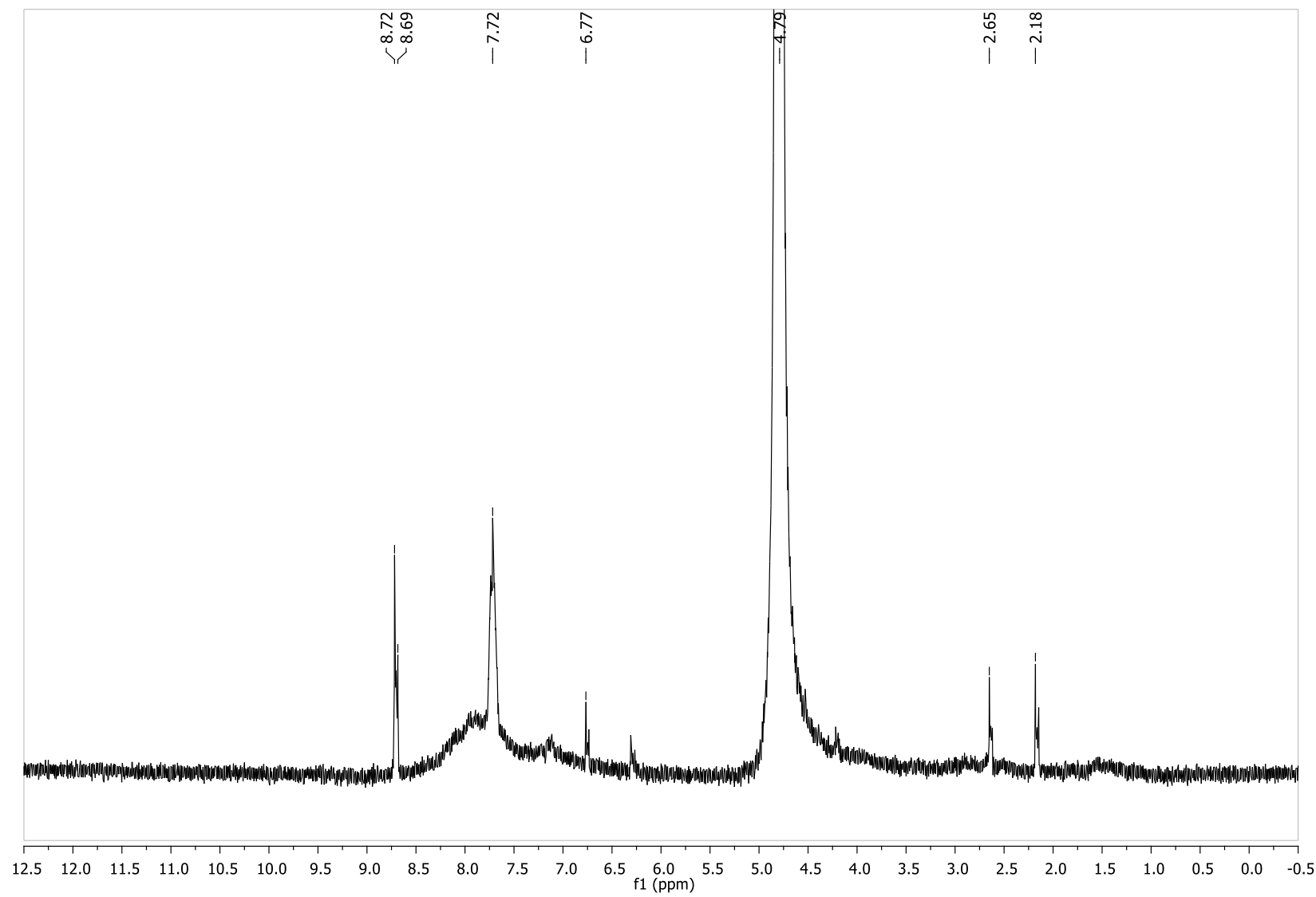


**Figure S34**  $^{13}\text{C}\{^1\text{H}\}$  NMR (125 MHz,  $\text{D}_2\text{O}$ -based PBS buffer ( $0.1 \text{ mol dm}^{-3}$ ,  $\text{pH} = 7.4$ ,  $V = 0.5 \text{ mL}$ ) with  $\text{DMSO-}d_6$  as a co-solvent): Product mixture obtained upon irradiation of  $[9\text{-}^{13}\text{C}][\text{carboxy-}^{13}\text{C}]\text{-fluorescein}$  ( $[^{13}\text{C}_2]\text{-1}$ ) with white-light LED reflectors (Figure S83).

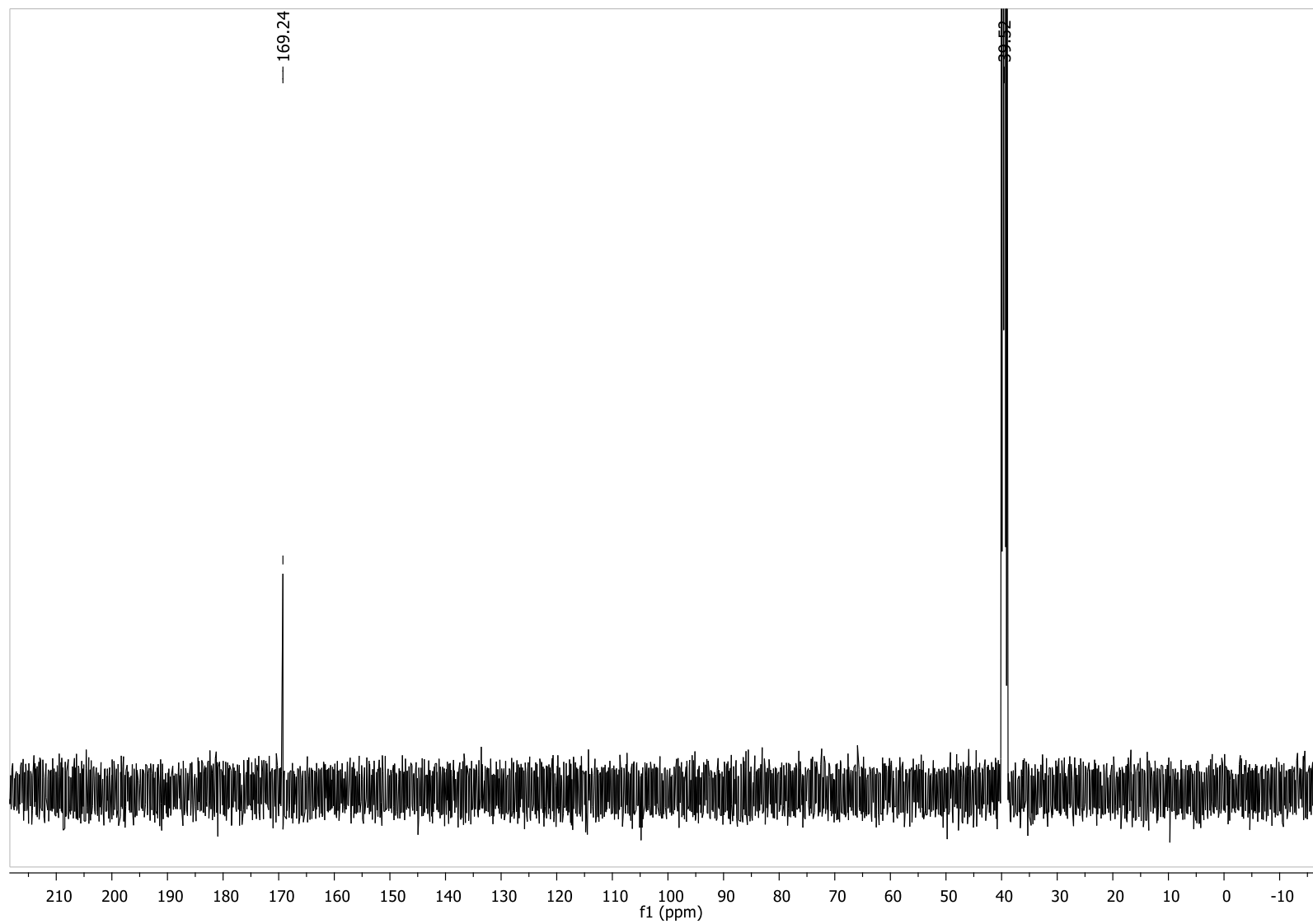


**Figure S35.**  $^1\text{H}$  NMR (500 MHz,  $\text{CD}_3\text{OD}$ ): Product mixture obtained upon irradiation of fluorescein (**1**) with white-light LED reflectors (Figure S83).

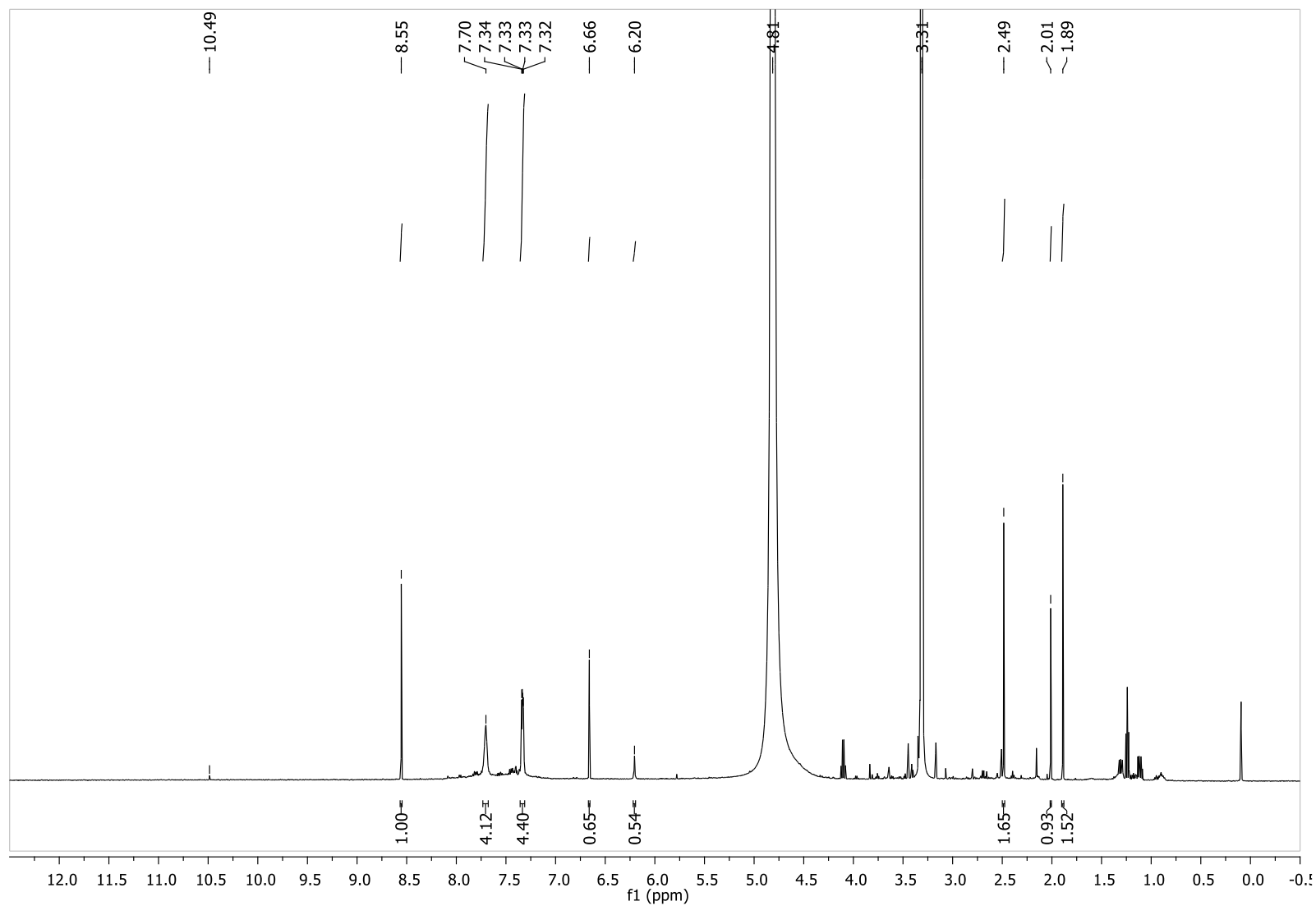


**Figure S36.**  $^1\text{H}$  NMR (500 MHz,  $\text{CD}_3\text{OD}$ ): Product mixture obtained upon irradiation of  $[9\text{-}^{13}\text{C}][\text{carboxy-}^{13}\text{C}]\text{-fluorescein}$  ( $[^{13}\text{C}_2]\text{-1}$ ) with white-light LED reflectors (Figure S83).

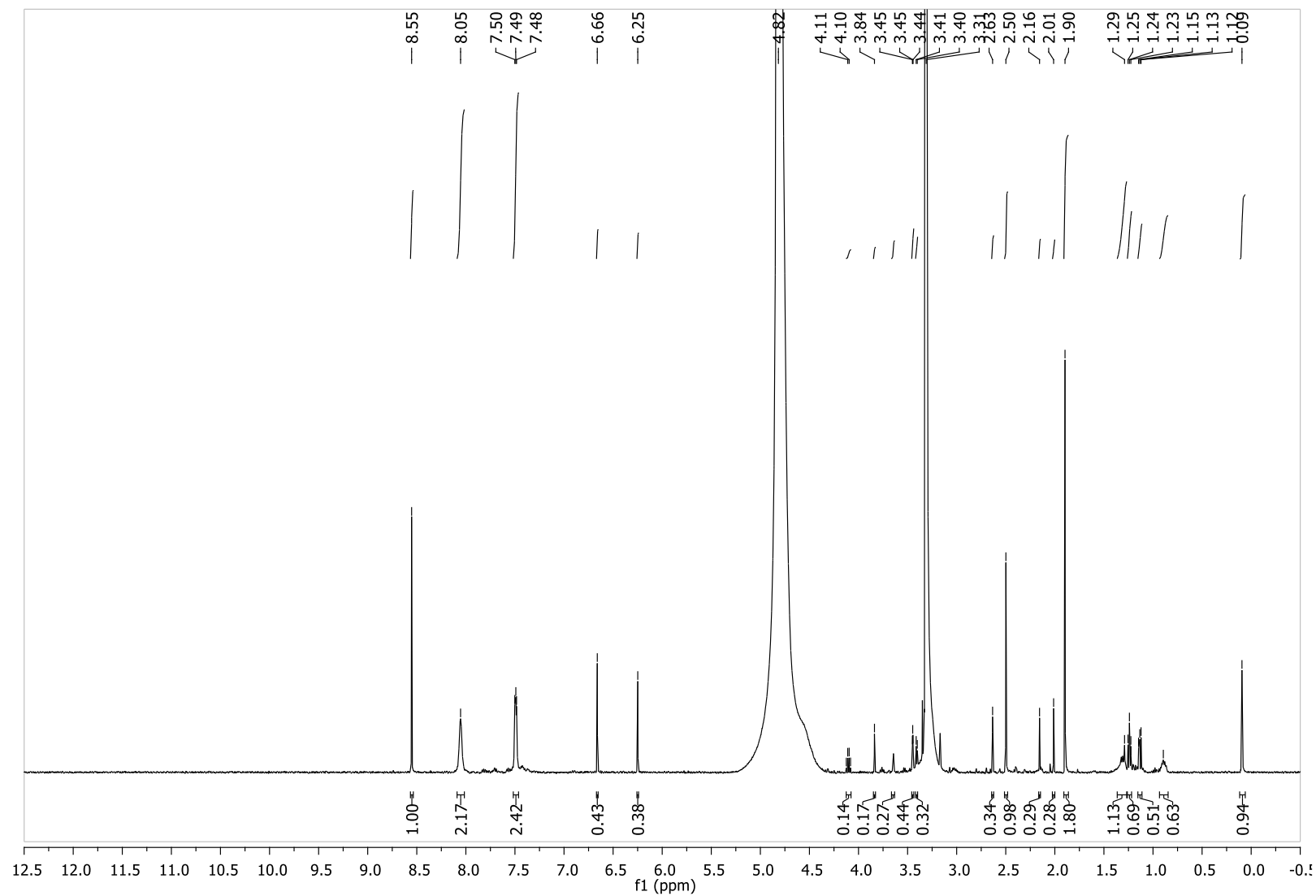


**Figure S37.**  $^{13}\text{C}\{^1\text{H}\}$  NMR (125 MHz,  $\text{CD}_3\text{OD}$ ): Product mixture obtained upon irradiation of  $[9\text{-}^{13}\text{C}][\text{carboxy-}^{13}\text{C}]\text{-fluorescein}$  ( $[^{13}\text{C}_2]\text{-1}$ ) with white-light LED reflectors (Figure S83).

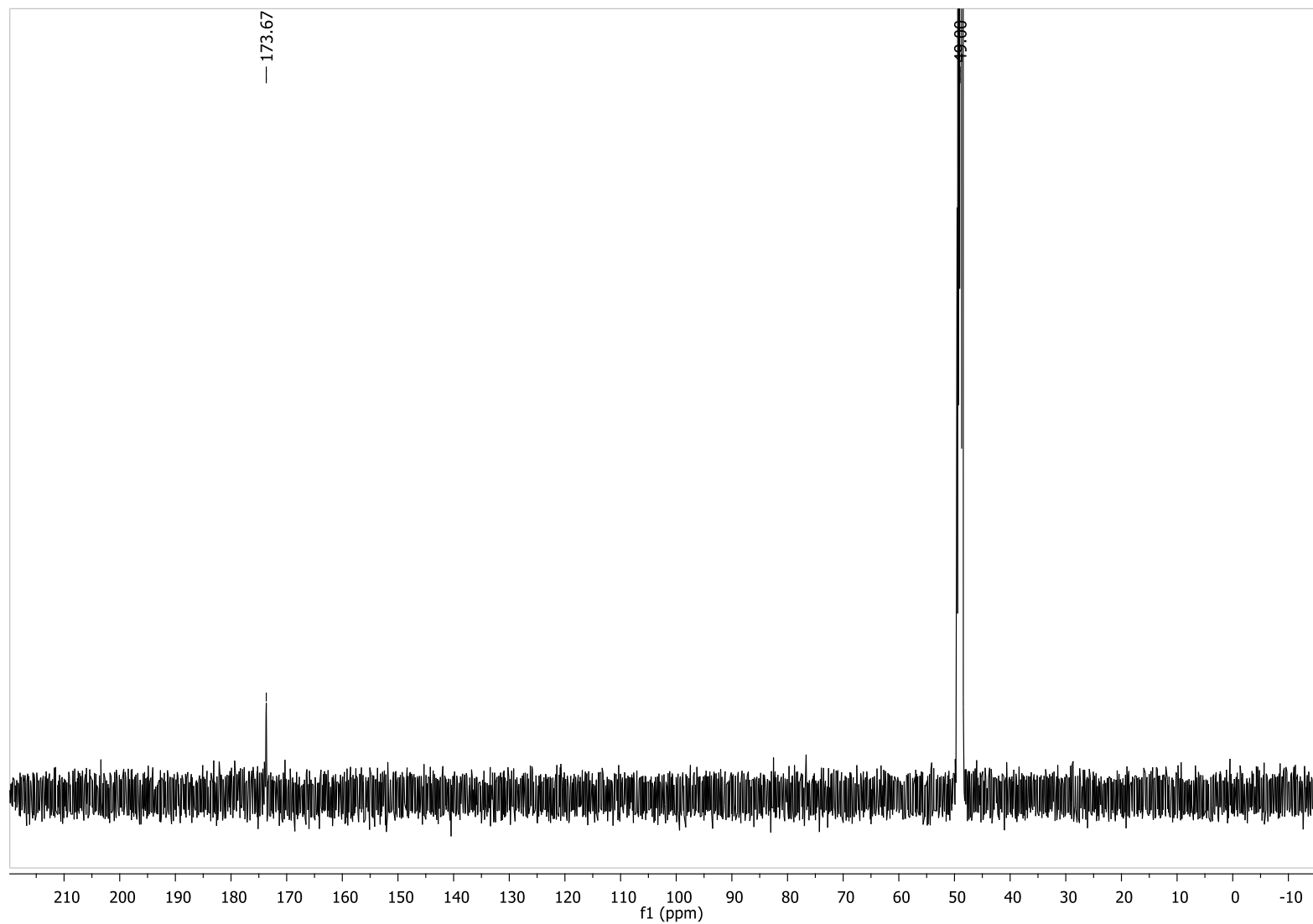


**Figure S38.**  $^1\text{H}$ - $^{13}\text{C}$  HSQC NMR (500 MHz,  $\text{CD}_3\text{OD}$ ): Product mixture obtained upon irradiation of  $[9\text{-}^{13}\text{C}][\text{carboxy-}^{13}\text{C}]\text{-fluorescein}$  ( $[^{13}\text{C}_2]\text{-1}$ ) with white-light LED reflectors (Figure S83).

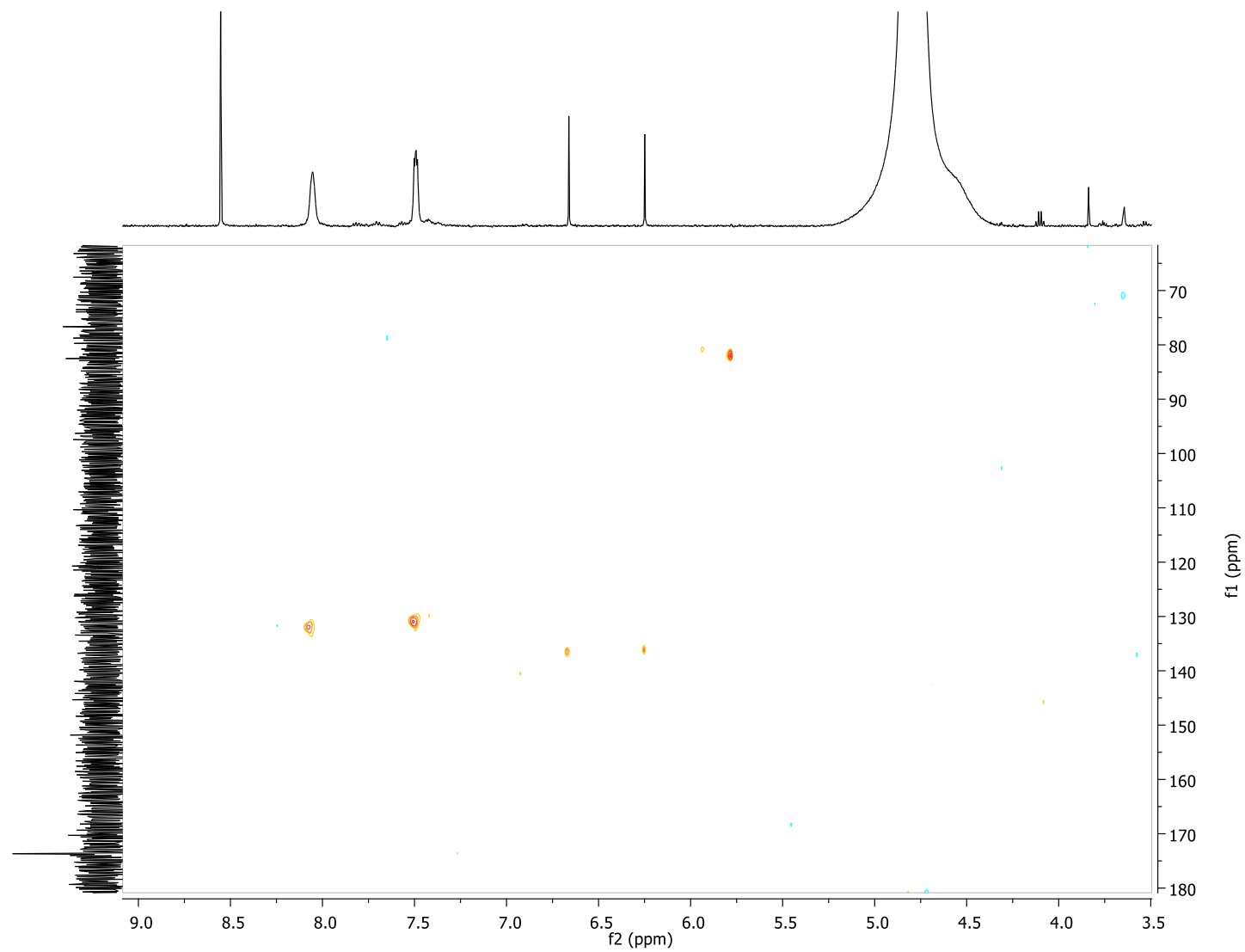


**Figure S39.**  $^1\text{H}$  NMR (500 MHz,  $\text{D}_2\text{O}$ -based PBS buffer (0.1 mol  $\text{dm}^{-3}$ , pH = 7.4) spectra of an aerated solution of **1** ( $c \sim 6 \times 10^{-3}$  mol  $\text{dm}^{-3}$ ;  $V = 0.5$  mL) during irradiation with a  $3 \times 100$  W white LED (Figure S83). Note: the signal at  $\delta$  0.0 ppm corresponds to 1 % (v/v) TMS in  $\text{CCl}_4$  used as internal standard (in a sealed glass capillary).

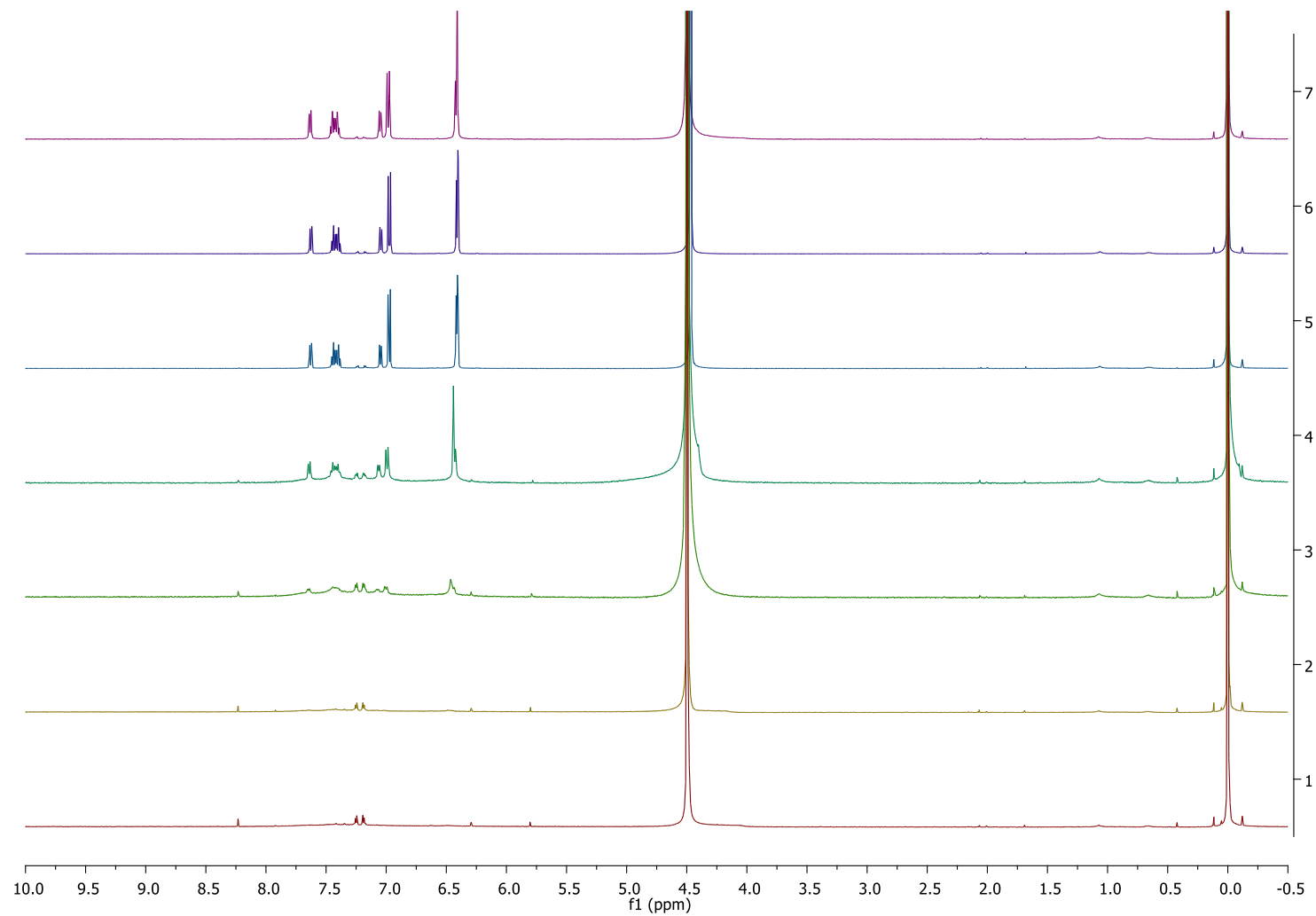


**Figure S40.**  $^1\text{H}$  NMR (500 MHz,  $\text{D}_2\text{O}$ -based PBS buffer (0.1 mol  $\text{dm}^{-3}$ , pH = 7.4) spectra of an a) aerated solution of **1** ( $c \sim 6 \times 10^{-3}$  mol  $\text{dm}^{-3}$ ;  $V = 0.5$  mL) exhaustively irradiated with a  $3 \times 100$  W white LED (Figure S83) until no starting material was detected (upper panel), and b) with added authentic samples of phthalic and formic acids (bottom panel). Note: the signal at  $\delta$  0.0 ppm corresponds to 1 % (v/v) TMS in  $\text{CCl}_4$  used as internal standard (in a sealed glass capillary).

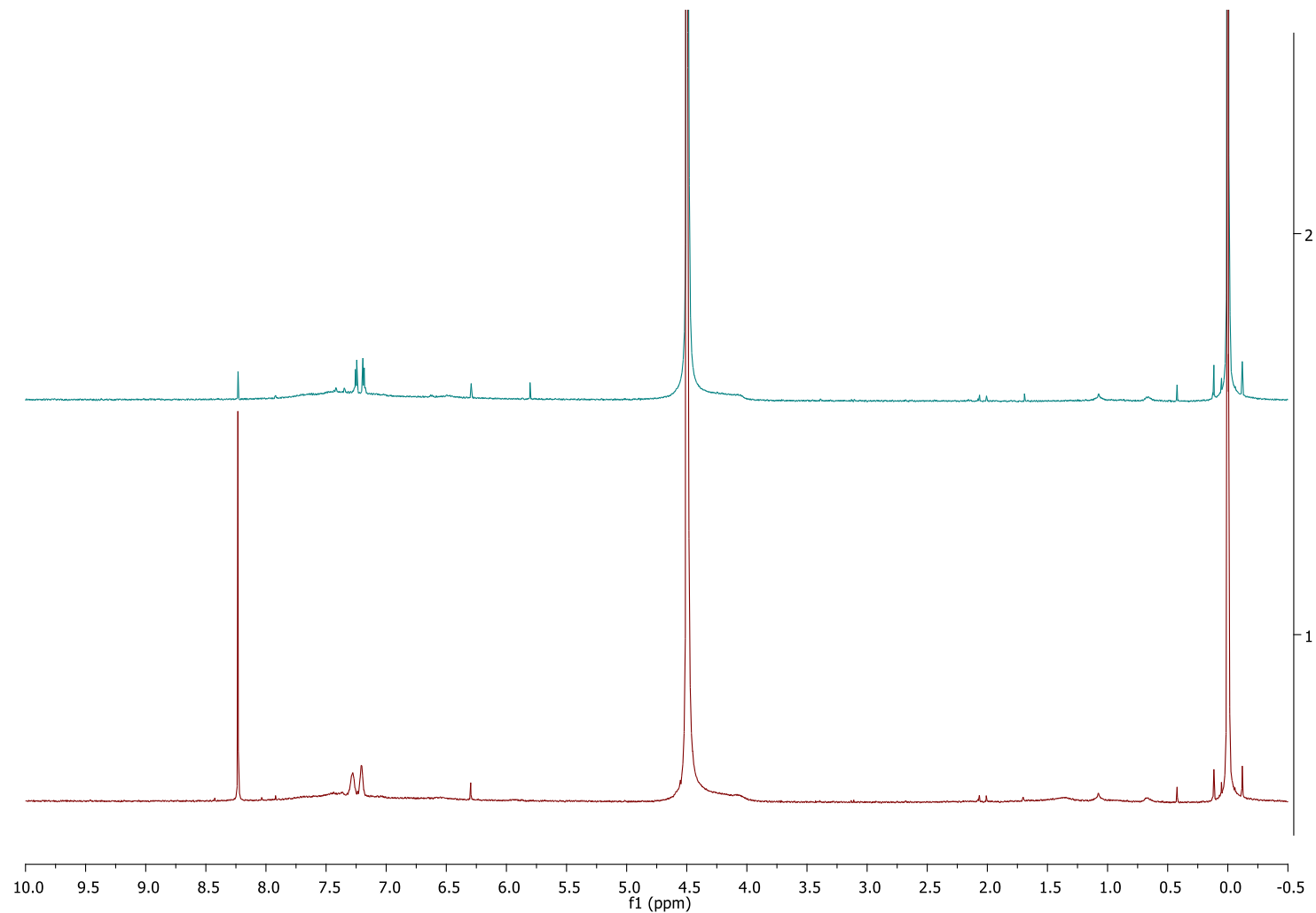


**Figure S41.**  $^1\text{H}$  NMR (500 MHz,  $\text{D}_2\text{O}$ -based PBS buffer ( $0.1 \text{ mol dm}^{-3}$ ,  $\text{pH} = 7.4$ ) spectra of an aerated solution of  $^{13}\text{C}_2\text{-1}$  ( $c \sim 6 \times 10^{-3} \text{ mol dm}^{-3}$ ;  $V = 0.5 \text{ mL}$ ) before (top panel) and after (3 days, bottom panel) irradiation with a  $3 \times 100 \text{ W}$  white LED (Figure S83). Note: the signal at  $\delta 0.0 \text{ ppm}$  corresponds to 1 % (v/v) TMS in  $\text{CCl}_4$  used as internal standard (in a sealed glass capillary).

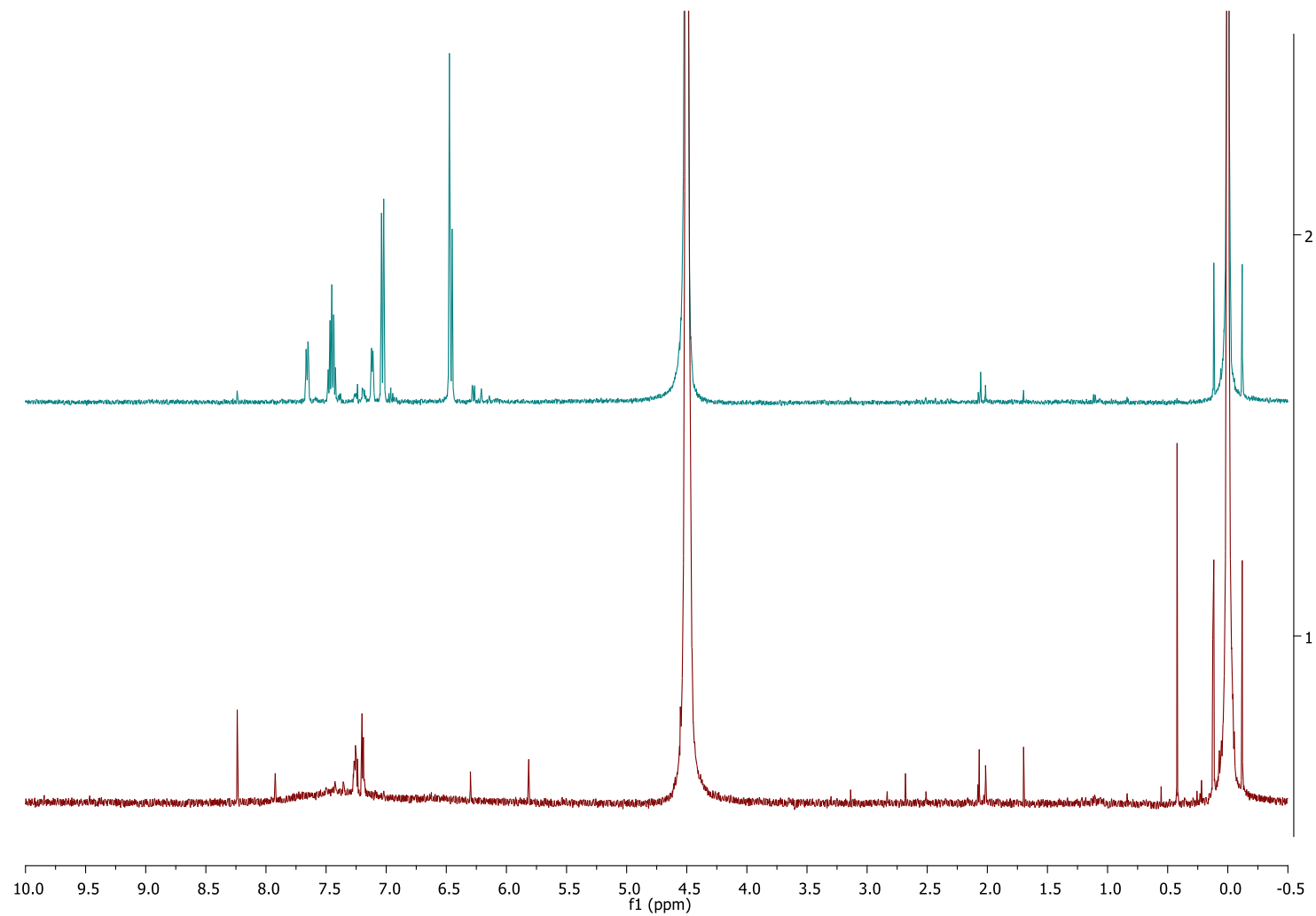


**Figure S42.**  $^{13}\text{C}\{^1\text{H}\}$  NMR (500 MHz,  $\text{D}_2\text{O}$ -based PBS buffer ( $0.1 \text{ mol dm}^{-3}$ ,  $\text{pH} = 7.4$ ) spectra of an a) aerated solution of  $^{13}\text{C}_2\text{-1}$  ( $c \sim 6 \times 10^{-3} \text{ mol dm}^{-3}$ ;  $V = 0.5 \text{ mL}$ ) exhaustively irradiated with a  $3 \times 100 \text{ W}$  white LED (Figure S83) until no starting material was detected.

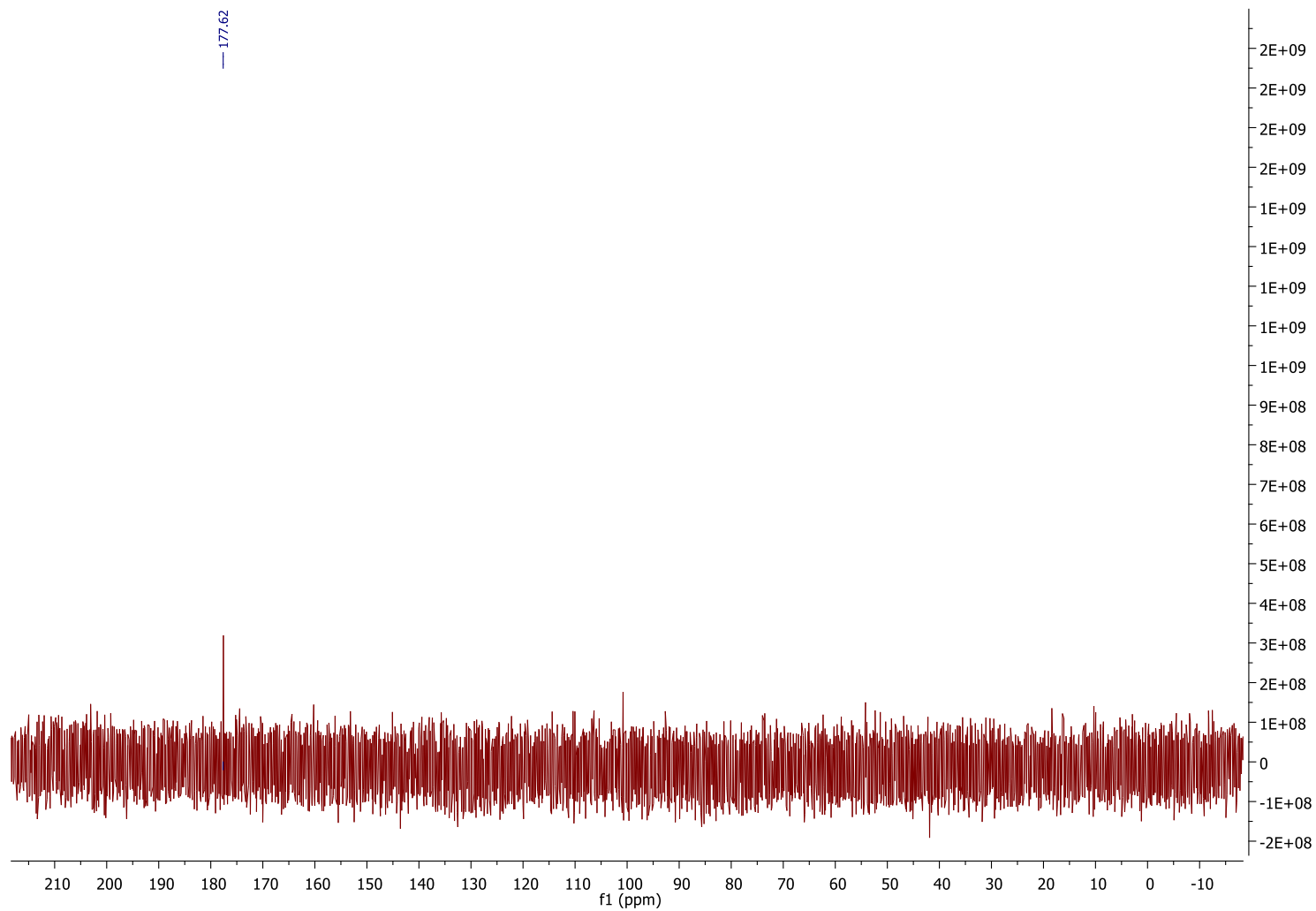


**Figure S43.**  $^1\text{H}$  NMR (500 MHz,  $\text{D}_2\text{O}$ -based PBS buffer (0.1 mol  $\text{dm}^{-3}$ , pH = 7.4) spectra of an aerated solution of **2** ( $c \sim 6 \times 10^{-3}$  mol  $\text{dm}^{-3}$ ;  $V = 0.5$  mL) during irradiation with a  $3 \times 100$  W white LED (Figure S83). Note: the signal at  $\delta$  0.0 ppm corresponds to 1 % (v/v) TMS in  $\text{CCl}_4$  used as internal standard (in a sealed glass capillary.)

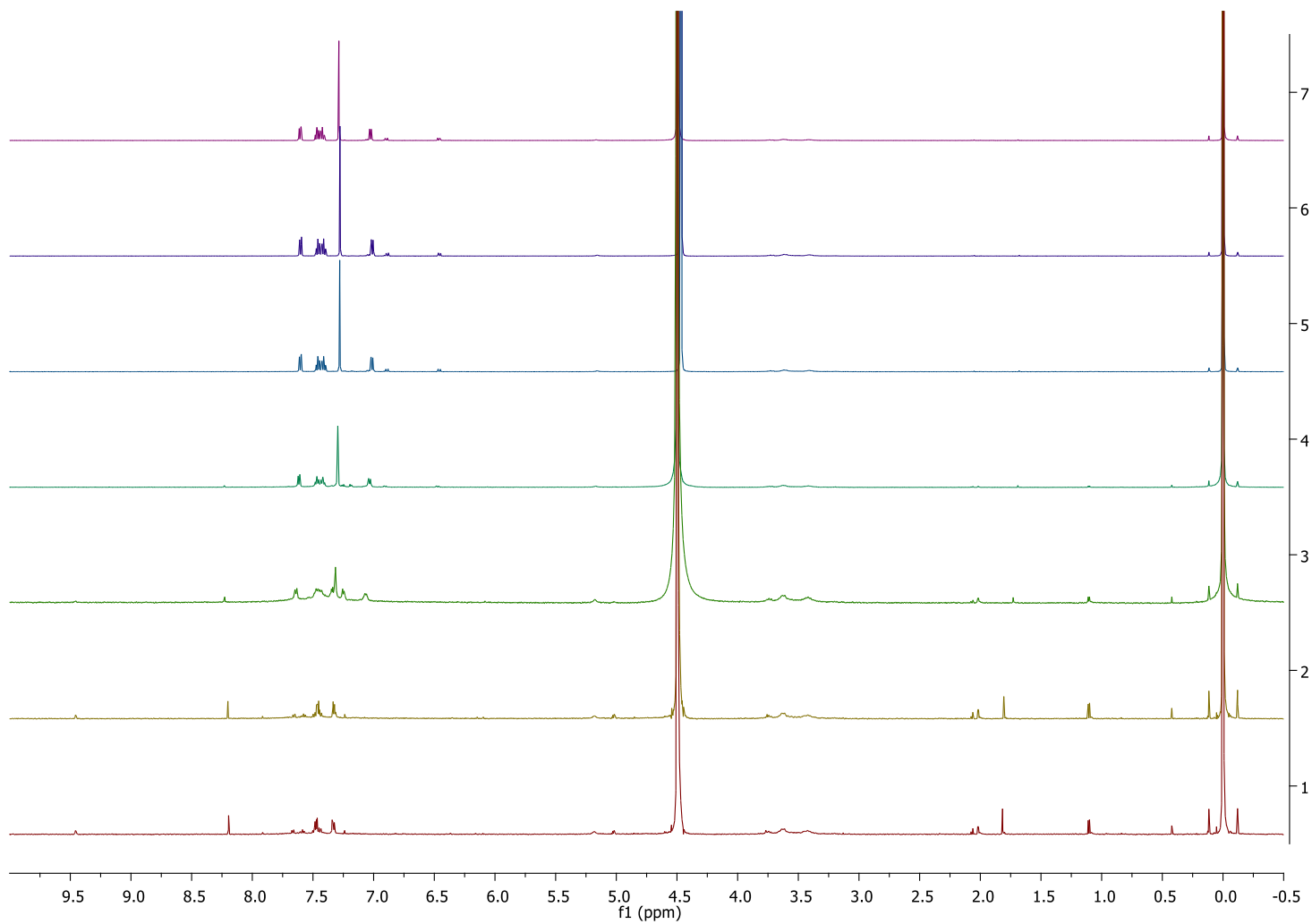


**Figure S44.**  $^1\text{H}$  NMR (500 MHz,  $\text{D}_2\text{O}$ -based PBS buffer (0.1 mol  $\text{dm}^{-3}$ , pH = 7.4) spectra of an a) aerated solution of **2** ( $c \sim 6 \times 10^{-3}$  mol  $\text{dm}^{-3}$ ;  $V = 0.5$  mL) exhaustively irradiated with a  $3 \times 100$  W white LED (Figure S83) until no starting material was detected (upper panel), and b) with added authentic samples of phthalic and formic acids (bottom panel). Note: the signal at  $\delta$  0.0 ppm corresponds to 1 % (v/v) TMS in  $\text{CCl}_4$  used as internal standard (in a sealed glass capillary.)

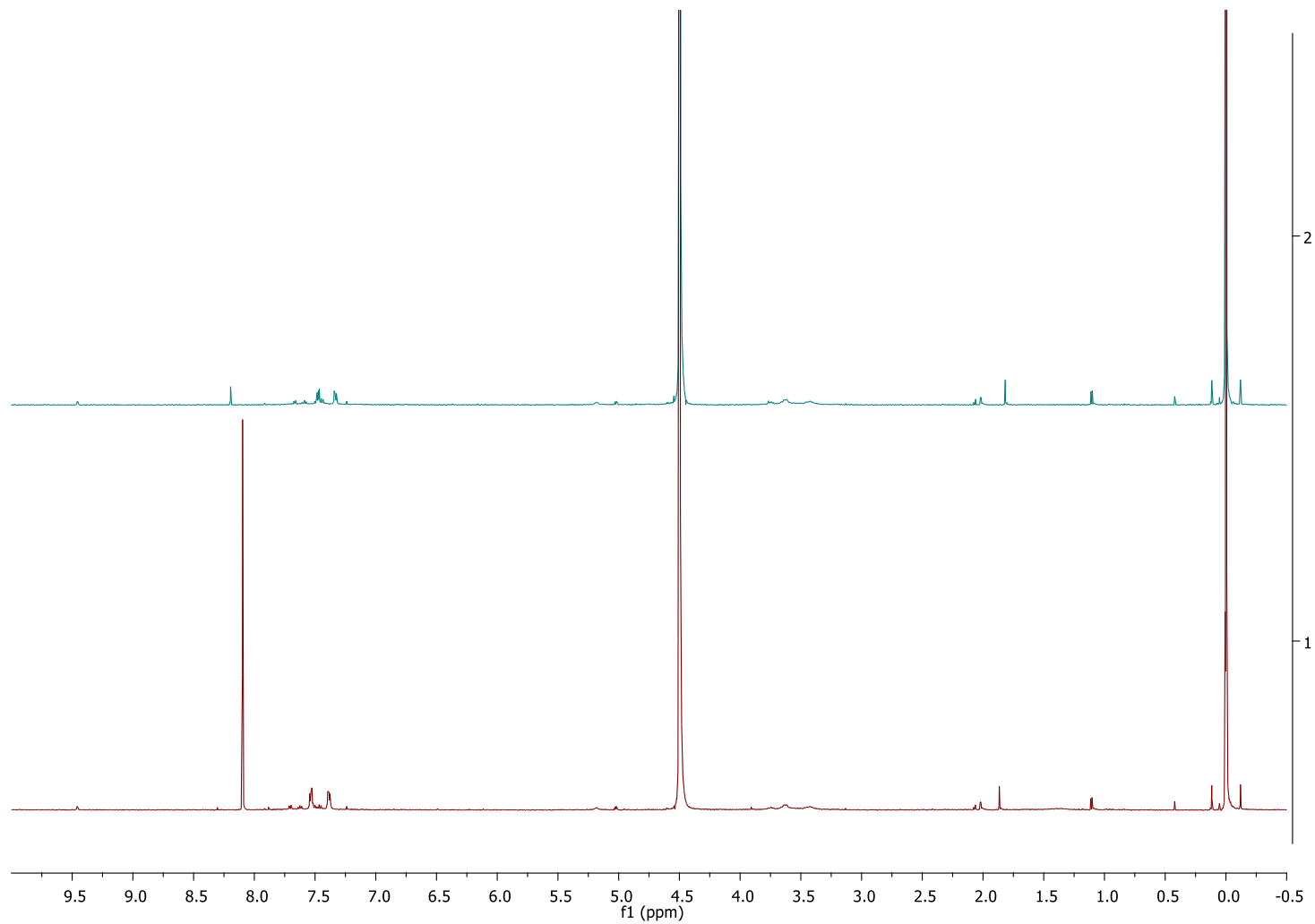


**Figure S45.**  $^1\text{H}$  NMR (500 MHz,  $\text{D}_2\text{O}$ -based PBS buffer ( $0.1 \text{ mol dm}^{-3}$ ,  $\text{pH} = 7.4$ ) spectra of an aerated solution of **3** ( $c \sim 6 \times 10^{-3} \text{ mol dm}^{-3}$ ;  $V = 0.5 \text{ mL}$ ) during irradiation with a  $3 \times 100 \text{ W}$  white LED (Figure S83). Note: the signal at  $\delta 0.0 \text{ ppm}$  corresponds to 1 % (v/v) TMS in  $\text{CCl}_4$  used as internal standard (in a sealed glass capillary).

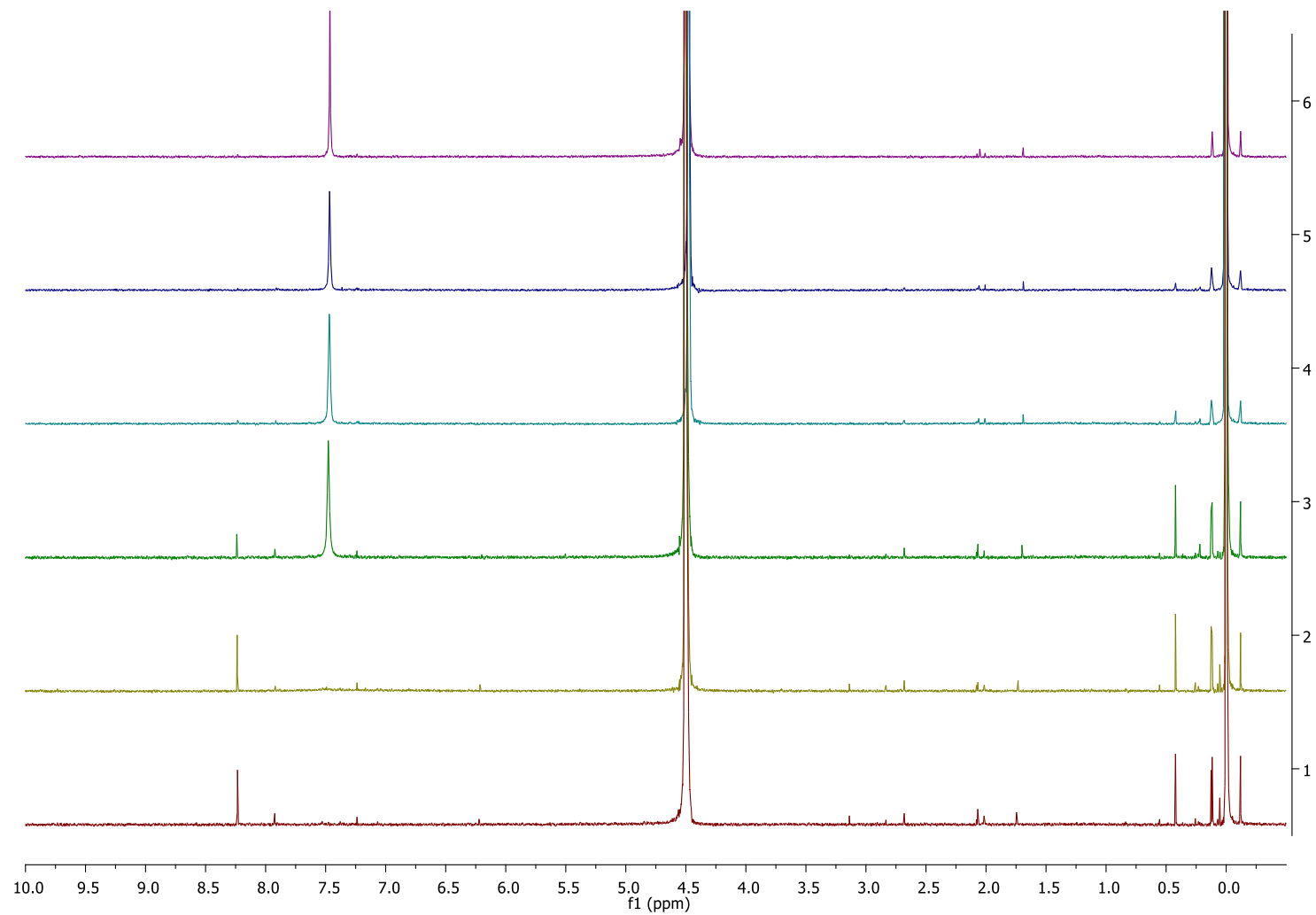


**Figure S46.**  $^1\text{H}$  NMR (500 MHz,  $\text{D}_2\text{O}$ -based PBS buffer ( $0.1 \text{ mol dm}^{-3}$ ,  $\text{pH} = 7.4$ ) spectra of an a) aerated solution of **3** ( $c \sim 6 \times 10^{-3} \text{ mol dm}^{-3}$ ;  $V = 0.5 \text{ mL}$ ) exhaustively irradiated with a  $3 \times 100 \text{ W}$  white LED (Figure S83) until no starting material was detected (upper panel), and b) with added authentic samples of phthalic and formic acids (bottom panel). Note: the signal at  $\delta 0.0 \text{ ppm}$  corresponds to 1 % (v/v) TMS in  $\text{CCl}_4$  used as internal standard (in a sealed glass capillary).

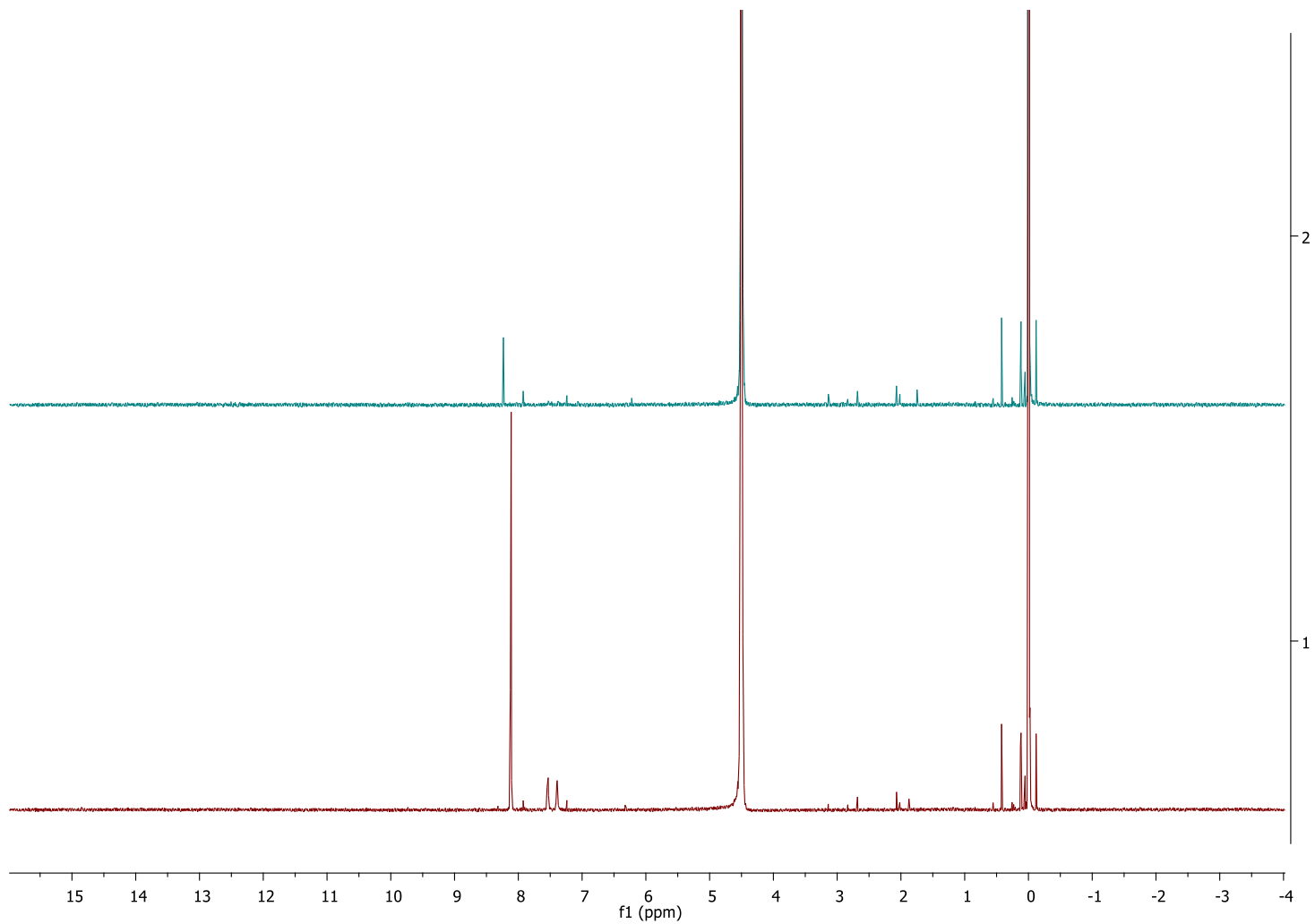


**Figure S47.** Differential thermal scanning calorimetry (DSC, blue line; right y-axis) and thermogravimetric analysis (TG, green line; left y-axis) upon heating from 25 to 500 °C: fluorescein (**1**)

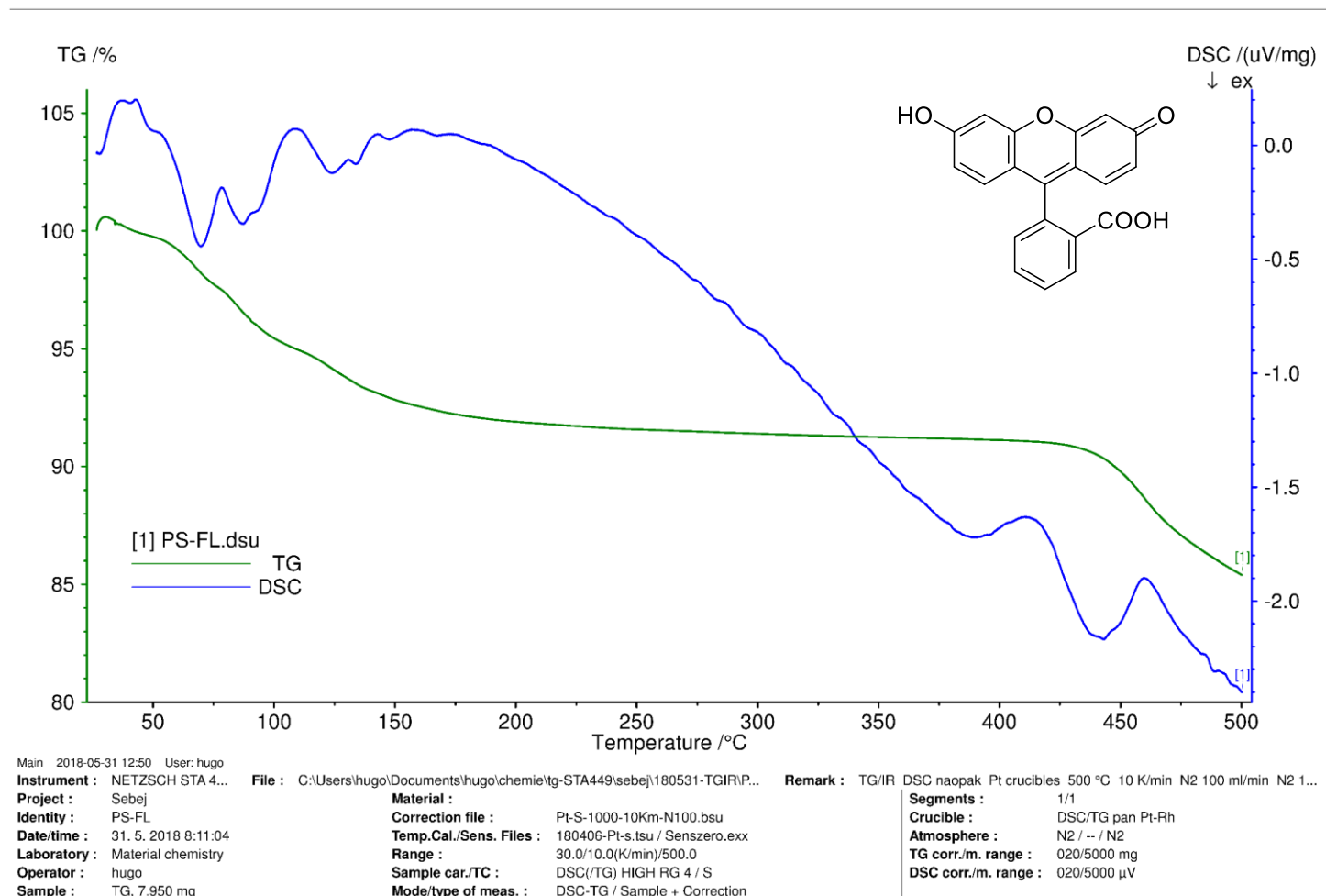


**Figure S48.** Differential thermogravimetric analysis (DTG, green dash-dot line; right y-axis) and thermogravimetric analysis (TG, solid green line; left y-axis) upon heating from 25 to 500 °C; the mass changes for each process and residual mass at 500 °C are indicated: fluorescein (**1**)

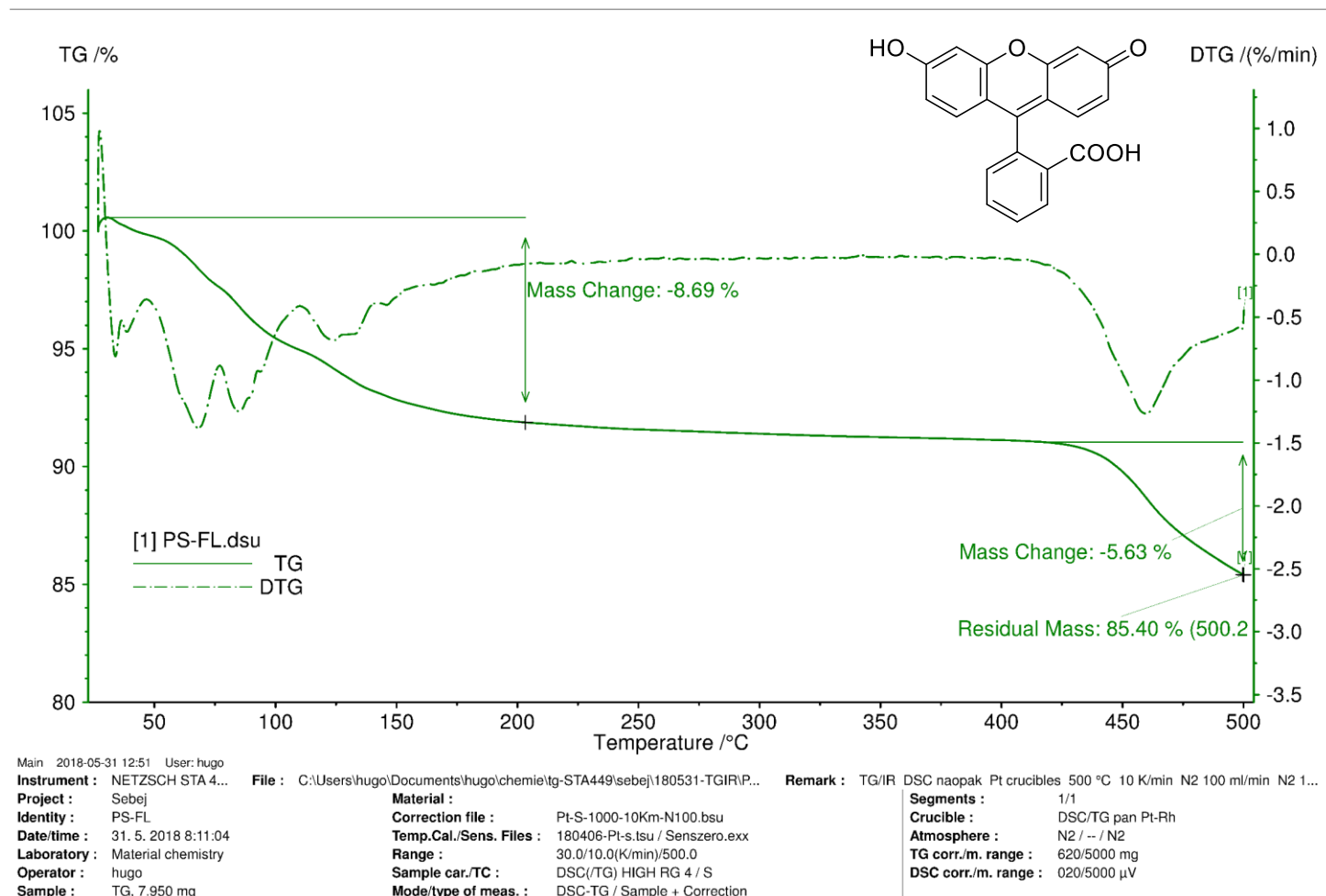


**Figure S49.** Differential thermal scanning calorimetry (DSC, blue line; left y-axis) and differential differential thermal scanning calorimetry (DDSC, blue dash-dot line; right y-axis) upon heating from 25 to 500 °C; the inflection points for each thermal process are indicated: fluorescein (1)

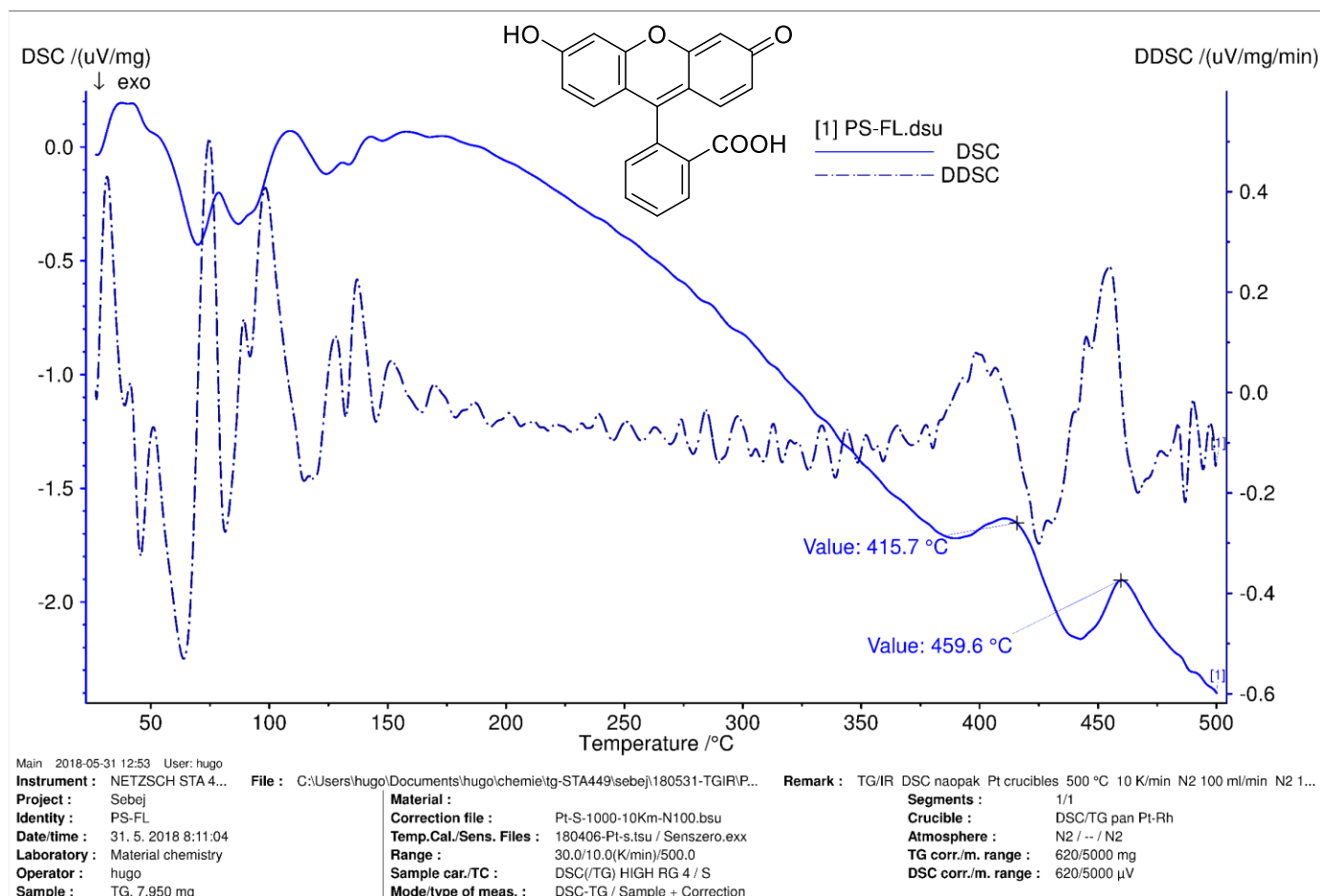
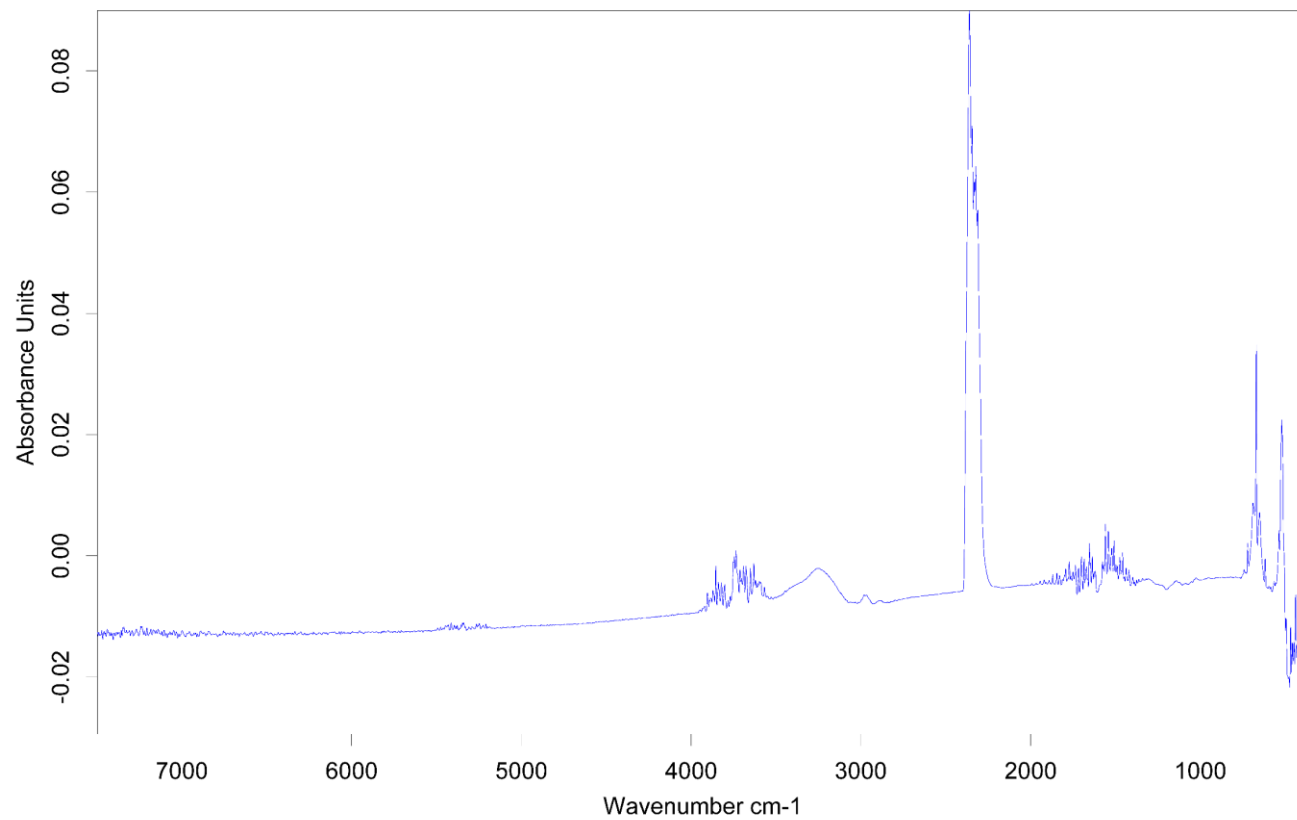


**Figure S50.** IR of the released gases during the thermal scanning calorimetry and thermogravimetric analysis upon heating from 25 to 500 °C: fluorescein (**1**)



PS-FL\_0\_AB\_193\_2721.973000\_Seconds.0

TG

7.950 | NETZSCH STA 449 C | C:\ngbwint\data5\PS-FL.dsu

31. 5. 2018

**Figure S51.** Differential thermal scanning calorimetry (DSC, blue line; right y-axis) and thermogravimetric analysis (TG, green line; left y-axis) upon heating from 25 °C to 500 °C: eosin Y (2)

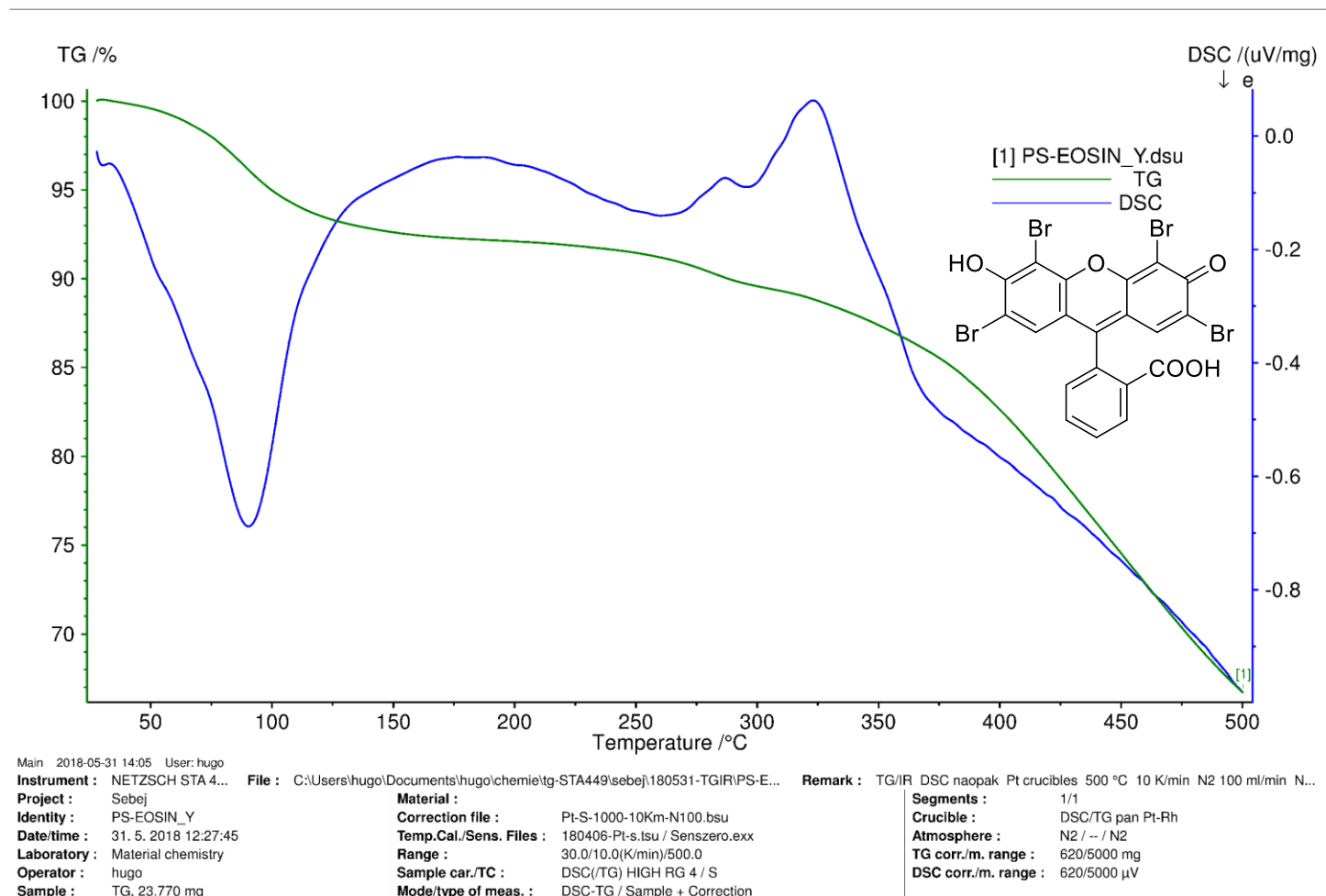


**Figure S52.** Differential thermogravimetric analysis (DTG, green dash-dot line; right y-axis) and thermogravimetric analysis (TG, solid green line; left y-axis) upon heating from 25 to 500 °C; the mass changes for each process and residual mass at 500 °C are indicated: eosin Y (2)

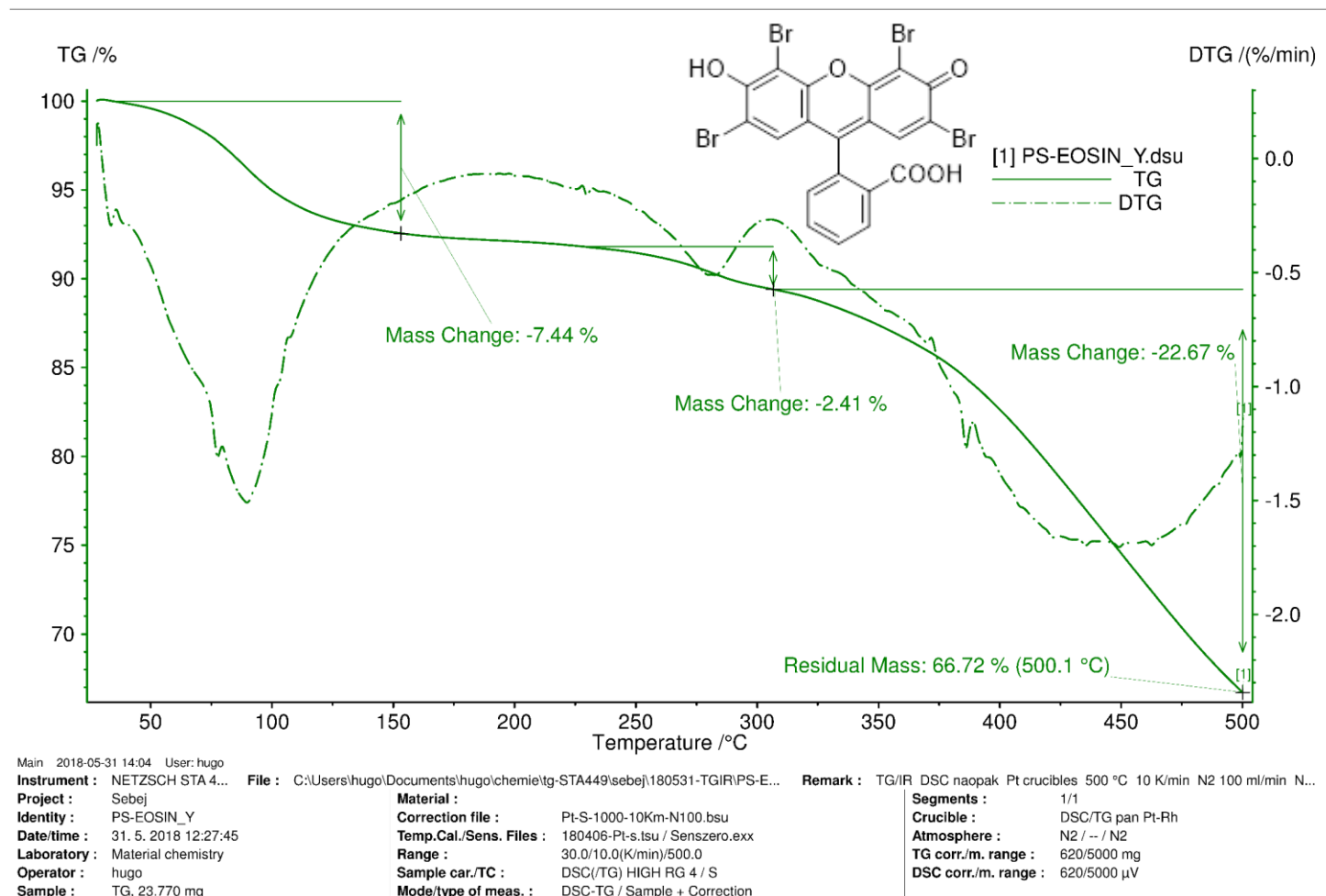


**Figure S53.** Differential thermal scanning calorimetry (DSC, blue line; left y-axis) and differential differential thermal scanning calorimetry (DDSC, blue dash-dot line; right y-axis) upon heating from 25 to 500 °C; the inflection points for each thermal process are indicated: eosin Y (2)

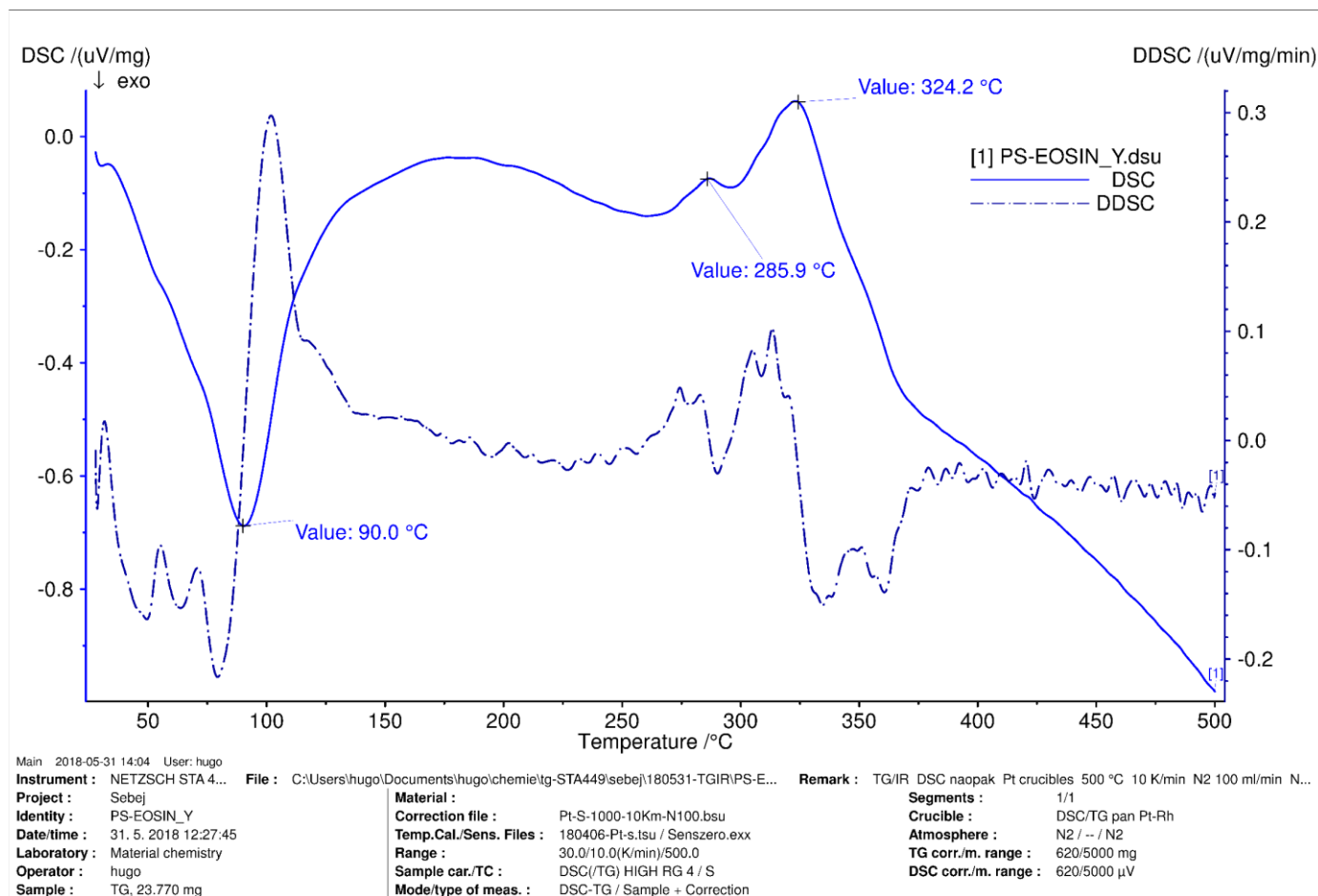
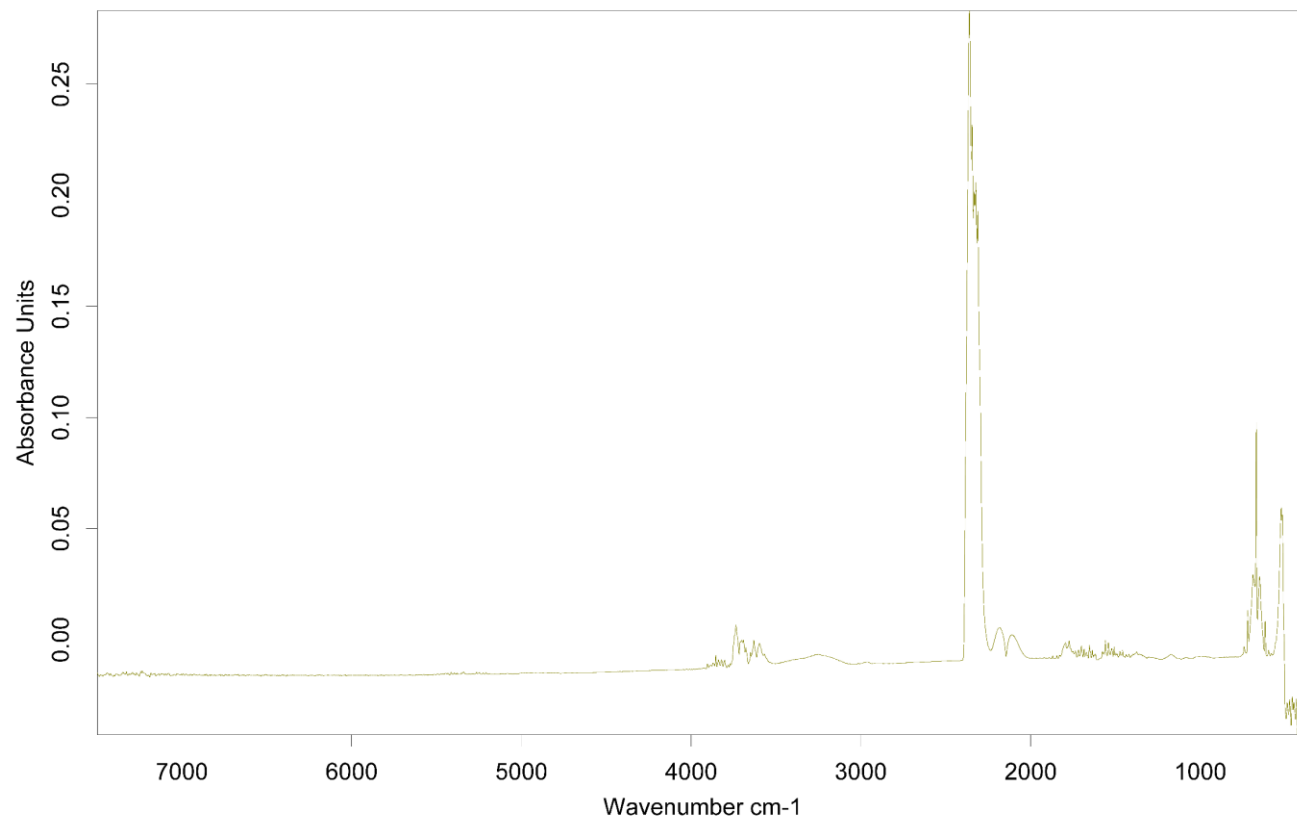


**Figure S54.** IR of the released gases during the thermal scanning calorimetry and thermogravimetric analysis upon heating from 25 to 500 °C: eosin Y (2)



PS-EOSIN_Y_0_AB_187_2636.529995_Seconds.0	TG	23.770   NETZSCH STA 449 C   C:\ngbwintal\data5\PS-EOSIN_Y.dsu	31. 5. 2018
---	----	--	-------------

**Figure S55.** Differential thermal scanning calorimetry (DSC, blue line; right y-axis) and thermogravimetric analysis (TG, green line; left y-axis) upon heating from 25 to 500 °C: rose bengal (**3**)

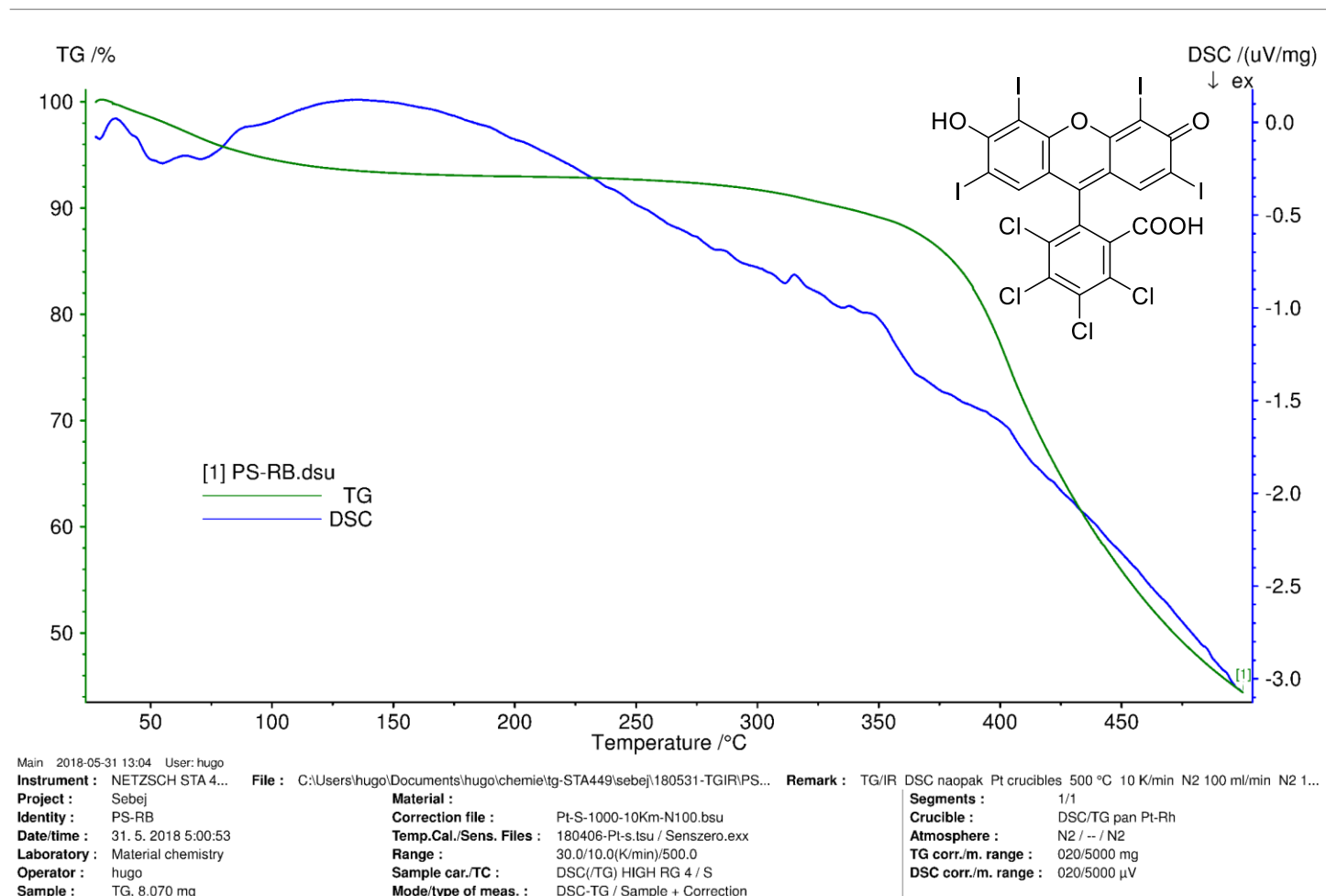


**Figure S56.** Differential thermogravimetric analysis (DTG, green dash-dot line; right y-axis) and thermogravimetric analysis (TG, solid green line; left y-axis) upon heating from 25 to 500 °C; the mass changes for each process and residual mass at 500 °C are indicated: rose bengal (**3**)

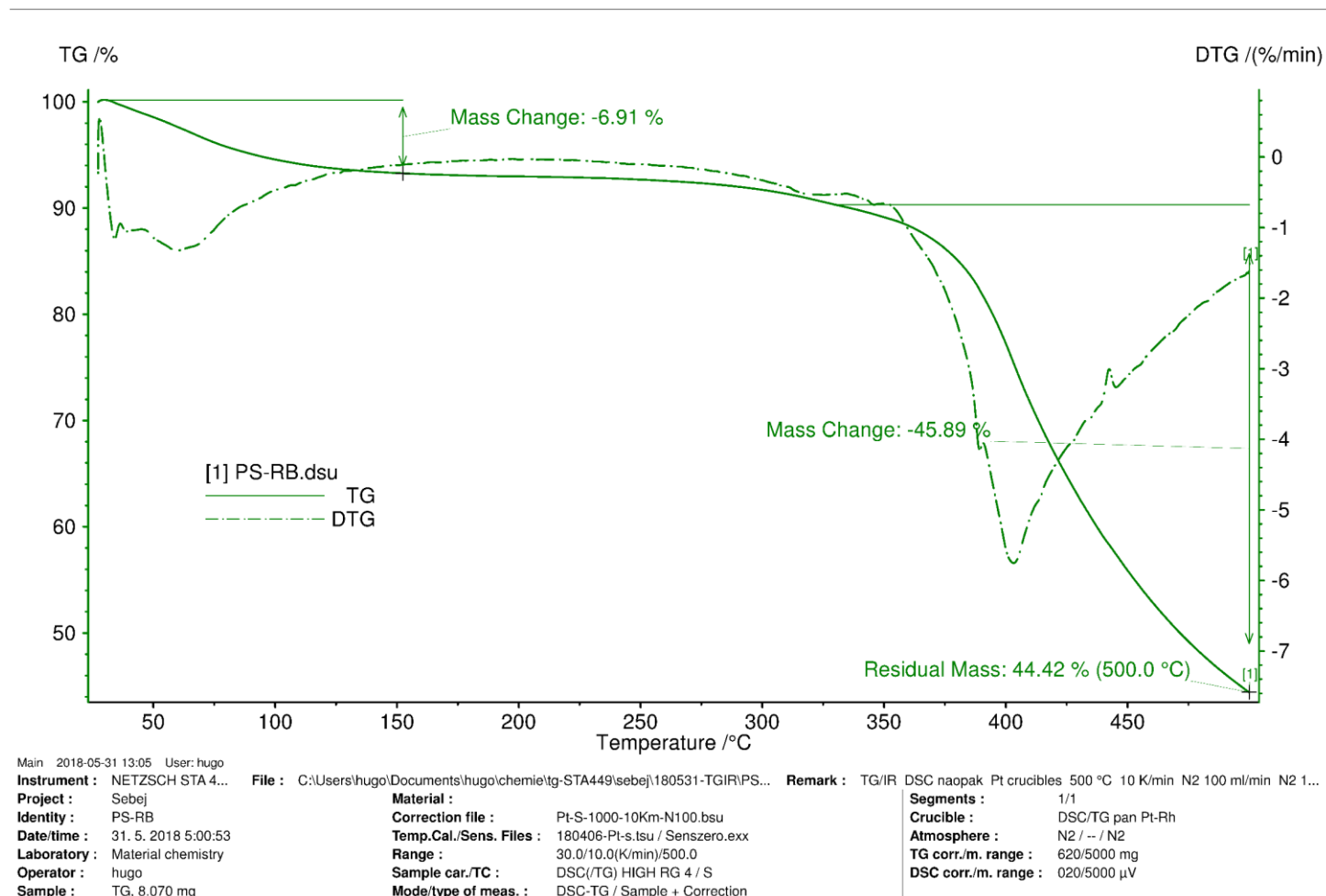


**Figure S57.** Differential thermal scanning calorimetry (DSC, blue line; left y-axis) and differential differential thermal scanning calorimetry (DDSC, blue dash-dot line; right y-axis) upon heating from 25 to 500 °C; the inflection points for each thermal process are indicated: rose bengal (3)

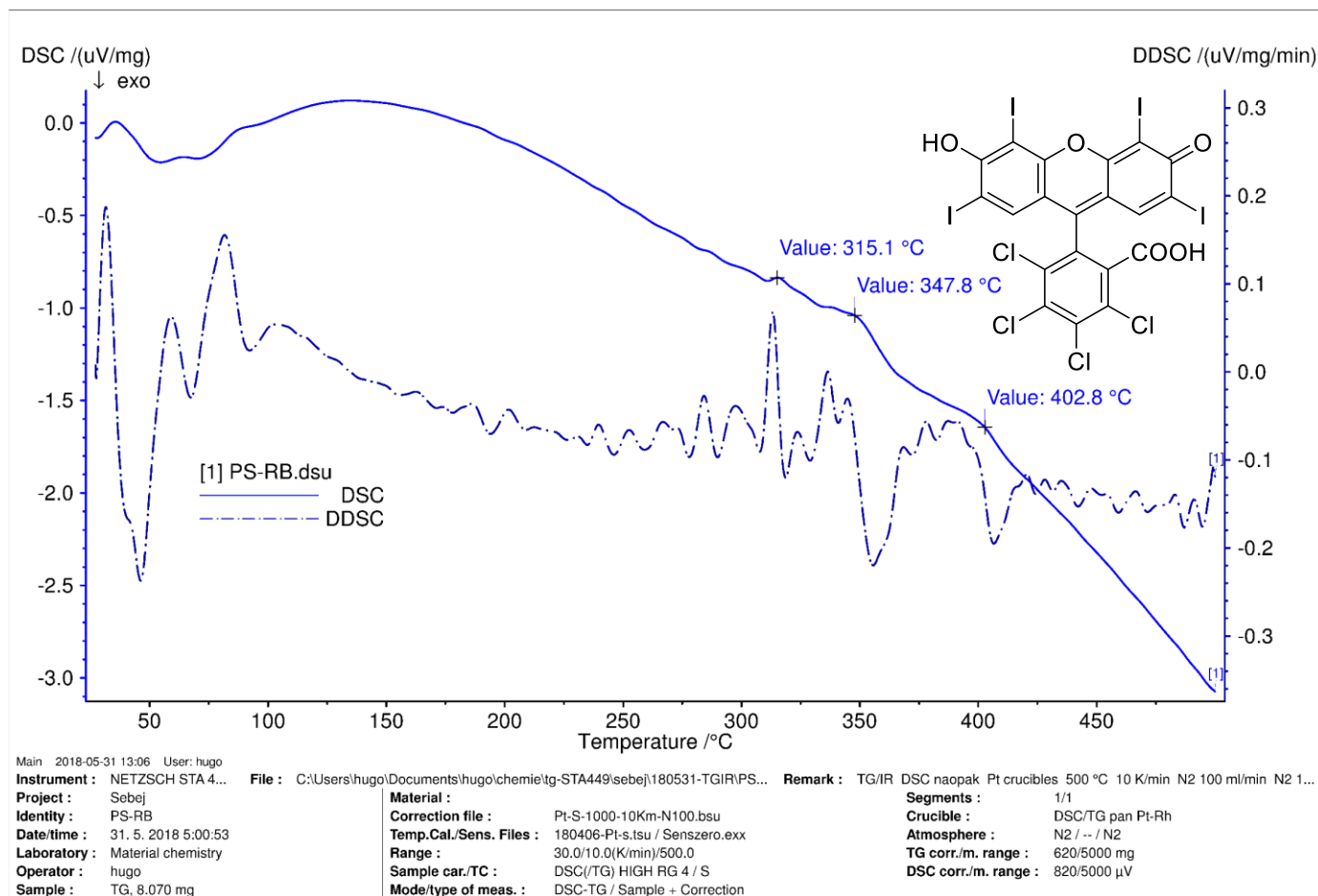
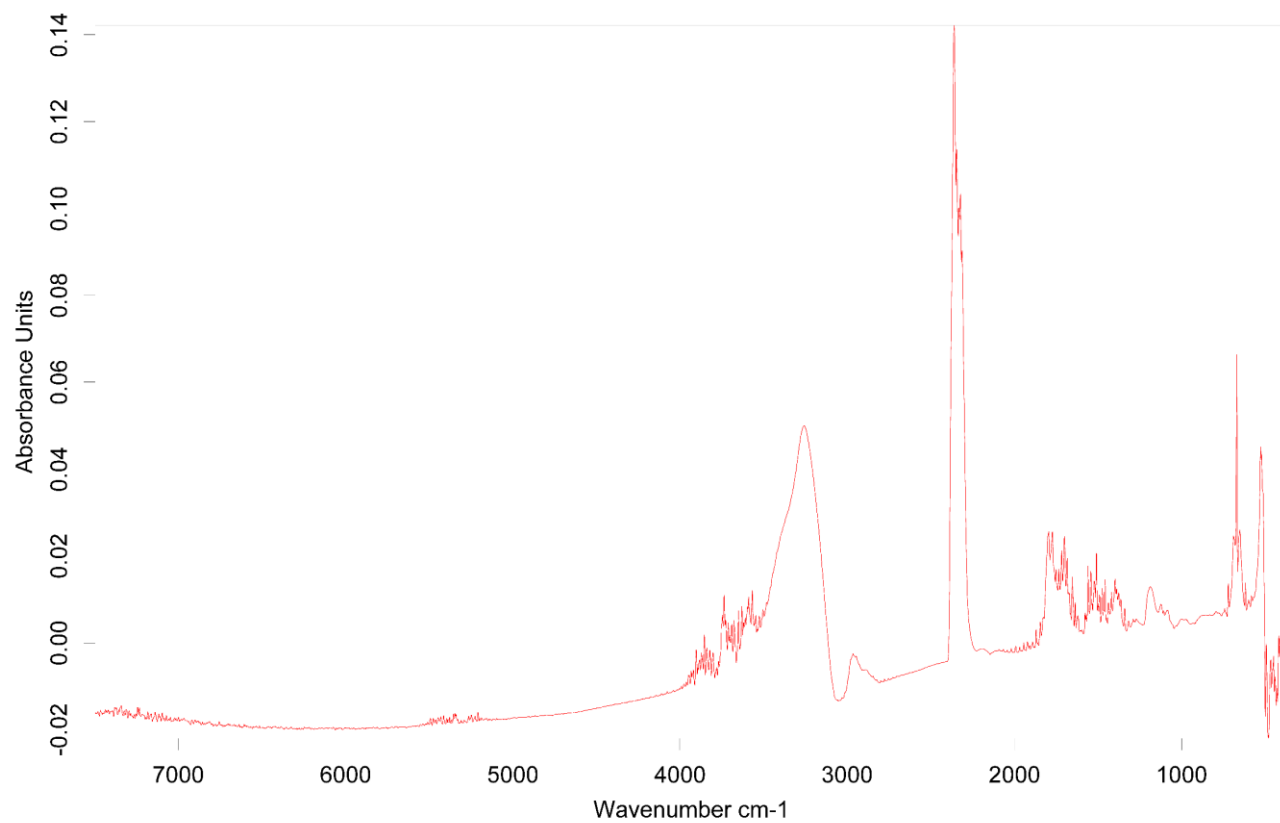


**Figure S58.** IR of the released gases during the thermal scanning calorimetry and thermogravimetric analysis upon heating from 25 to 500 °C: rose bengal (3)



PS-RB.0_AB_169_2384.147998_Seconds.0	TG	8.070   NETZSCH STA 449 C   C:\ngbwin\ta\data5\PS-RB.dsu	31. 5. 2018
--------------------------------------	----	--	-------------

**Figure S59.** TIC of a) sample of **1** ( $c(\text{dye}) = 3 \times 10^{-5} \text{ mol dm}^{-3}$ ) in aerated aqueous PBS buffer ( $\text{pH} = 7.4$ ,  $I = 0.1 \text{ mol dm}^{-3}$ ) and irradiated with three white-light LED reflectors for 4 days and then processed using method A (blue solid line); and b) samples of water (blank) (red solid line).

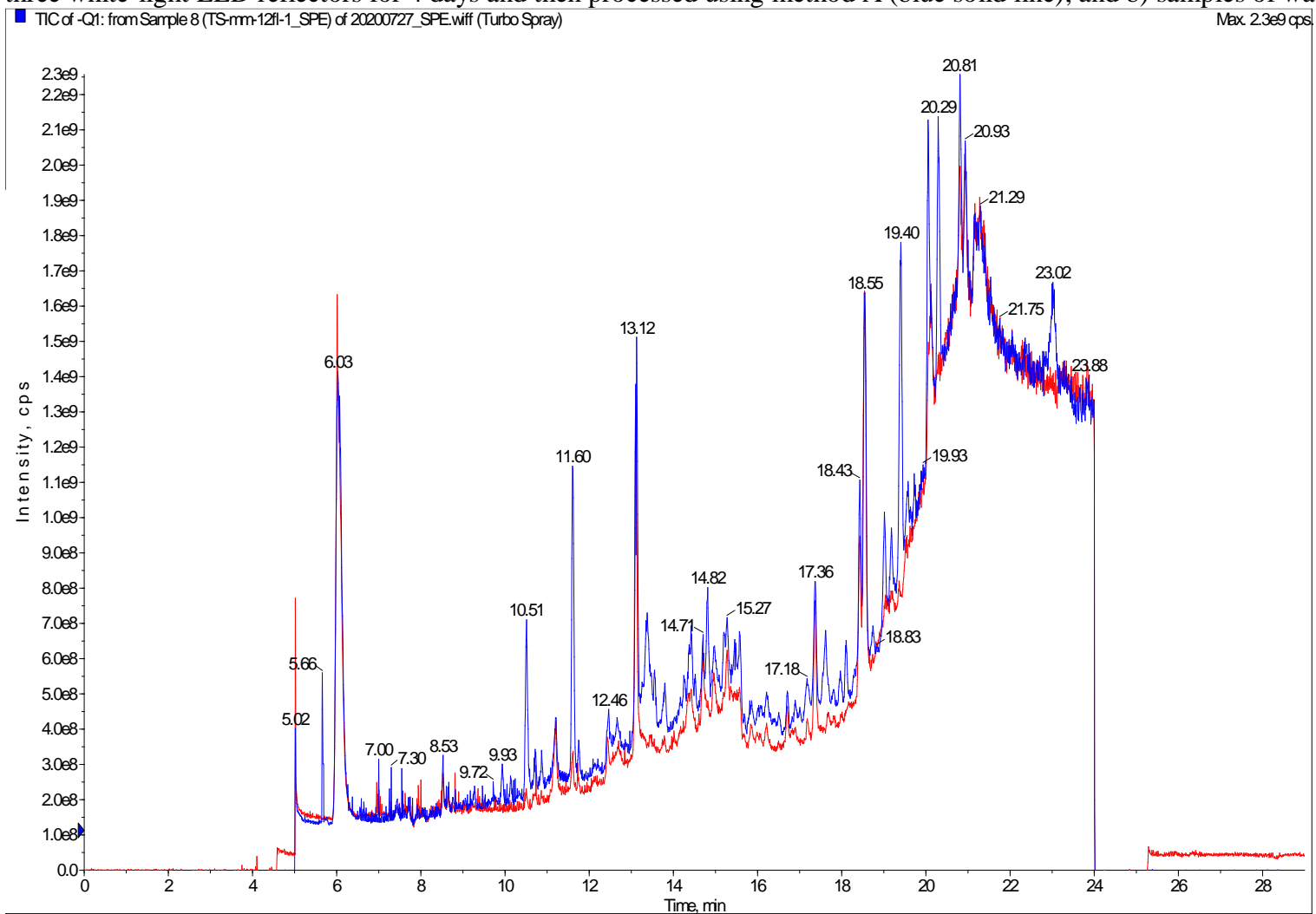


**Figure S60.** ESI mass spectrum (negative mode; bottom panel) of an aerated PBS solution of photoproduct mixture obtained upon irradiation of **1** with white-light LED reflectors and processed using method A processing. The mass spectrum shown is calculated for the grey area (highlighted in the chromatogram; upper panel) with a maximum in  $t = 10.51$  min.

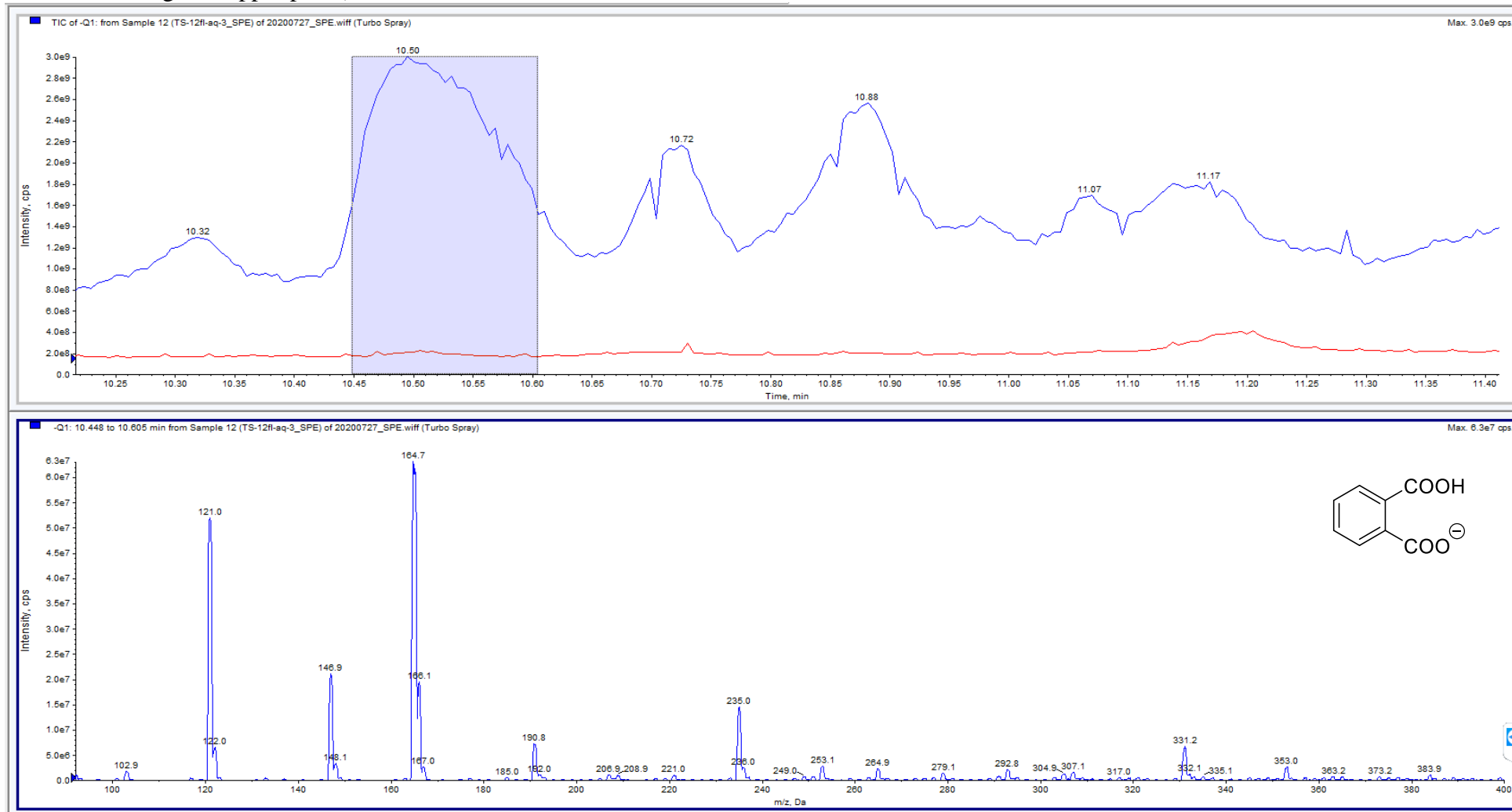


**Figure S61.** ESI mass spectrum (negative mode; bottom panel) of an aerated PBS solution of photoproduct mixture obtained upon irradiation of **1** with white-light LED reflectors and processed using method A processing. The mass spectrum shown is calculated for the grey area (highlighted in the chromatogram; upper panel) with a maximum in  $t = 11.62$  min.

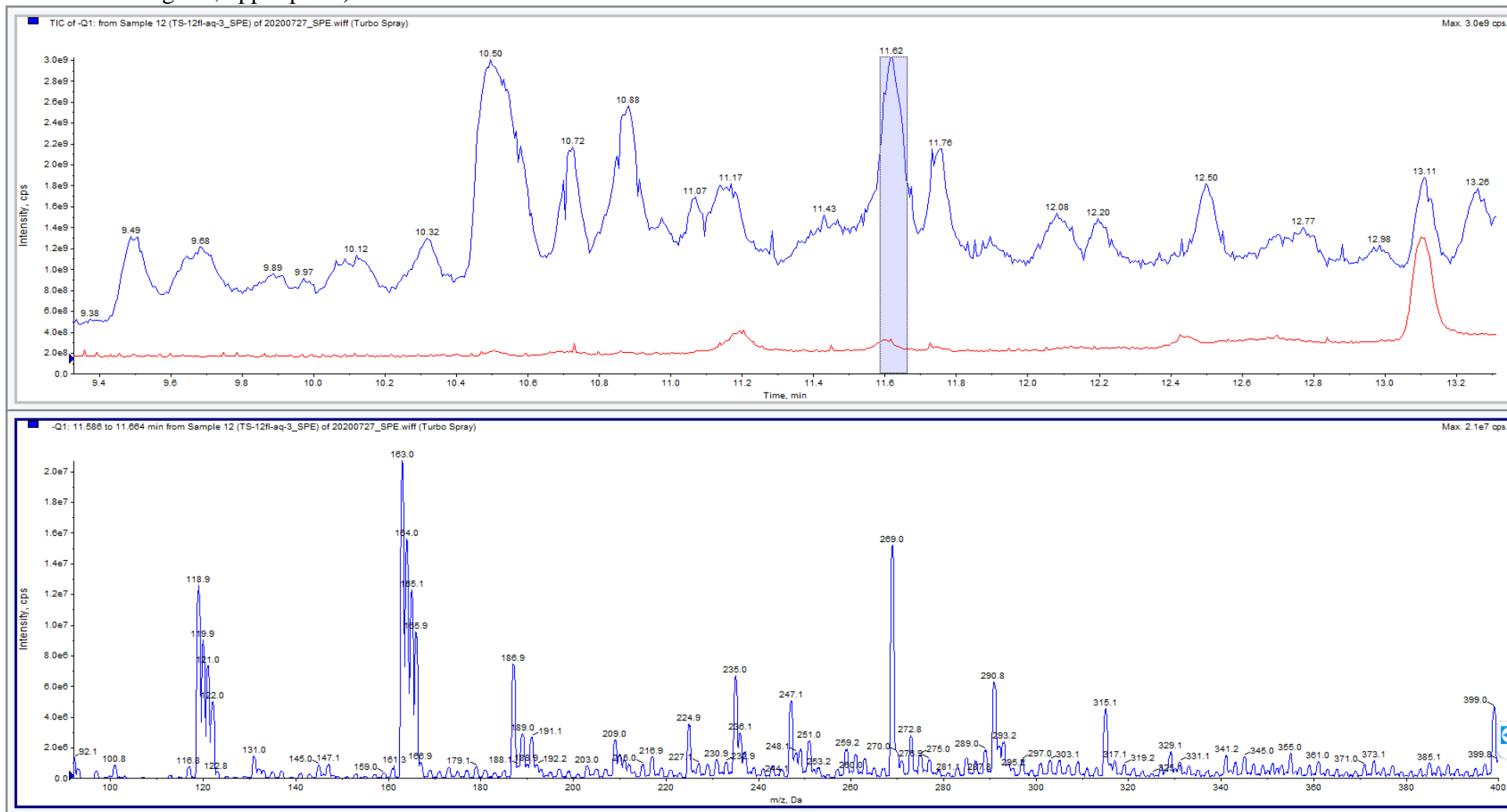


**Figure S62.** ESI mass spectrum (negative mode; bottom panel) of an aerated PBS solution of photoproduct mixture obtained upon irradiation of **1** with white-light LED reflectors and processed using method A processing. The mass spectrum shown is calculated for the grey area (highlighted in the chromatogram; upper panel) with a maximum in  $t = 13.38$  min.

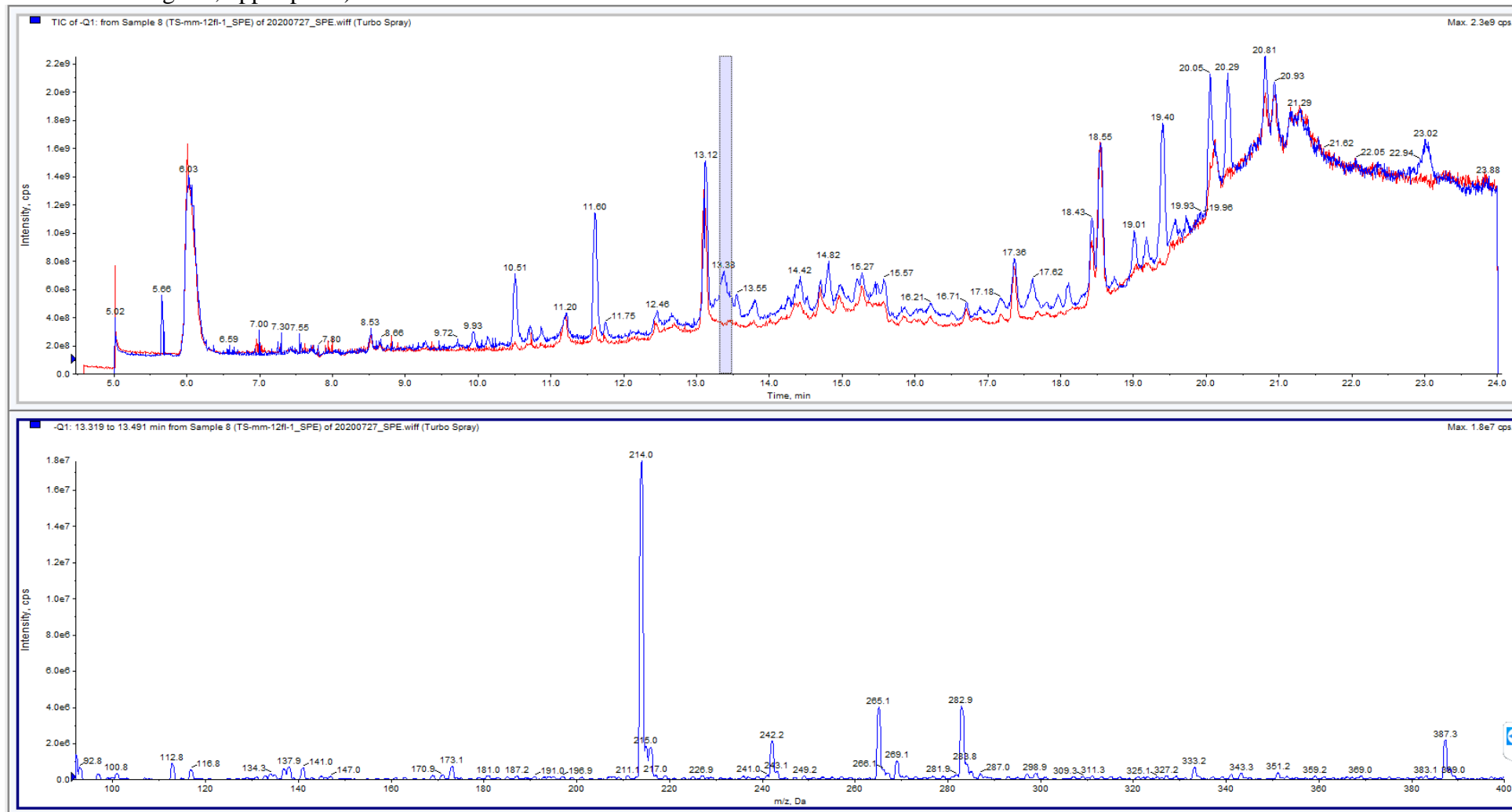


**Figure S63.** ESI mass spectrum (negative mode; bottom panel) of an aerated PBS solution of photoproduct mixture obtained upon irradiation of **1** with white-light LED reflectors and processed using method A processing. The mass spectrum shown is calculated for the grey area (highlighted in the chromatogram; upper panel) with a maximum in  $t = 16.19$  min.

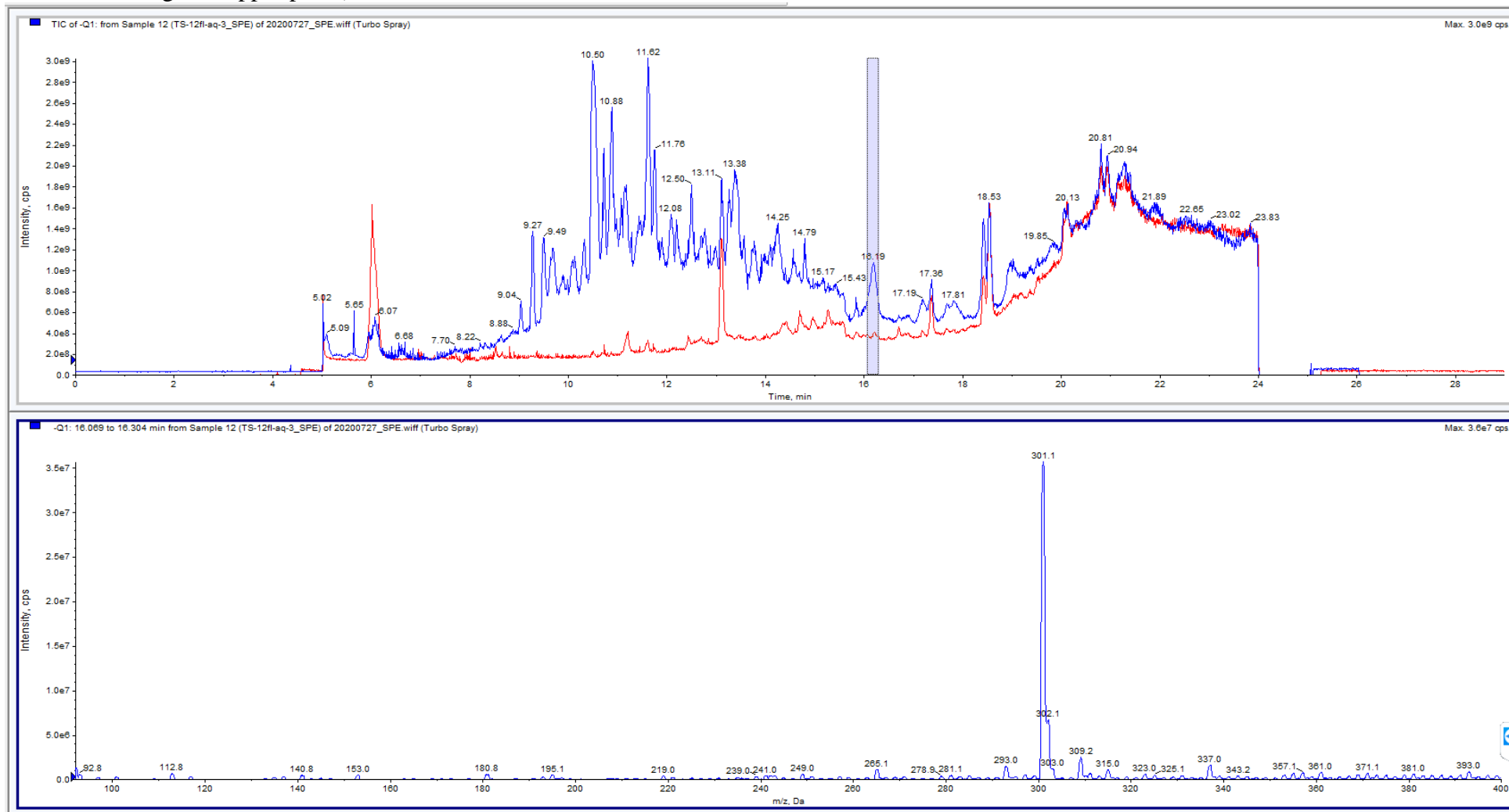


**Figure S64.** Chromatograms of a) sample of [ $^{13}\text{C}_2$ ]-**1** ( $c(\text{dye}) = 3 \times 10^{-5} \text{ mol dm}^{-3}$ ) in an aerated aqueous PBS buffer ( $\text{pH} = 7.4$ ,  $I = 0.1 \text{ mol dm}^{-3}$ ) irradiated with white-light LED reflectors for 4 days and then processed using method A (blue solid line); and b) samples of water (blank) (red solid line).

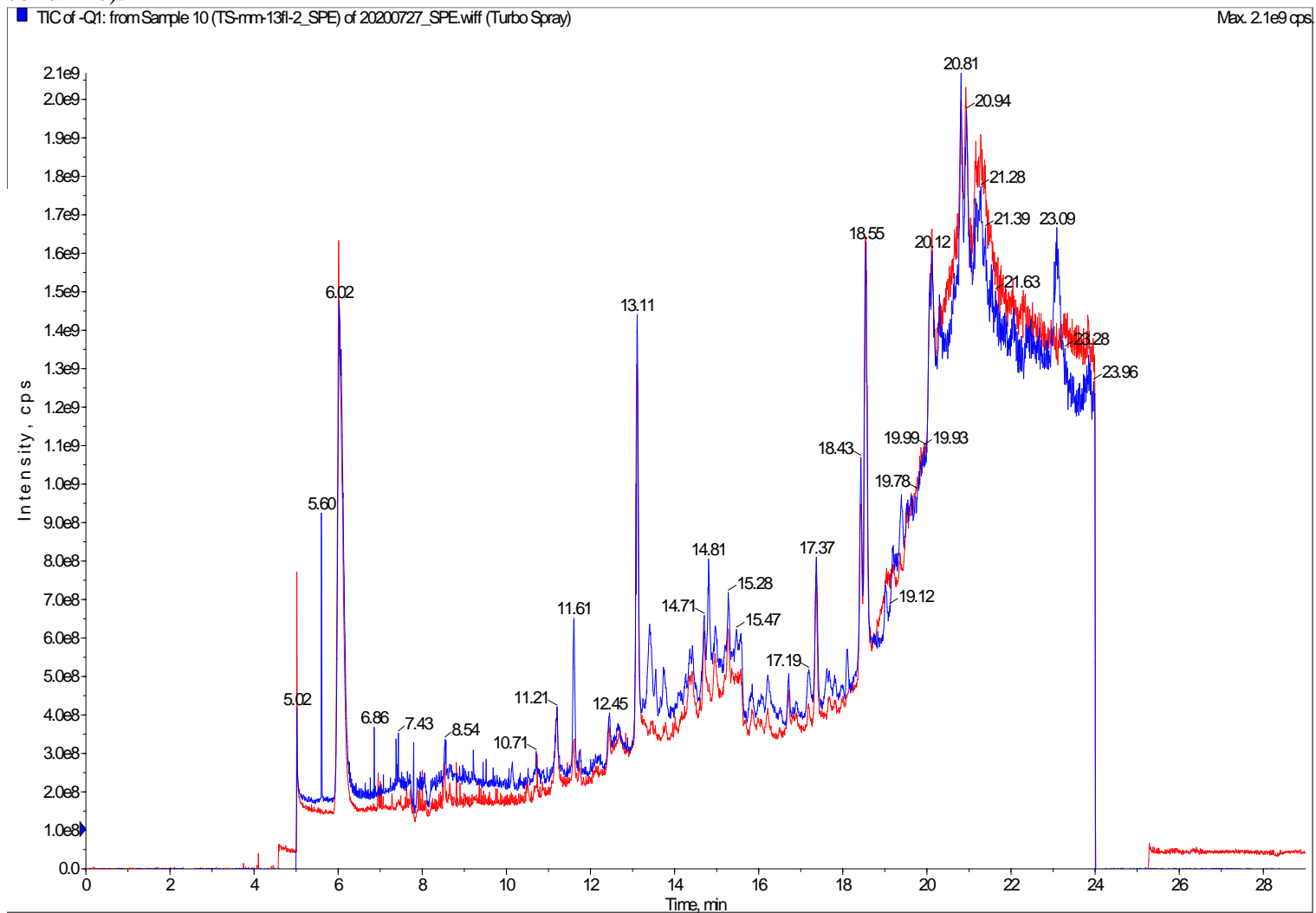


**Figure S65.** ESI mass spectrum (negative mode; bottom panel) of an aerated PBS solution of photoproduct mixture obtained upon irradiation of [ $^{13}\text{C}_2$ ]-**1** with white-light LED reflectors and processed using method A processing. The mass spectrum shown is calculated for the grey area (highlighted in the chromatogram; upper panel) with a maximum in  $t = 10.51$  min.

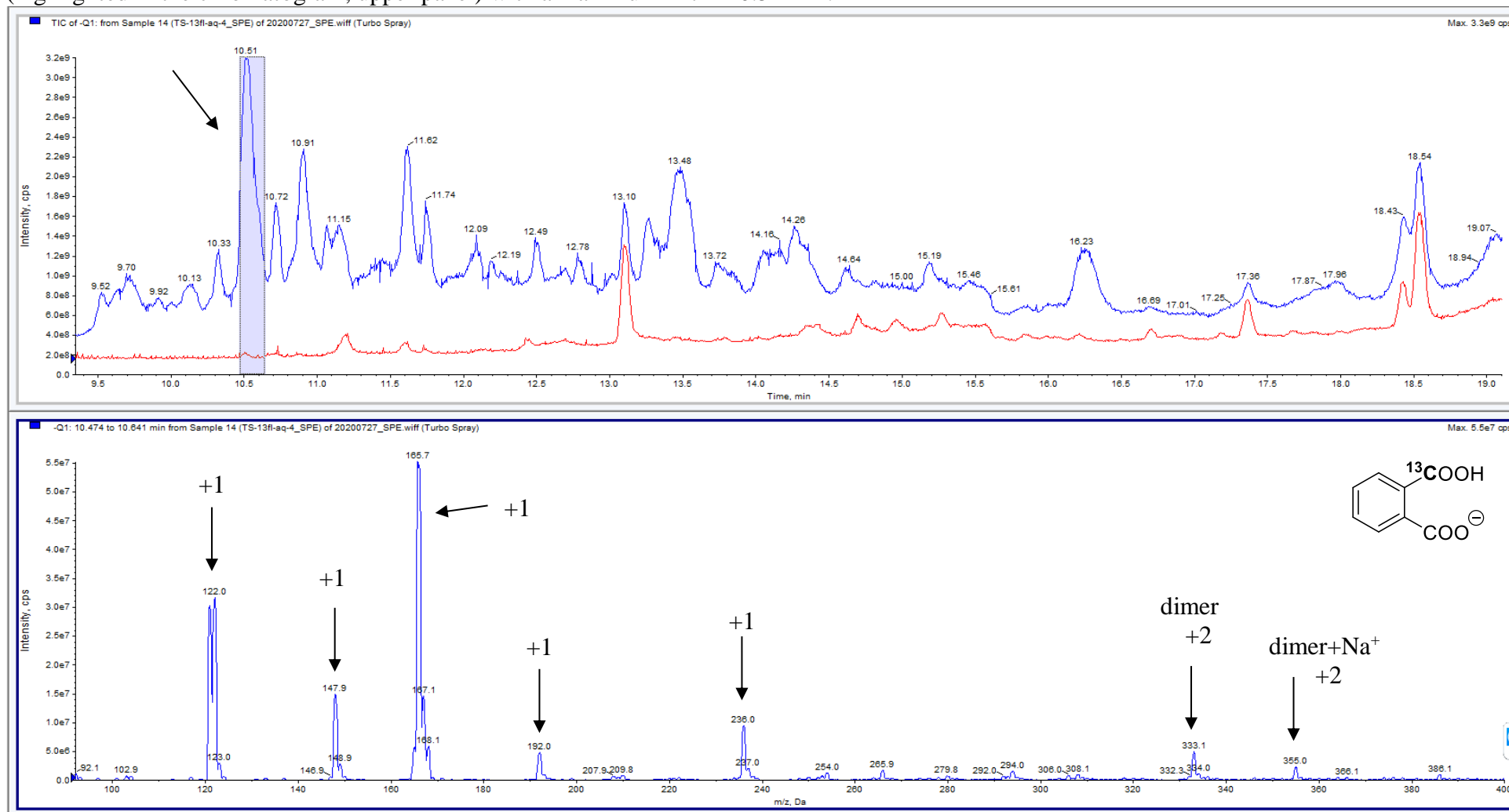


**Figure S66.** ESI mass spectrum (negative mode; bottom panel) of an aerated PBS solution of photoproduct mixture obtained upon irradiation of [ $^{13}\text{C}_2$ ]-**1** with white-light LED reflectors and processed using method A processing. The mass spectrum shown is calculated for the grey area (highlighted in the chromatogram; upper panel) with a maximum in  $t = 11.62$  min.

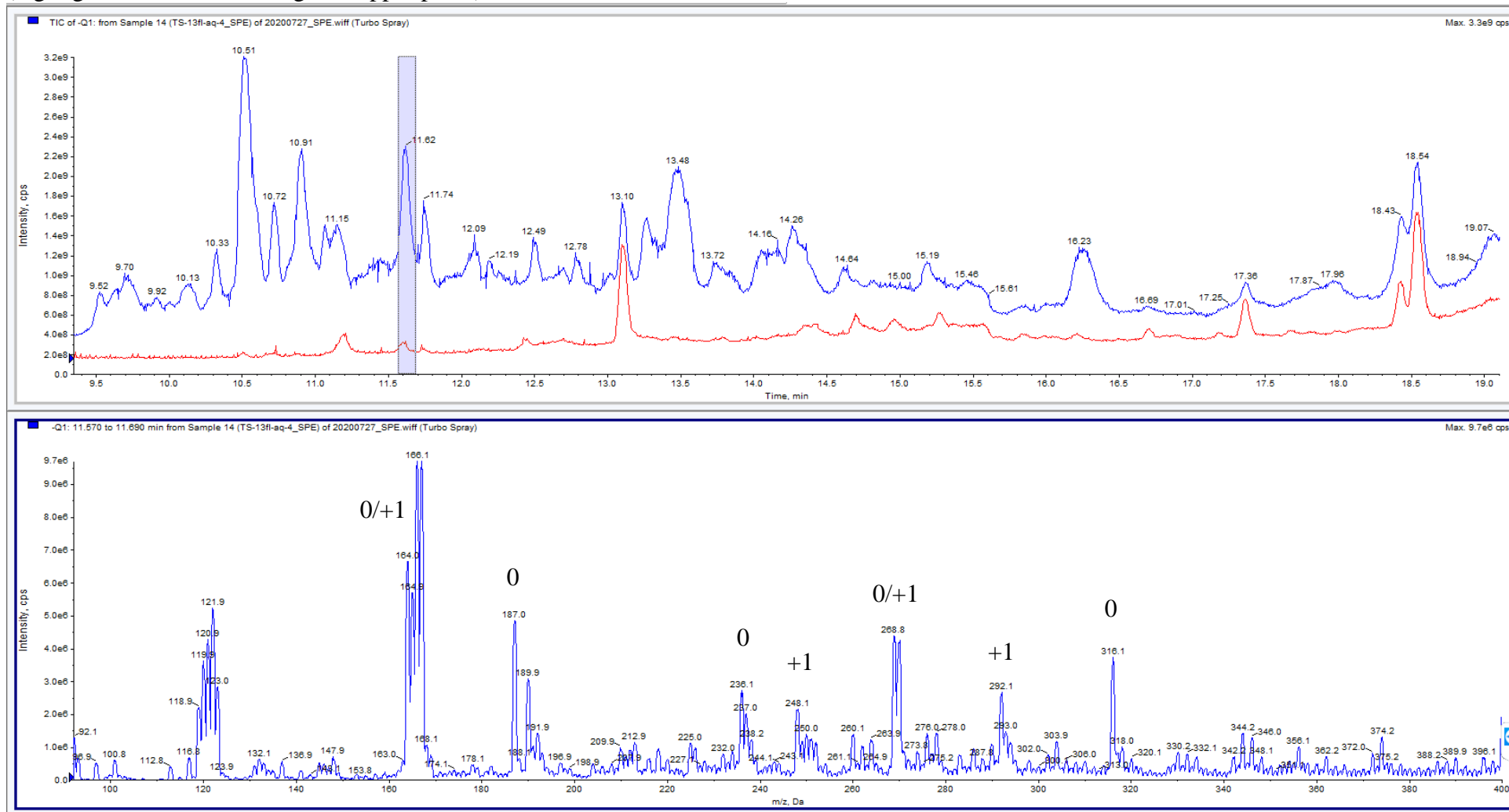


**Figure S67.** ESI mass spectrum (negative mode; bottom panel) of an aerated PBS solution of photoproduct mixture obtained upon irradiation of [ $^{13}\text{C}_2$ ]-**1** with white-light LED reflectors and processed using method A processing. The mass spectrum shown is calculated for the grey area (highlighted in the chromatogram; upper panel) with a maximum in  $t = 13.48$  min.

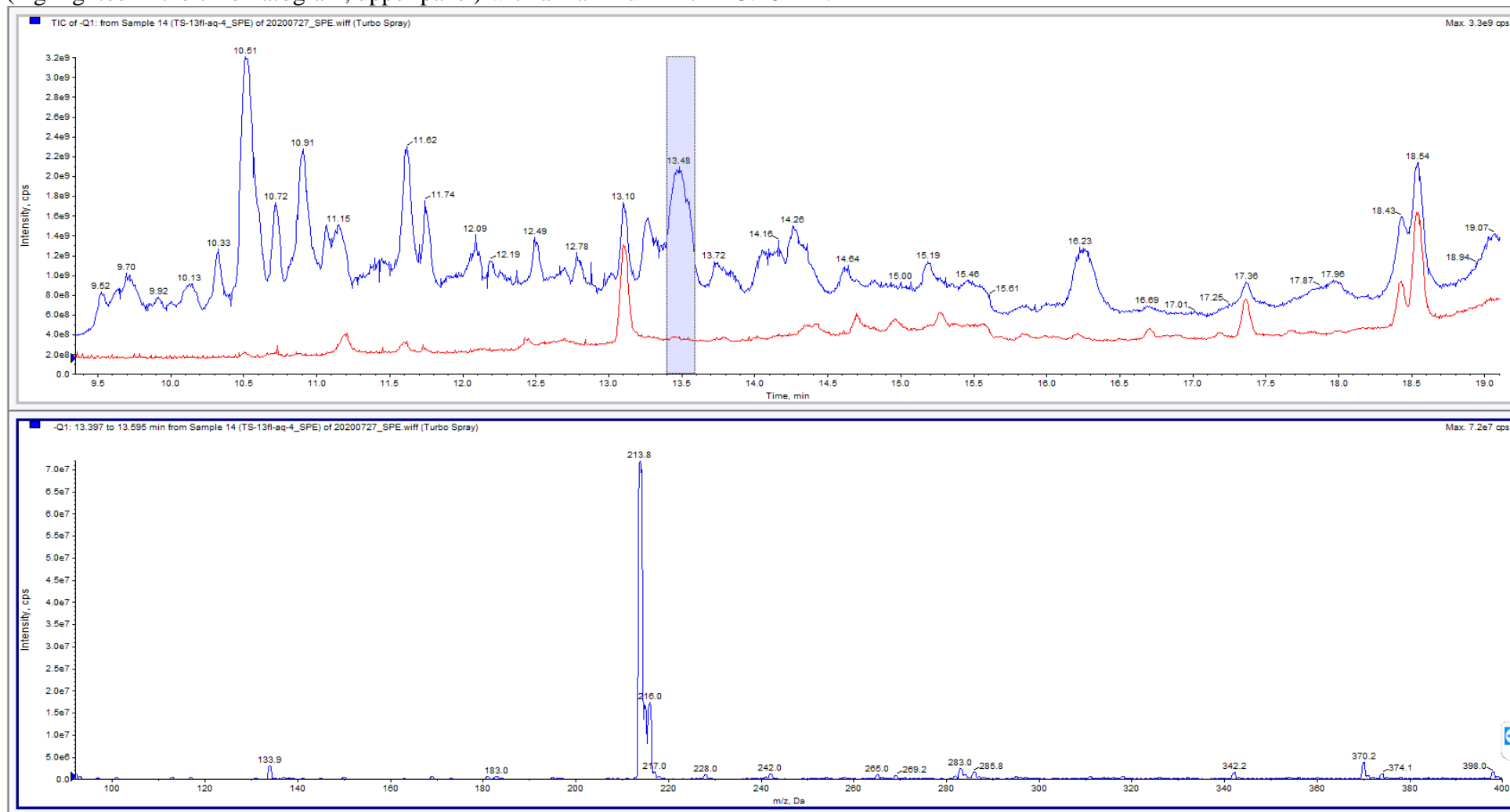


**Figure S68.** ESI mass spectrum (negative mode; bottom panel) of an aerated PBS solution of photoproduct mixture obtained upon irradiation of [ $^{13}\text{C}_2$ ]-**1** with white-light LED reflectors and processed using method A processing. The mass spectrum shown is calculated for the grey area (highlighted in the chromatogram; upper panel) with a maximum in  $t = 16.23$  min.

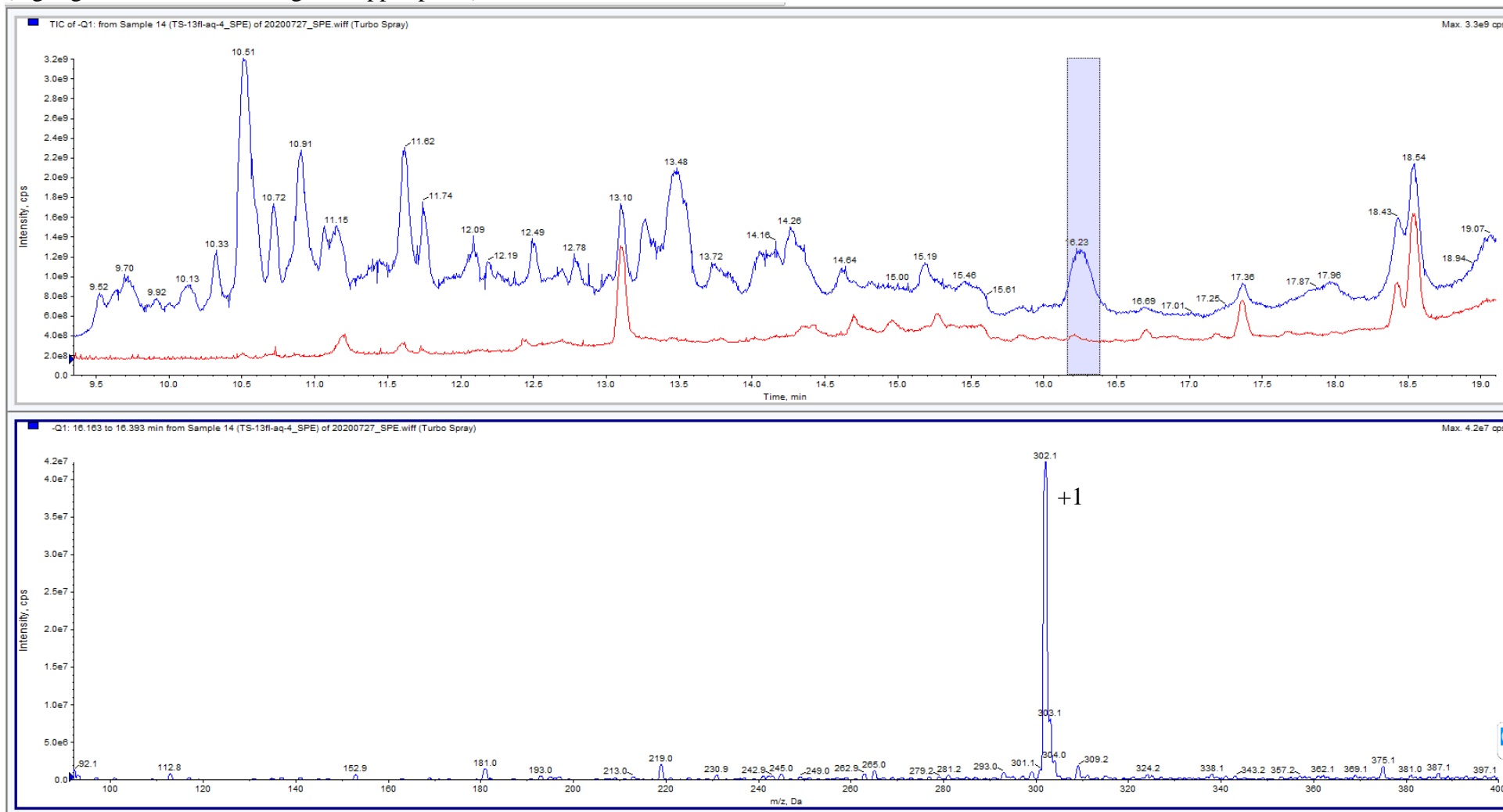


**Figure S69.** Chromatograms of a) sample of **1** ( $c(\text{dye}) = 3 \times 10^{-5} \text{ mol dm}^{-3}$ ) in deoxygenated (argon bubbled for 15 min) aqueous PBS buffer (pH = 7.4,  $I = 0.1 \text{ mol dm}^{-3}$ ) and irradiated with white-light LED reflectors for 4 days and then processed using method A (solid blue line); and b) samples of water (blank) (solid red line).

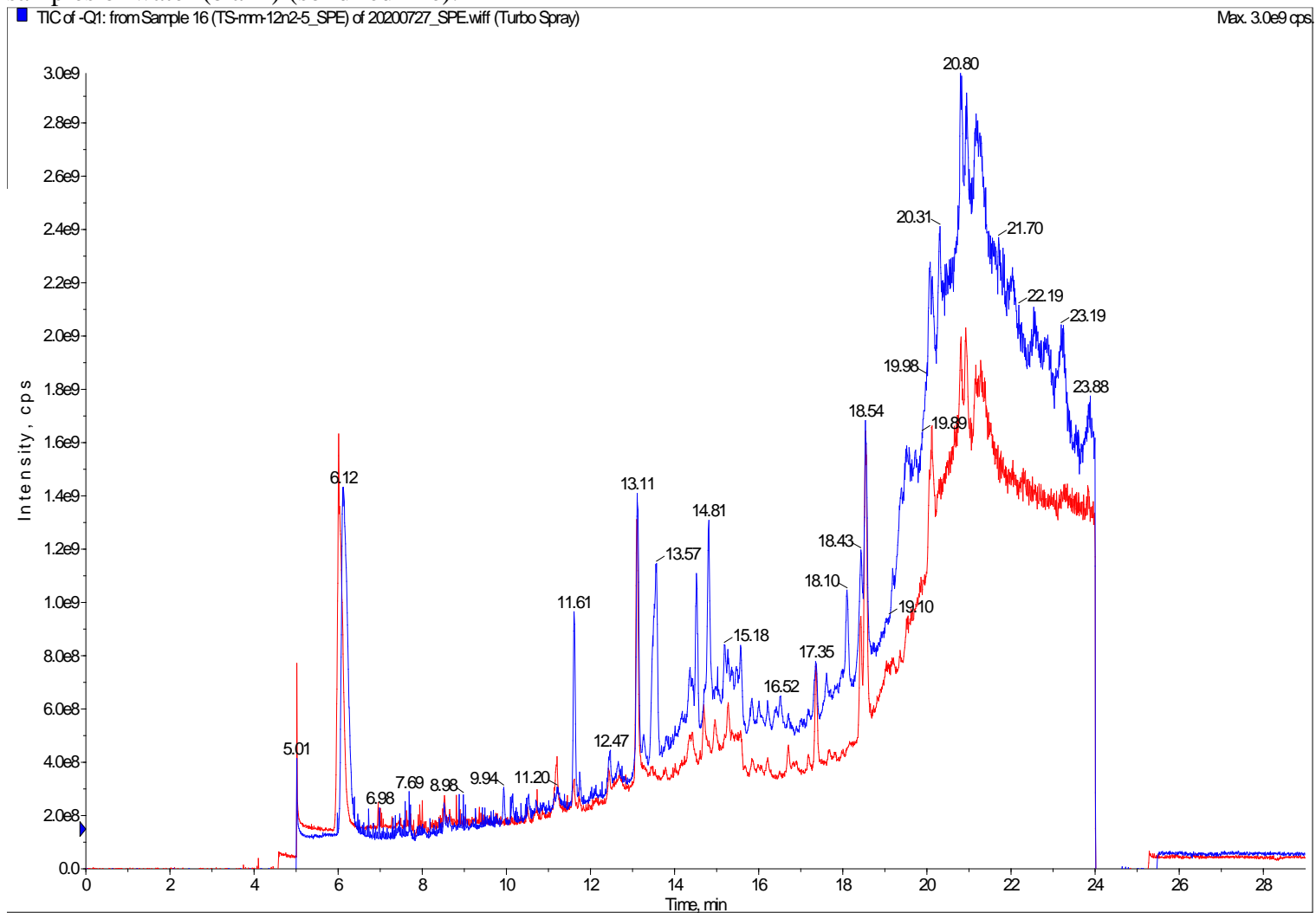


**Figure S70.** ESI mass spectrum (negative mode; bottom panel) of a deoxygenated PBS solution of photoproduct mixture obtained upon irradiation of [ $^{13}\text{C}_2$ ]-1 with white-light LED reflectors and processed using method A processing. The mass spectrum shown is calculated for the grey area (highlighted in the chromatogram; upper panel) with a maximum in  $t = 11.51$  min.

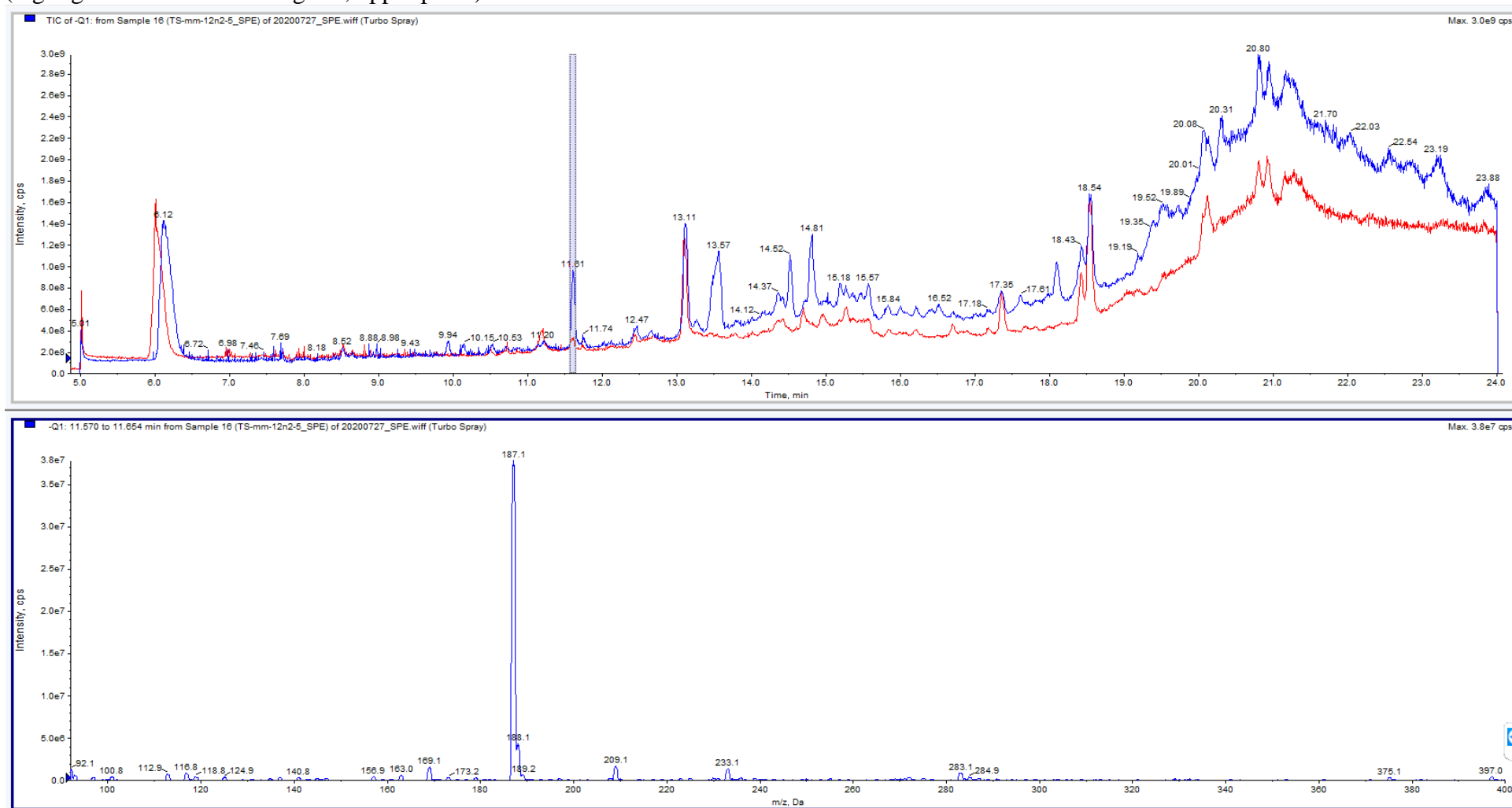


**Figure S71.** ESI mass spectrum (negative mode; bottom panel) of a deoxygenated PBS solution of photoproduct mixture obtained upon irradiation of [ $^{13}\text{C}_2$ ]-1 with white-light LED reflectors and processed using method A processing. The mass spectrum shown is calculated for the grey area (highlighted in the chromatogram; upper panel) with a maximum in  $t = 13.57$  min.

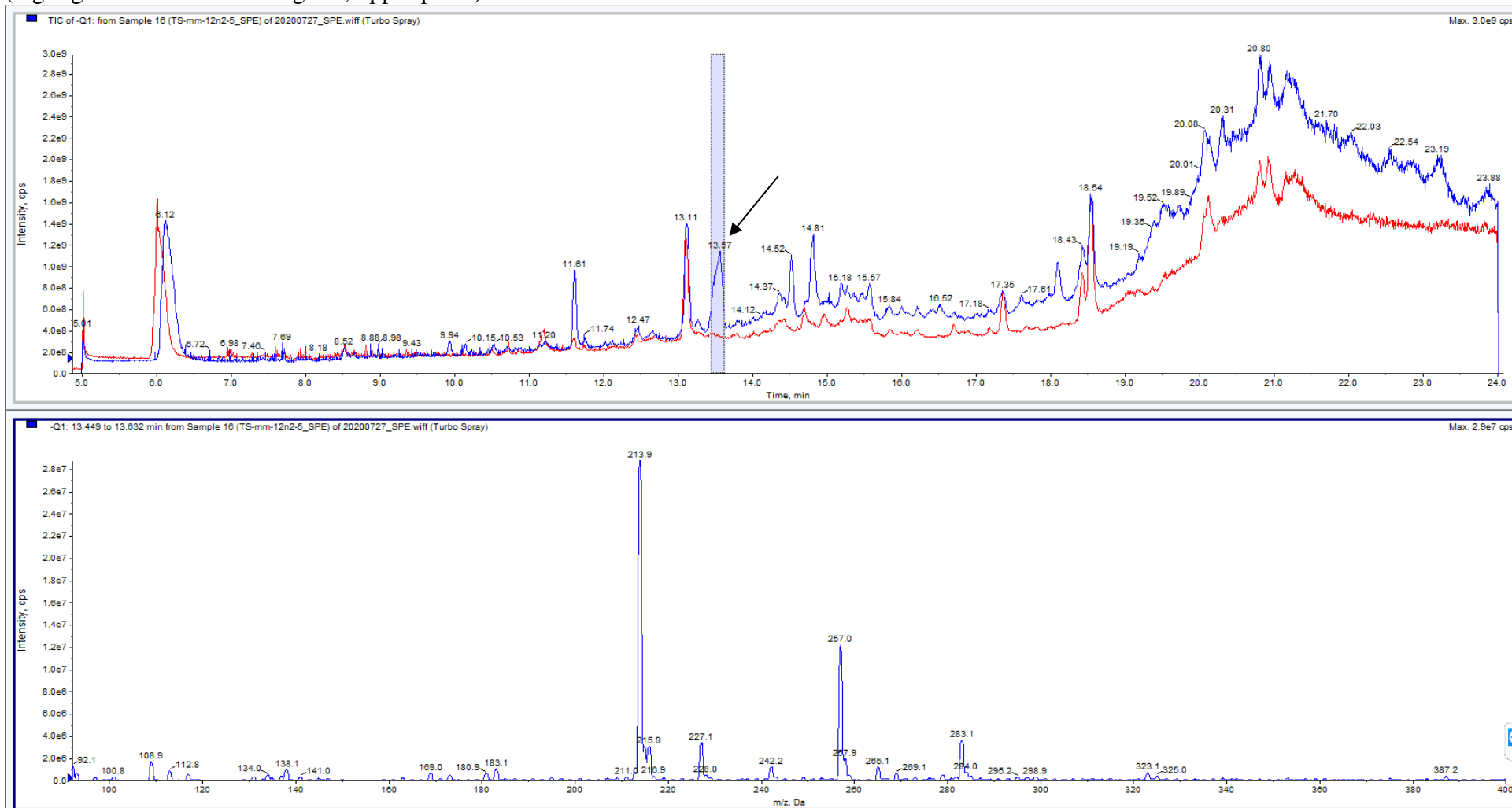


**Figure S72.** ESI mass spectrum (negative mode; bottom panel) of a deoxygenated PBS solution of photoproduct mixture obtained upon irradiation of [ $^{13}\text{C}_2$ ]-1 with white-light LED reflectors and processed using method A processing. The mass spectrum shown is calculated for the grey area (highlighted in the chromatogram; upper panel) with a maximum in  $t = 14.52$  min.

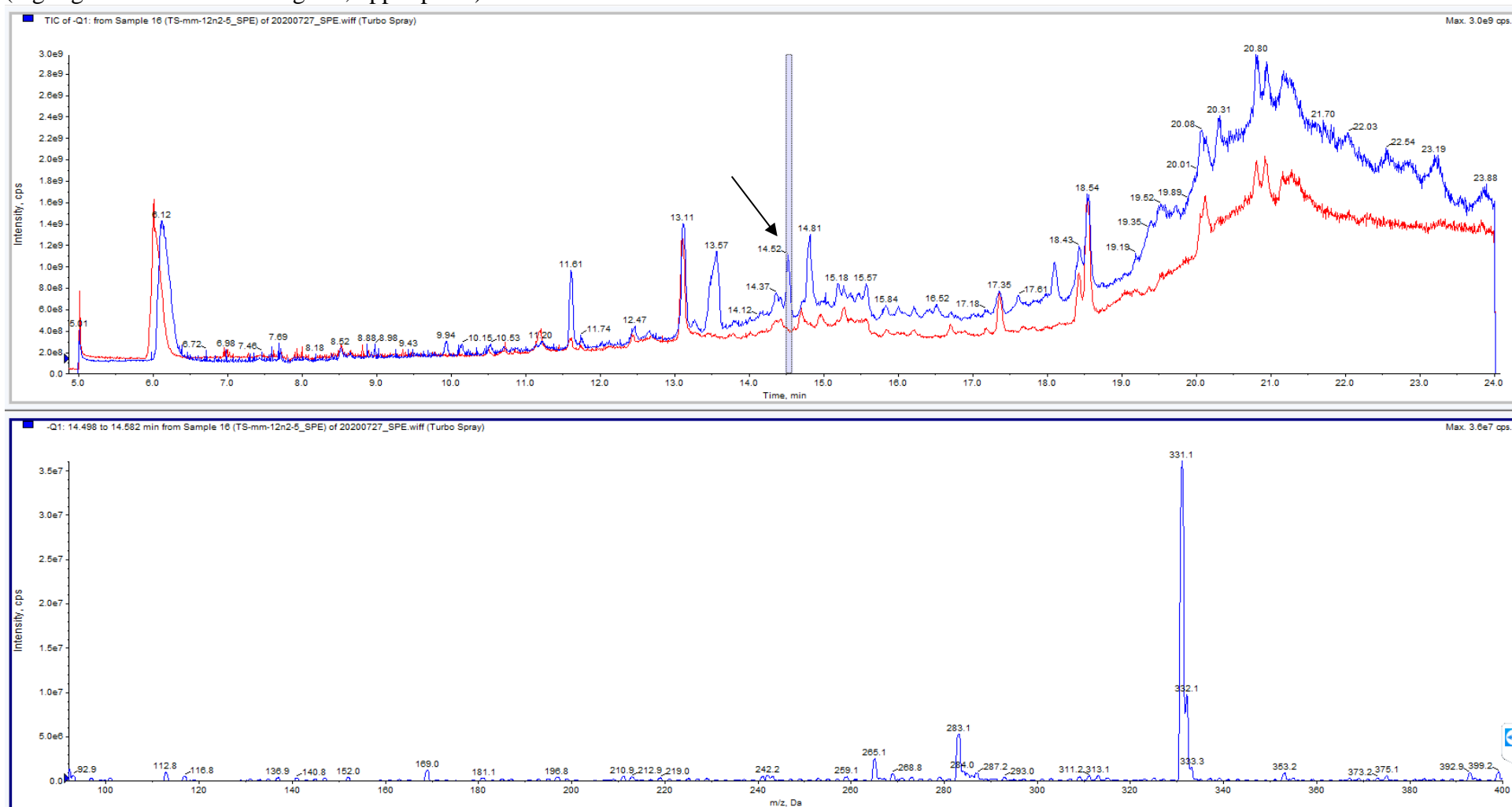


**Figure S73.** ESI mass spectrum (negative mode; bottom panel) of a deoxygenated PBS solution of photoproduct mixture obtained upon irradiation of [ $^{13}\text{C}_2$ ]-1 with white-light LED reflectors and processed using method A processing. The mass spectrum shown is calculated for the grey area (highlighted in the chromatogram; upper panel) with a maximum in  $t = 14.81$  min.

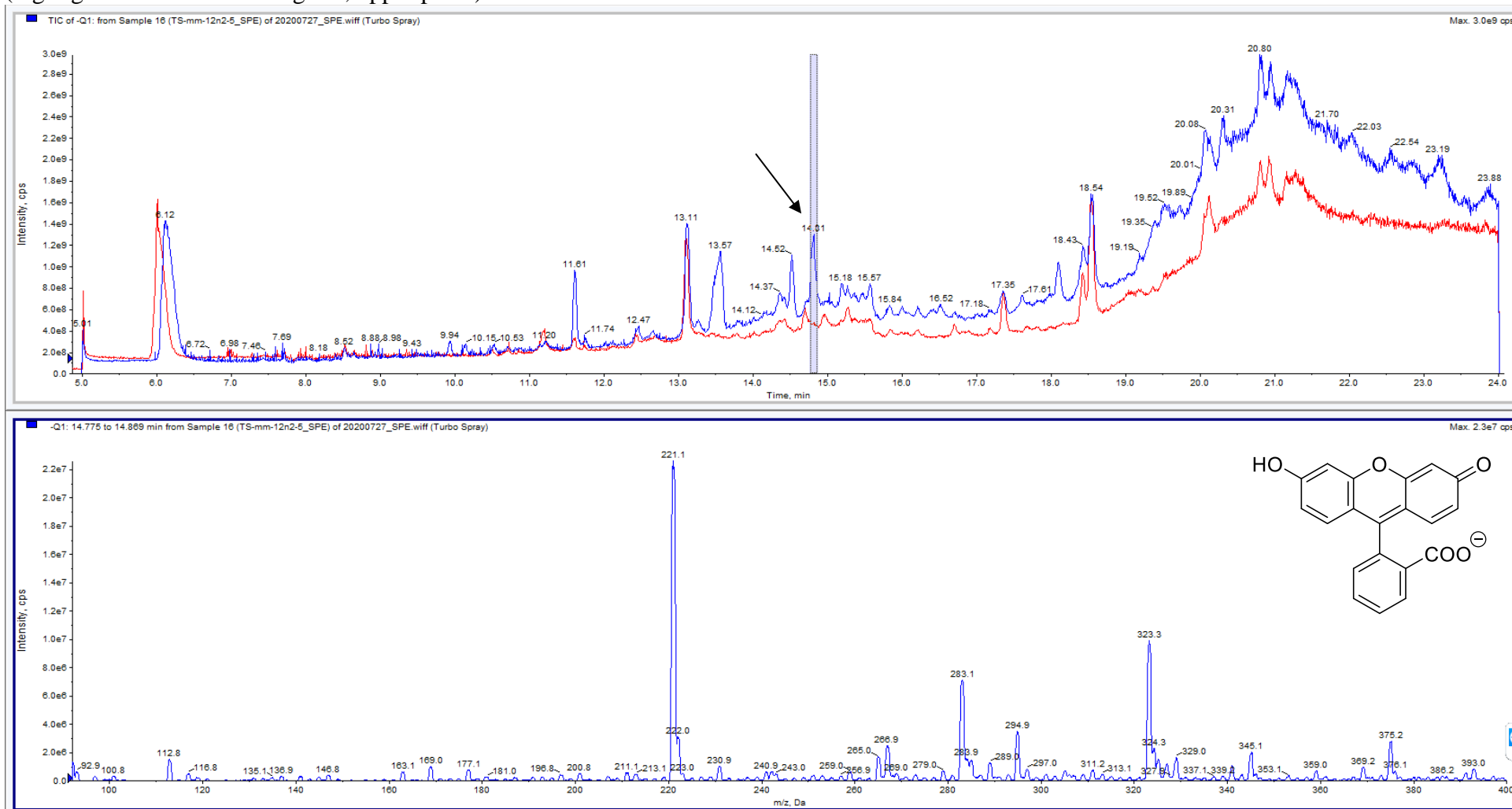


**Figure S74.** Chromatograms of a) sample of **1** ( $c(\text{dye}) = 3 \times 10^{-5} \text{ mol dm}^{-3}$ ) in aerated aqueous PBS buffer ( $\text{pH} = 7.4$ ,  $I = 0.1 \text{ mol dm}^{-3}$ ) and irradiated with white-light LED reflectors for 4 days and then processed using method B (solid blue line); and b) samples of water (blank) (solid red line).

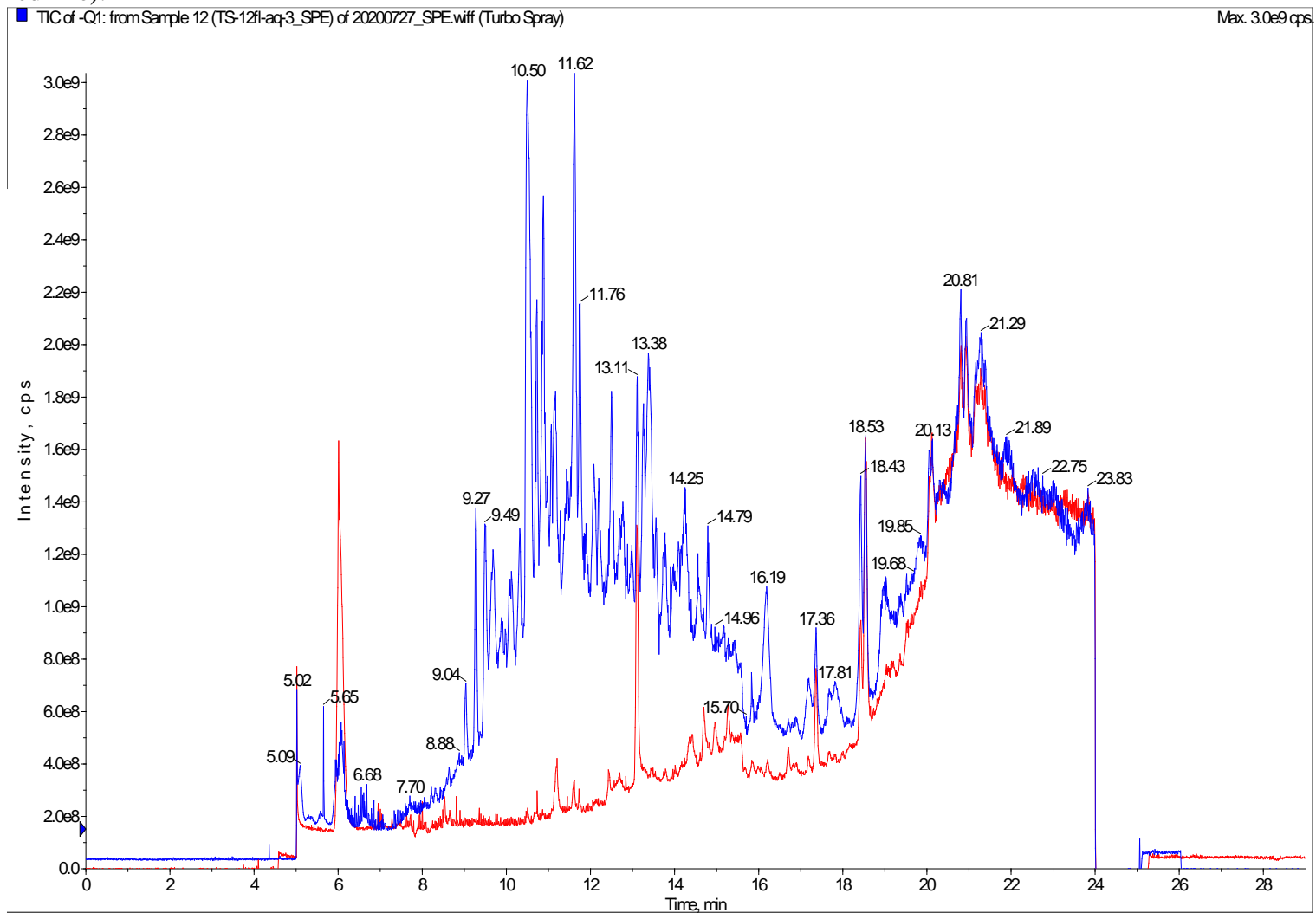


**Figure S75.** ESI mass spectrum (negative mode; bottom panel) of a aerated PBS solution of photoproduct mixture obtained upon irradiation of **1** with white-light LED reflectors and processed using method A processing. The mass spectrum shown is calculated for the grey area (highlighted in the chromatogram; upper panel) with a maximum in  $t = 10.51$  min.

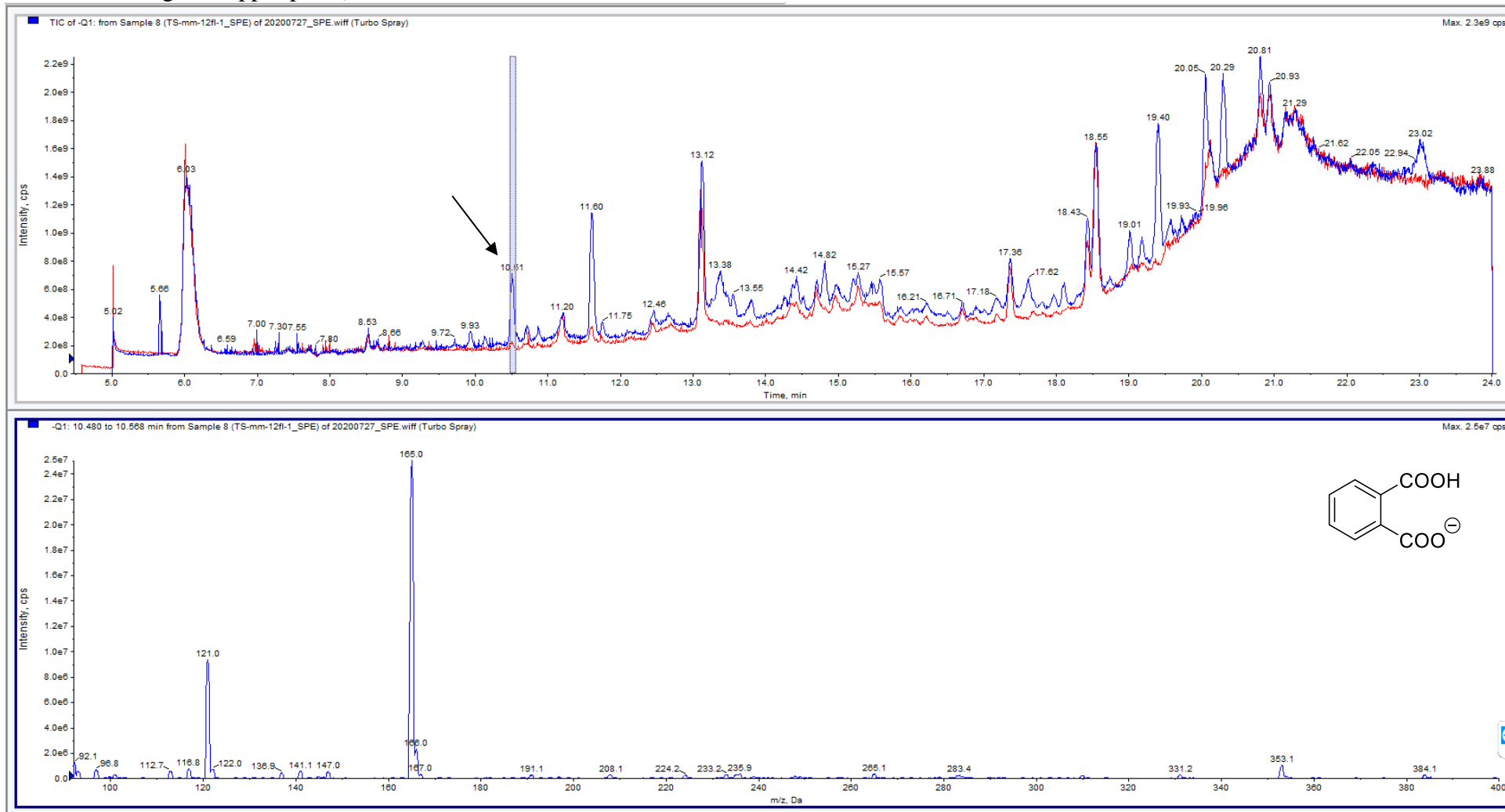


**Figure S76.** ESI mass spectrum (negative mode; bottom panel) of an aerated PBS solution of photoproduct mixture obtained upon irradiation of **1** with white-light LED reflectors and processed using method A processing. The mass spectrum shown is calculated for the grey area (highlighted in the chromatogram; upper panel) with a maximum in  $t = 11.60$  min.

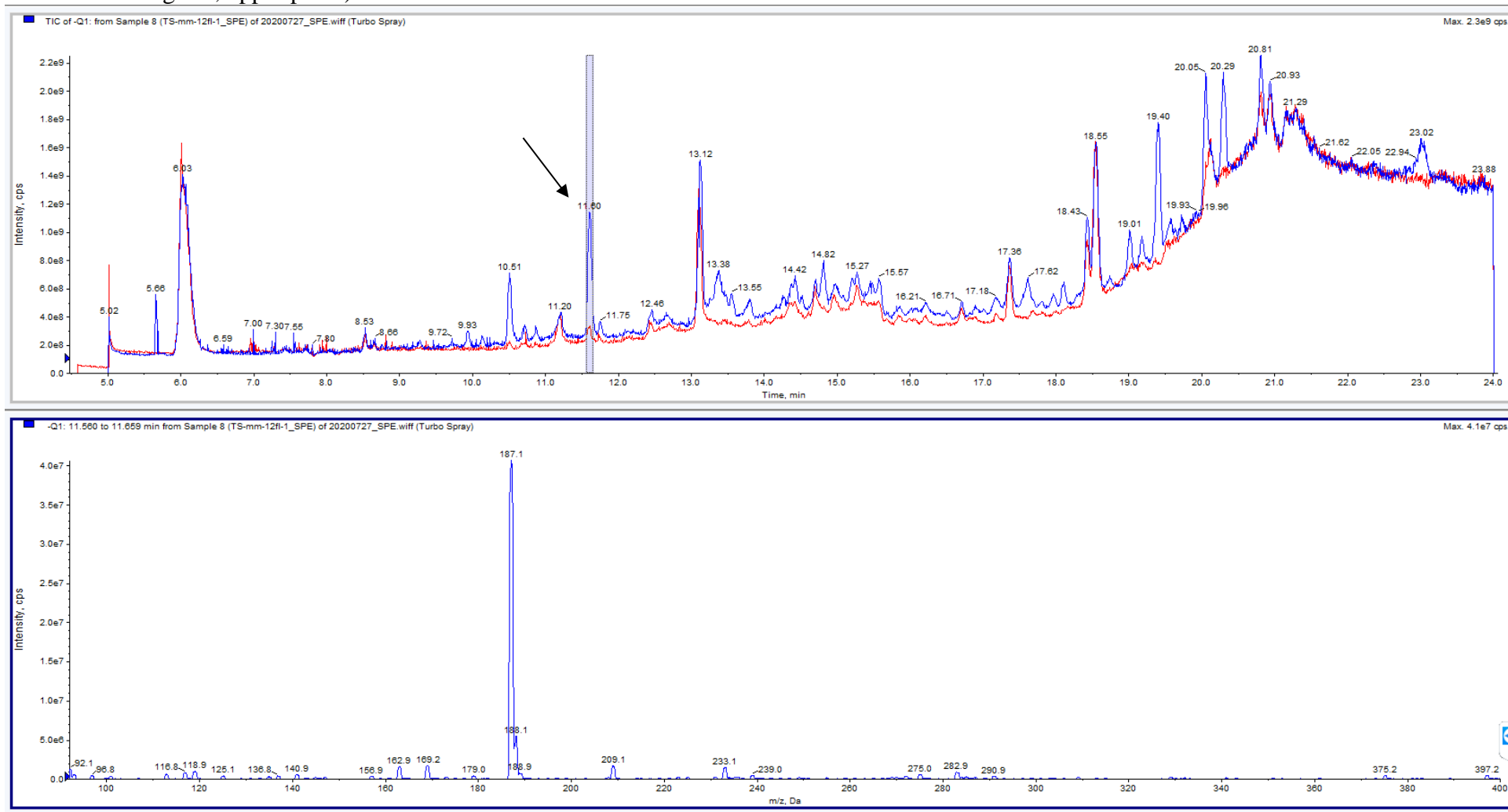


**Figure S77.** ESI mass spectrum (negative mode; bottom panel) of an aerated PBS solution of photoproduct mixture obtained upon irradiation of **1** with white-light LED reflectors and processed using method A processing. The mass spectrum shown is calculated for the grey area (highlighted in the chromatogram; upper panel) with a maximum in  $t = 13.38$  min.

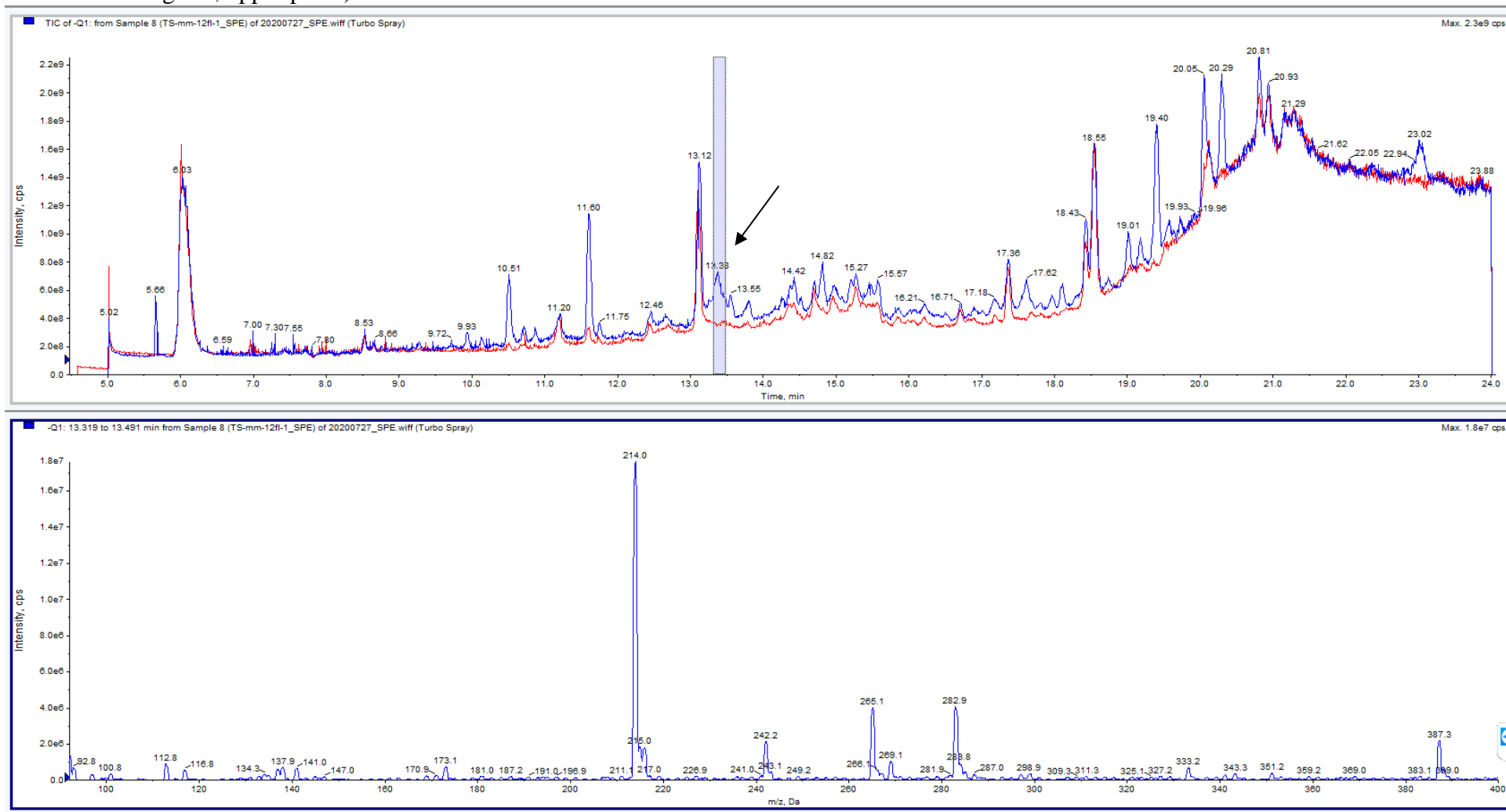


**Figure S78.** ESI mass spectrum (negative mode; bottom panel) of an aerated PBS solution of photoproduct mixture obtained upon irradiation of **1** with white-light LED reflectors and processed using method A processing. The mass spectrum shown is calculated for the grey area (highlighted in the chromatogram; upper panel) with a maximum in  $t = 14.82$  min.

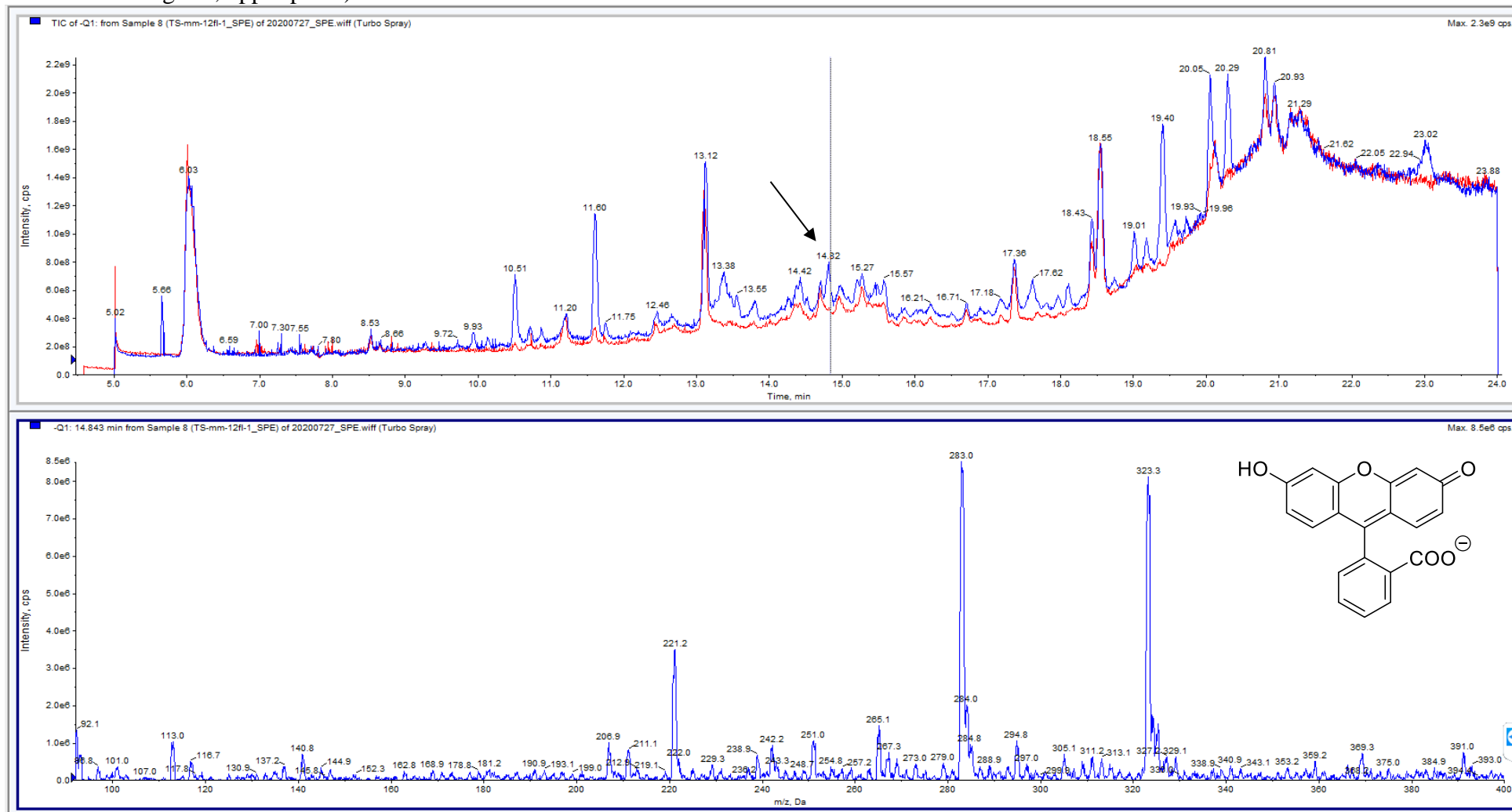


**Figure S79.** Chromatograms of a) sample of [ $^{13}\text{C}_2$ ]-**1** ( $c(\text{dye}) = 3 \times 10^{-5} \text{ mol dm}^{-3}$ ) in an aerated aqueous PBS buffer ( $\text{pH} = 7.4$ ,  $I = 0.1 \text{ mol dm}^{-3}$ ) irradiated with white-light LED reflectors for 4 days and then processed using method B (blue solid line); and b) samples of water (blank) (red solid line).

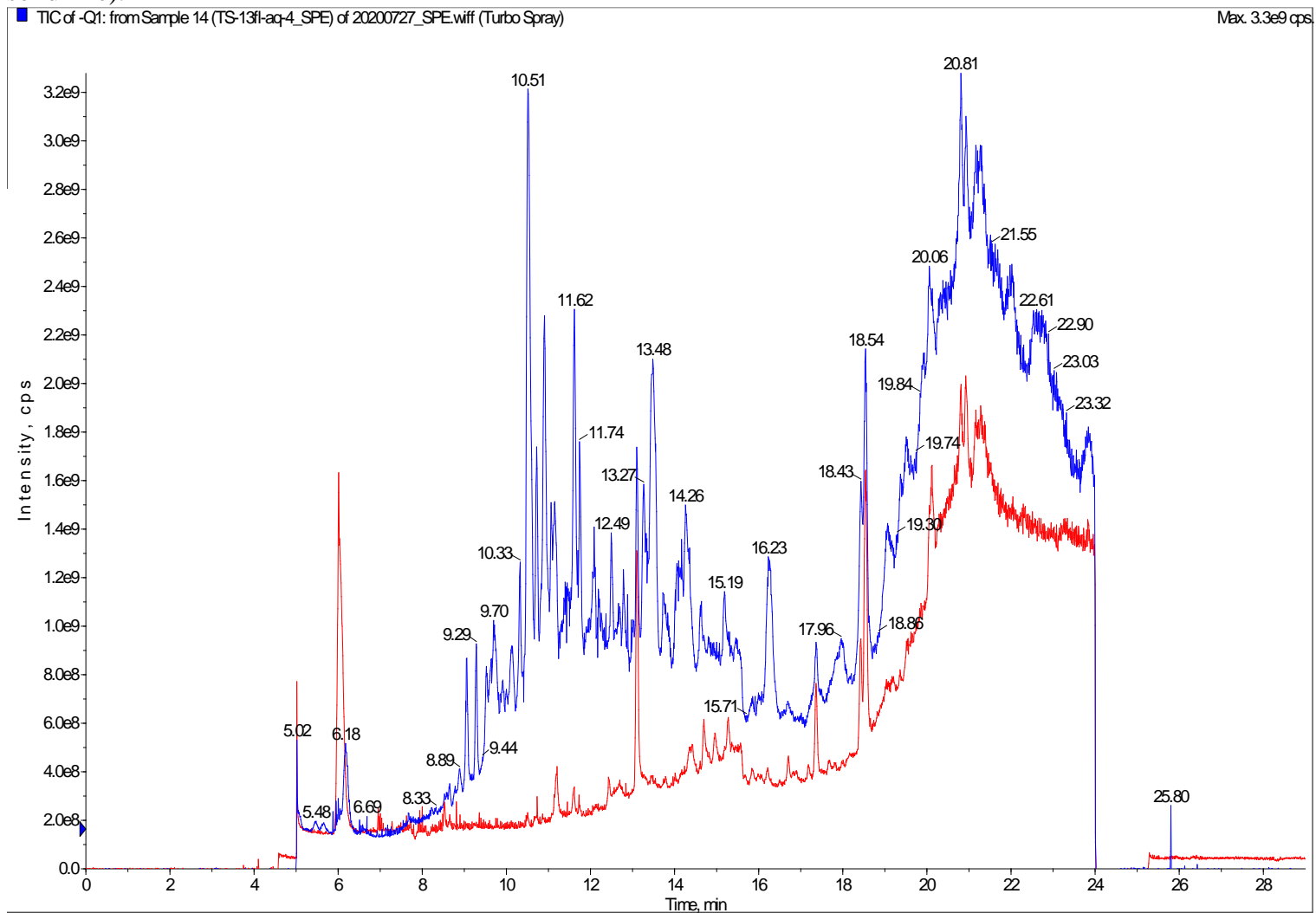


**Figure S80.** Chromatograms of a) sample of **1** ( $c(\text{dye}) = 3 \times 10^{-5} \text{ mol dm}^{-3}$ ) in a deoxygenated (argon bubbled for 15 min) aqueous PBS buffer (pH = 7.4,  $I = 0.1 \text{ mol dm}^{-3}$ ) and irradiated with white-light LED reflectors for 4 days and then processed using method B (solid blue line); and b) samples of water (blank) (solid red line).

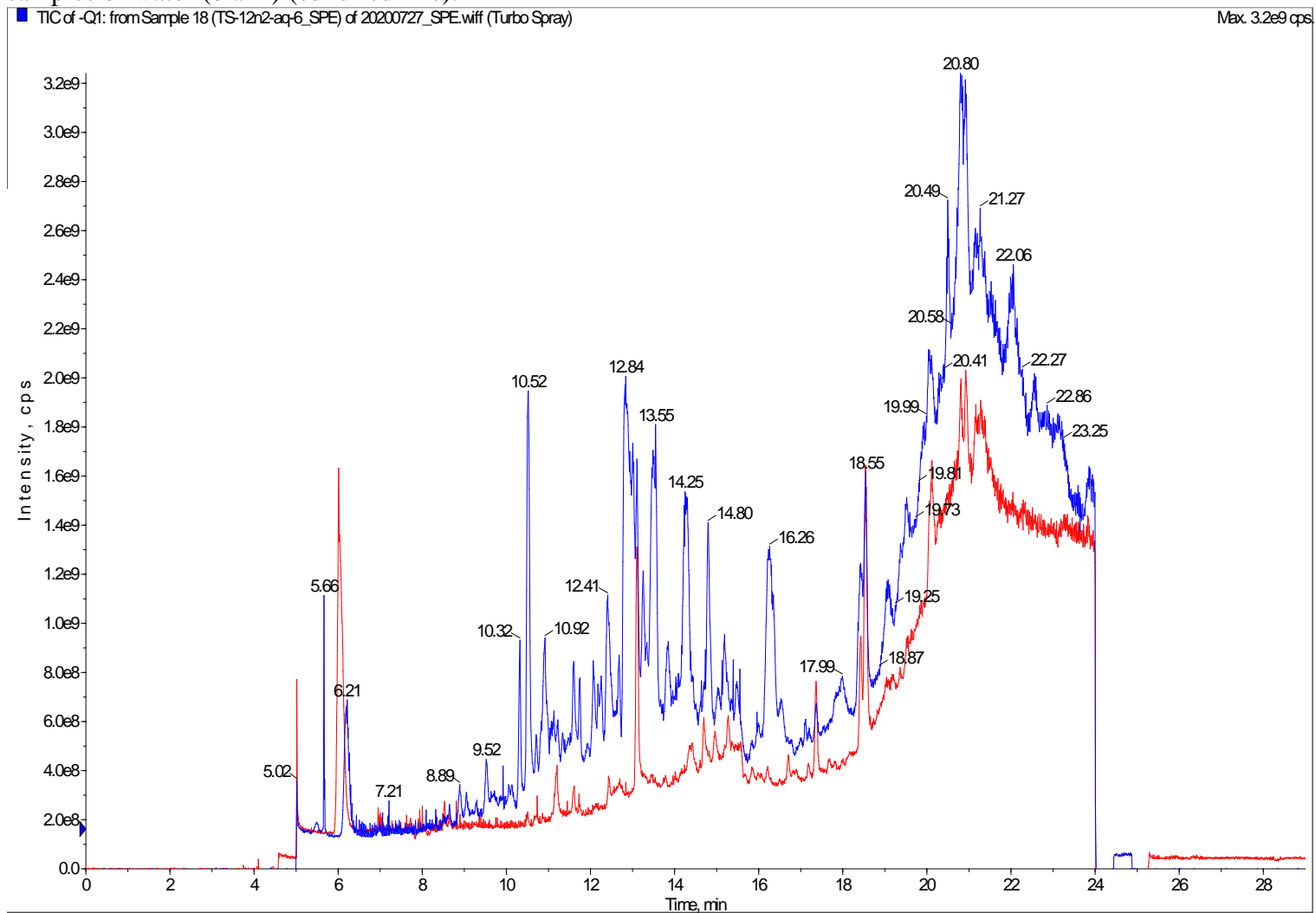


**Figure S81.** Image of a custom-made glass reactor with an attached spectrophotometric cuvette to measure optical properties of the solution. The total internal volume of the setup was determined to be  $V_{\text{tot}} = 1.05 \text{ L}$ .



**LED Sources.** The photochemical stability of compounds was tested using a homemade device allowing continuous irradiation of liquid samples and measurement of UV-vis absorption spectra to monitor the changes in the solution. The detailed scheme of this device was published previously by some of us.<sup>40</sup> For irradiation, arrays composed of 28 LEDs cooled with a built-in fan were used. The emission spectra of commercially available LEDs were determined (Table S7; emission spectra are shown in Figure S82).

**Table S7.** Selected Properties of 494 nm, 509 nm and 532 nm LEDs.

Manufacturer's label	Power dissipation <sup>b</sup>	Peak wavelength <sup>b</sup>	Measured wavelength <sup>c</sup>	Spectral half-width <sup>b,d</sup>	Measured half-width <sup>c,d</sup>
LED490-06 <sup>e</sup>	200 mW	480–500 nm	493.99 nm	30 nm	29 nm
B5-433-B505 <sup>e</sup>	120 mW	507 nm	508.85 nm	30 nm	32 nm
LED535-01 <sup>e</sup>	200 mW	525–545 nm	531.85 nm	35 nm	32 nm

<sup>a</sup> All LEDs were purchased from Roithner LaserTechnik GmbH. <sup>b</sup> Data from the datasheet. <sup>c</sup> Measured with a UV/vis spectrometer. <sup>d</sup> Bandwidth at half-height <sup>e</sup> Spectrum in Fig. S82.

**Figure S82.** The normalized emission spectra of LEDs used in the home-made 28-LED devices: a)  $\lambda_{em} = 494 \pm 14$  nm; b)  $\lambda_{em} = 509 \pm 17$  nm and c)  $\lambda_{em} = 532 \pm 16$  nm (bandwidth at a half-height).

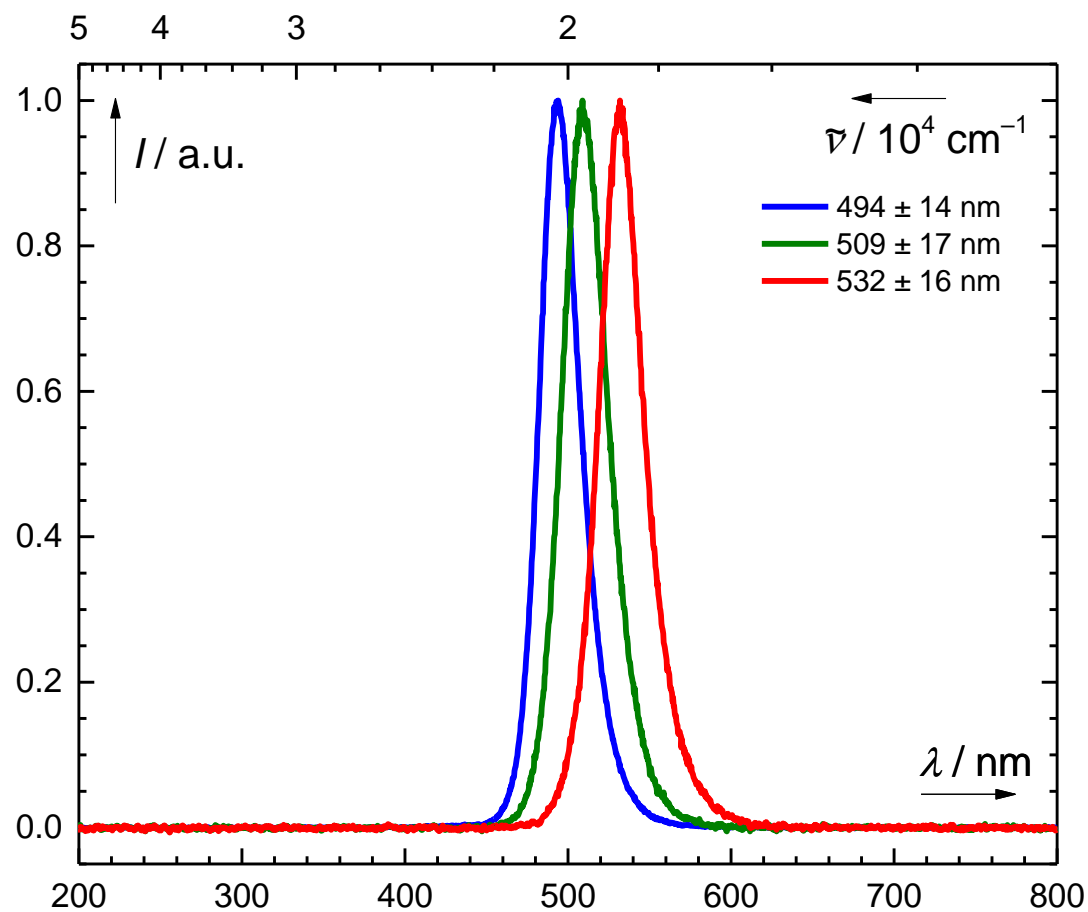


**Figure S83.** The normalized output spectra of LEDs used in 100 W LED irradiation panels (luminous flux 9 000 lm; color temperature 5 000 K):  $\lambda_{em} = 443\text{--}609$  nm (bandwidth at a half-height).

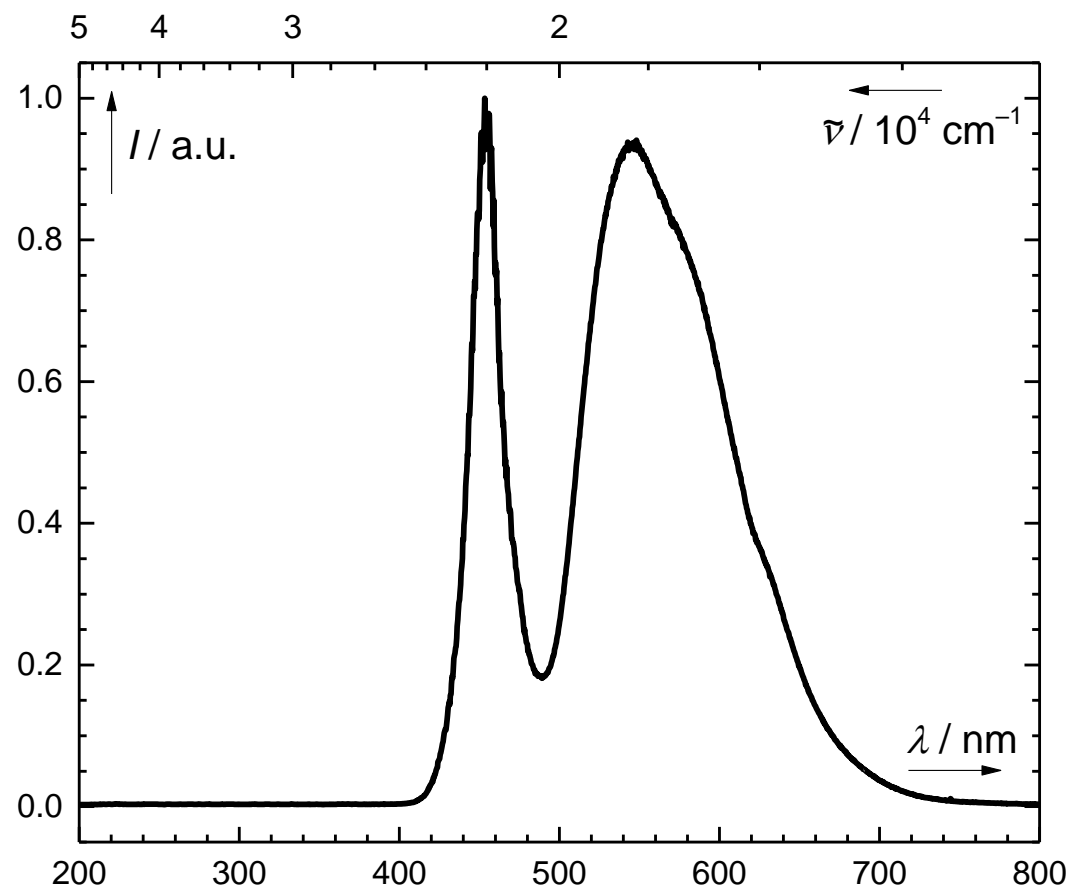


**Figure S84.** The normalized output spectra of LED (3 W):  $\lambda_{em} = 430\text{--}650\text{ nm}$  (bandwidth at a half-height).

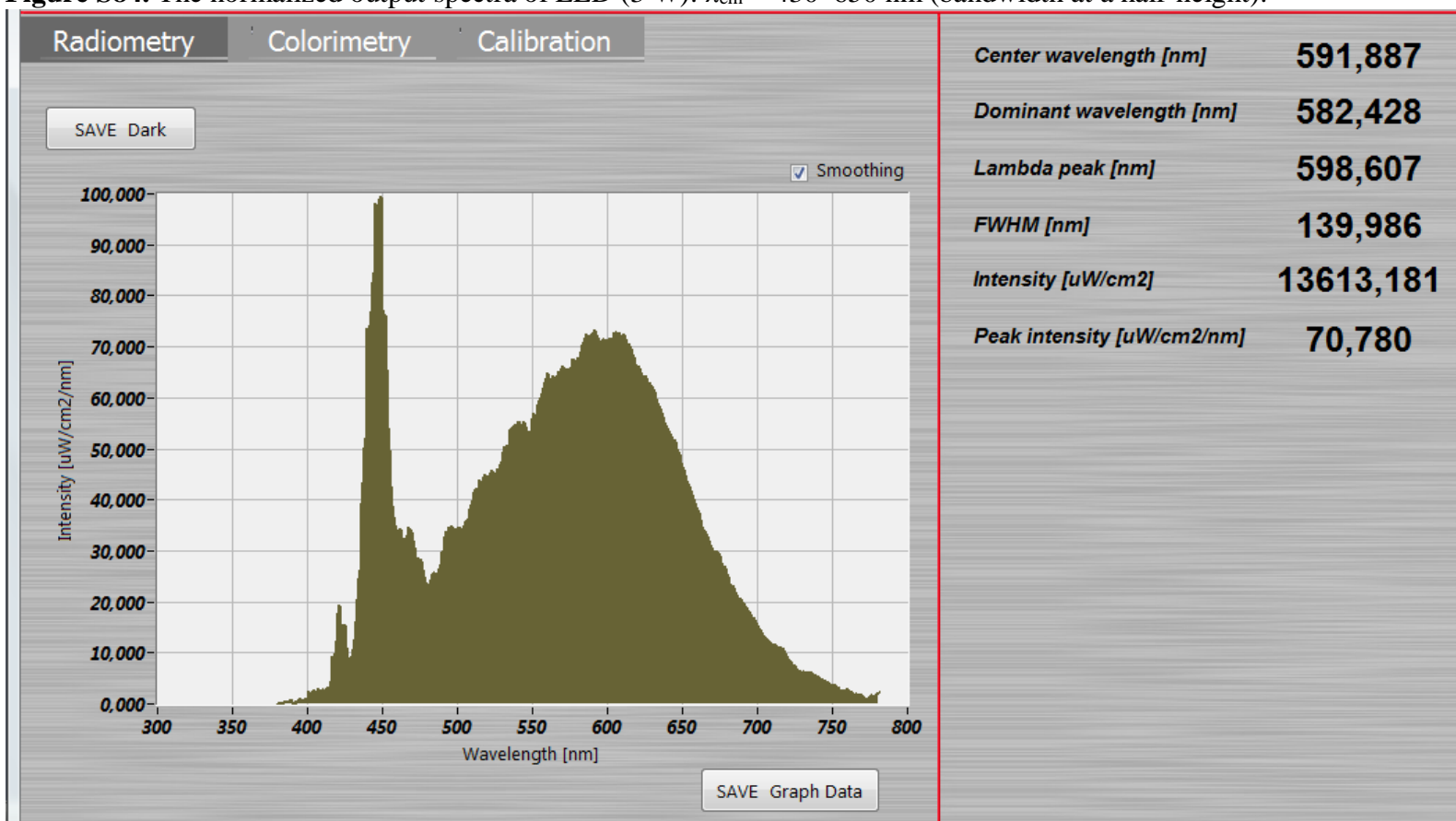
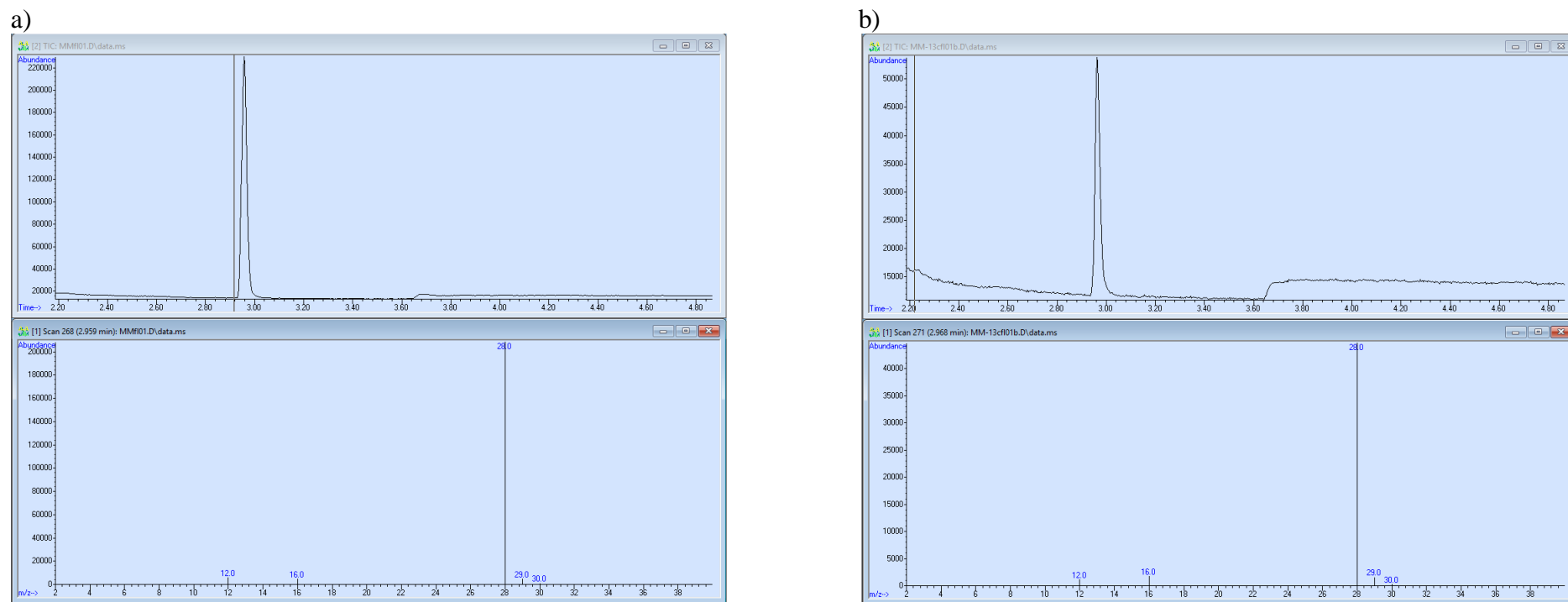


**Figure S85.** ESI mass spectrum (positive mode) of CO (determined by GC-MS) from the headspace above the reaction mixture of exhaustively irradiated a) **1** (left panel), and b)  $^{13}\text{C}_2\text{-1}$  (right panel). The peak corresponding to  $^{13}\text{CO}$  is visible at  $m/z = 29$ .



## Acknowledgement

The authors also express their thanks to Lukáš Maier and Miroslava Bittová for their help with the NMR and mass spectrometry measurements, Dominik Madea (all from Masaryk University, Brno) for the synthesis of 1,4-dimethyl-1,4-dihydro-1,4-epidioxynaphthalene (**4**), Tomáš Slanina (IOCB, Prague) for an MS analysis of the product mixtures and fruitful discussions. We thank Jana Roithová (Radboud University, Nijmegen) for an access to equipment for measurement of photodissociation and helium-tagging spectroscopy and Jan Zelenka (Charles University, Prague and Radboud University, Nijmegen) for assistance with measurements. Robert Vícha (T. Baťa University, Zlín) is acknowledged for elemental analyses, Zdeněk Moravec for thermogravimetric analyses, Luboš Jílek for his assistance with light sources, Jiří Nečas for manufacturing custom glass reactors, and Jiří Kalina (all from Masaryk University, Brno) for statistical analysis of the data.

## References

- (1) Martínek, M.; Filipová, L.; Galeta, J.; Ludvíková, L.; Klán, P. Photochemical Formation of Dibenzosilacyclohept-4-Yne for Cu-Free Click Chemistry with Azides and 1,2,4,5-Tetrazines. *Org. Lett.* **2016**, *18* (19), 4892–4895. <https://doi.org/10.1021/acs.orglett.6b02367>.
- (2) Slanina, T.; Shrestha, P.; Palao, E.; Kand, D.; Peterson, J. A.; Dutton, A. S.; Rubinstein, N.; Weinstain, R.; Winter, A. H.; Klán, P. In Search of the Perfect Photocage: Structure–Reactivity Relationships in Meso-Methyl BODIPY Photoremovable Protecting Groups. *J. Am. Chem. Soc.* **2017**, *139* (42), 15168–15175. <https://doi.org/10.1021/jacs.7b08532>.
- (3) Navrátil, R.; Wiedbrauk, S.; Jašík, J.; Dube, H.; Roithová, J. Transforming Hemithioindigo from a Two-Way to a One-Way Molecular Photoswitch by Isolation in the Gas Phase. *Phys. Chem. Chem. Phys.* **2018**, *20* (10), 6868–6876. <https://doi.org/10.1039/C8CP00096D>.
- (4) Jašík, J.; Gerlich, D.; Roithová, J. Probing Isomers of the Benzene Dication in a Low-Temperature Trap. *J. Am. Chem. Soc.* **2014**, *136* (8), 2960–2962. <https://doi.org/10.1021/ja412109h>.
- (5) Jašík, J.; Žabka, J.; Roithová, J.; Gerlich, D. Infrared Spectroscopy of Trapped Molecular Dications below 4K. *International Journal of Mass Spectrometry* **2013**, *354–355*, 204–210. <https://doi.org/10.1016/j.ijms.2013.06.007>.
- (6) Gerlich, D.; Jašík, J.; Andris, E.; Navrátil, R.; Roithová, J. Collisions of FeO<sup>+</sup> with H<sub>2</sub> and He in a Cryogenic Ion Trap. *ChemPhysChem* **2016**, *17* (22), 3723–3739. <https://doi.org/10.1002/cphc.201600753>.
- (7) Nencki, M.; Sieber, N. Ueber Die Verbindungen Der Ein- Und Zweibasischen Fettsäuren Mit Phenolen. *Journal für Praktische Chemie* **1881**, *23* (1), 147–156. <https://doi.org/10.1002/prac.18810230111>.
- (8) Stephenson, C. J.; Shimizu, K. D. A Fluorescent Diastereoselective Molecular Sensor for 1,2-Aminoalcohols Based on the Rhodamine B Lactone–Zwitterion Equilibrium. *Org. Biomol. Chem.* **2010**, *8* (5), 1027–1032. <https://doi.org/10.1039/B918823A>.
- (9) Furniss, B. S.; Vogel, A. I. *Vogel's Textbook of Practical Organic Chemistry Including Qualitative Organic Analysis. 4.Ed. Revised by B.S.Furniss A.o: Textbook of Practical Organic Chemistry. 4.Ed*; Longman XXXV, 1978.
- (10) Sujeeth, P. K. Syntheses of Fluorescein Compounds with Excess Resorcinol as a Solvent. US5637733A, June 10, 1997.
- (11) Melhado, L. L.; Peltz, S. W.; Leytus, S. P.; Mangel, W. F. P-Guanidinobenzoic Acid Esters of Fluorescein as Active-Site Titrants of Serine Proteases. *J. Am. Chem. Soc.* **1982**, *104* (25), 7299–7306. <https://doi.org/10.1021/ja00389a065>.
- (12) da Silva, B. H. S. T.; Bregadiolli, B. A.; Graeff, C. F. de O.; da Silva-Filho, L. C. NbCl<sub>5</sub>-Promoted Synthesis of Fluorescein Dye Derivatives: Spectroscopic and Spectrometric Characterization and Their Application in Dye-Sensitized Solar Cells. *ChemPlusChem* **2017**, *82* (2), 261–269. <https://doi.org/10.1002/cplu.201600530>.
- (13) Sjöback, R.; Nygren, J.; Kubista, M. Absorption and Fluorescence Properties of Fluorescein. *Spectrochimica Acta Part A: Molecular and Biomolecular Spectroscopy* **1995**, *51* (6), L7–L21. [https://doi.org/10.1016/0584-8539\(95\)01421-P](https://doi.org/10.1016/0584-8539(95)01421-P).
- (14) Ludvíková, L.; Friš, P.; Heger, D.; Šebej, P.; Wirz, J.; Klán, P. Photochemistry of Rose Bengal in Water and Acetonitrile: A Comprehensive Kinetic Analysis. *Phys. Chem. Chem. Phys.* **2016**, *18* (24), 16266–16273. <https://doi.org/10.1039/C6CP01710J>.
- (15) Cramer, L. E.; Spears, K. G. Hydrogen Bond Strengths from Solvent-Dependent Lifetimes of Rose Bengal Dye. *J. Am. Chem. Soc.* **1978**, *100* (1), 221–227. <https://doi.org/10.1021/ja00469a039>.

- (16) Fleming, G. R.; Knight, A. W. E.; Morris, J. M.; Morrison, R. J. S.; Robinson, G. W. Picosecond Fluorescence Studies of Xanthene Dyes. *J. Am. Chem. Soc.* **1977**, *99* (13), 4306–4311. <https://doi.org/10.1021/ja00455a017>.
- (17) Rauf, M. A.; Graham, J. P.; Bukallah, S. B.; Al-Saedi, M. A. S. Solvatochromic Behavior on the Absorption and Fluorescence Spectra of Rose Bengal Dye in Various Solvents. *Spectrochimica Acta Part A: Molecular and Biomolecular Spectroscopy* **2009**, *72* (1), 133–137. <https://doi.org/10.1016/j.saa.2008.08.018>.
- (18) Lakowicz, J. R. *Principles of Fluorescence Spectroscopy*, 3rd ed.; Springer US, 2006.
- (19) *Molecular Probes Handbook, A Guide to Fluorescent Probes and Labeling Technologies, 11th Edition*, 11th edition.; Johnson, I., Spence, M. T. Z., Eds.; Life Technologies: Carlsbad, Calif., 2010.
- (20) Gollnick, K.; Schenck, G. O. Mechanism and stereoselectivity of photosensitized oxygen transfer reactions. *Pure and Applied Chemistry* **1964**, *9* (4), 507–526. <https://doi.org/10.1351/pac196409040507>.
- (21) Usui, Y. Determination of Quantum Yield of Singlet Oxygen Formation by Photosensitization. *Chem. Lett.* **1973**, *2* (7), 743–744. <https://doi.org/10.1246/cl.1973.743>.
- (22) Chakraborty, M.; Panda, A. K. Spectral Behaviour of Eosin Y in Different Solvents and Aqueous Surfactant Media. *Spectrochimica Acta Part A: Molecular and Biomolecular Spectroscopy* **2011**, *81* (1), 458–465. <https://doi.org/10.1016/j.saa.2011.06.038>.
- (23) Kasche, V.; Lindqvist, L. Transient Species in the Photochemistry of Eosin\*. *Photochemistry and Photobiology* **1965**, *4* (5), 923–933. <https://doi.org/10.1111/j.1751-1097.1965.tb07941.x>.
- (24) Acharya, S.; Rebery, B. Fluorescence Spectrometric Study of Eosin Yellow Dye–Surfactant Interactions. *Arabian Journal of Chemistry* **2009**, *2* (1), 7–12. <https://doi.org/10.1016/j.arabjc.2009.07.010>.
- (25) Bowers, P. G.; Porter, G. Triplet State Quantum Yields for Some Aromatic Hydrocarbons and Xanthene Dyes in Dilute Solution. *Proc. R. Soc. Lond. A* **1967**, *299* (1458), 348–353. <https://doi.org/10.1098/rspa.1967.0141>.
- (26) Reindl, S.; Penzkofer, A. Triplet Quantum Yield Determination by Picosecond Laser Double-Pulse Fluorescence Excitation. *Chemical Physics* **1996**, *213* (1), 429–438. [https://doi.org/10.1016/S0301-0104\(96\)00289-3](https://doi.org/10.1016/S0301-0104(96)00289-3).
- (27) Berndt, O.; Bandt, F.; Eichwurz, I.; Stiel, H. Picosecond Transient Absorption of Xanthene Dyes. *Acta Physica Polonica A* **1999**, *95* (2), 207–220. <https://doi.org/10.12693/APhysPolA.95.207>.
- (28) Bernstein, R.; Foote, C. S. Singlet Oxygen Involvement in the Photochemical Reaction of C60 and Amines. Synthesis of an Alkyne-Containing Fullerene. *J. Phys. Chem. A* **1999**, *103* (36), 7244–7247. <https://doi.org/10.1021/jp991534t>.
- (29) Turro, N. J.; Chow, M. F. Mechanism of Thermolysis of Endoperoxides of Aromatic Compounds. Activation Parameters, Magnetic Field, and Magnetic Isotope Effects. *J. Am. Chem. Soc.* **1981**, *103* (24), 7218–7224. <https://doi.org/10.1021/ja00414a029>.
- (30) Cargill, R. W. (ed). *Solubility Data Series, Volume 43, Carbon Monoxide*; Pergamon Press, 1990. <https://doi.org/10.1016/C2009-0-01228-8>.
- (31) Power, G. G.; Stegall, H. Solubility of Gases in Human Red Blood Cell Ghosts. *Journal of Applied Physiology* **1970**, *29* (2), 145–149. <https://doi.org/10.1152/jappl.1970.29.2.145>.
- (32) Schmidt, U. The Solubility of Carbon Monoxide and Hydrogen in Water and Sea-Water at Partial Pressures of about 10<sup>-5</sup> Atmospheres. *Tellus* **1979**, *31* (1), 68–74. <https://doi.org/10.3402/tellusa.v31i1.10411>.
- (33) O'Brien, H. R.; Parker, W. L. Solubility of Carbon Monoxide in Serum and Plasma. *J. Biol. Chem.* **1922**, *50* (1), 289–300.

- (34) Dake, S. B.; Chaudhari, R. V. Solubility of Carbon Monoxide in Aqueous Mixtures of Methanol, Acetic Acid, Ethanol and Propionic Acid. *J. Chem. Eng. Data* **1985**, *30* (4), 400–403. <https://doi.org/10.1021/je00042a010>.
- (35) McQueen, P. D.; Sagoo, S.; Yao, H.; Jockusch, R. A. On the Intrinsic Photophysics of Fluorescein. *Angewandte Chemie International Edition* **2010**, *49* (48), 9193–9196. <https://doi.org/10.1002/anie.201004366>.
- (36) Yao, H.; Jockusch, R. A. Fluorescence and Electronic Action Spectroscopy of Mass-Selected Gas-Phase Fluorescein, 2',7'-Dichlorofluorescein, and 2',7'-Difluorofluorescein Ions. *J. Phys. Chem. A* **2013**, *117* (6), 1351–1359. <https://doi.org/10.1021/jp309767f>.
- (37) Navrátil, R.; Jašík, J.; Roithová, J. Visible Photodissociation Spectra of Gaseous Rhodamine Ions: Effects of Temperature and Tagging. *Journal of Molecular Spectroscopy* **2017**, *332*, 52–58. <https://doi.org/10.1016/j.jms.2016.10.016>.
- (38) Antony, L. A. P.; Slanina, T.; Šebelj, P.; Šolomek, T.; Klán, P. Fluorescein Analogue Xanthene-9-Carboxylic Acid: A Transition-Metal-Free CO Releasing Molecule Activated by Green Light. *Org. Lett.* **2013**, *15* (17), 4552–4555. <https://doi.org/10.1021/ol4021089>.
- (39) Madea, D.; Slanina, T.; Klán, P. A 'Photorelease, Catch and Photorelease' Strategy for Bioconjugation Utilizing a p-Hydroxyphenacyl Group. *Chem. Commun.* **2016**, *52* (87), 12901–12904. <https://doi.org/10.1039/C6CC07496K>.
- (40) Štacková, L.; Muchová, E.; Russo, M.; Slavíček, P.; Štacko, P.; Klán, P. Deciphering the Structure–Property Relations in Substituted Heptamethine Cyanines. *J. Org. Chem.* **2020**, *85* (15), 9776–9790. <https://doi.org/10.1021/acs.joc.0c01104>.